Fabrication of Capacitive Micromachined Ultrasonic Transducers based on Adhesive Wafer Bonding

by

Zhenhao Li

A thesis

presented to the University of Waterloo

in fulfillment of the

thesis requirement for the degree of

Doctor of Philosophy

in

Systems Design Engineering (Nanotechnology)

Waterloo, Ontario, Canada, 2017

© Zhenhao Li 2017

AUTHOR'S DECLARATION

I hereby declare that I am the sole author of this thesis. This is a true copy of the thesis, including any required final revisions, as accepted by my examiners.

I understand that my thesis may be made electronically available to the public.

Abstract

Capacitive micromachined ultrasonic transducers (CMUTs) can be used for medical imaging, non-destructive testing or medical treatment applications. It can also be used as gravimetric sensors for gas sensing or immersion bio-sensing. Although various CMUT fabrication methods have been reported, there are still many challenges to address.

Conventional fabrication methods can be categorized as either surface micromachining or the wafer bonding method. These methods have design trade-offs and limitations associated with process complexity, structural parameter optimization and wafer materials selection. For example, surface micromachining approaches can suffer from complicated fabrication processes. In addition, structural parameters cannot be fully optimized due to feasibility concerns during fabrication. In contrast, the development of wafer bonding techniques enabled CMUTs to be fabricated in a straightforward way and structural parameters can be easily optimized when compared with a surface micromachining approach. However, the yield of the traditional wafer bonded CMUTs is very sensitive to contaminations and the surface quality at the bonding interface. Although the difficulties of the wafer bonding process are not always reported, they definitely exist for every researcher who wants to fabricate their own CMUTs. As a result, this dissertation work aims to develop a CMUT fabrication process with fewer fabrication constraints, low-cost and low process temperature for CMOS integration.

The developed CMUT fabrication processes reported in the thesis applied photosensitive polymer adhesive for wafer bonding in order to make a process with good tolerance to contaminations and defects on the wafer surface, present a wide range of material selection at the bonding interface and require low process temperature (less than 250°C). These features can benefit CMUT fabrication with increased yield better design flexibility and lower cost. Having maximum process temperature of 250°C, the developed processes can also be CMOS compatible. Furthermore, a novel CMUT structure, which can only be achieved by the reported technique, was developed showing more than doubled ultrasound receive sensitivity when compared with conventional CMUT structures. The fabrication processes were developed systematically and the details of process development will be presented in this thesis.

Acknowledgements

To my supervisor, Prof. Yeow. Thank you for giving me the opportunity to work in AMNDL. Thank you for supporting all the equipment/materials, and facility accesses. I know how expensive they are and without you, I would not have been able to execute my ideas and finish the projects.

To my committees, Prof. Huissoon, Prof. Nieva and Prof. Stashuk, Thank you for all the comments and suggestions on my project. Additionally, I would say thank you to Prof. Huissoon. You gave me the to come to study in Waterloo and I will never forget the time I received your email where you asked me to come to Canada. To Prof. Cretu, thank you for agreeing to be the external committee and travelling to Waterloo for my defence.

The CMUTs in this thesis were fabricated in G2N and TNFC. I would say thank Richard, Czang-Ho, Edward, Harlan, Minoli, Mark, Mike, Peng, Jian, Sina and Celal who trained me and helped me in the cleanroom. I especially want to say thank you to Prof. Karim and Sina who shared the BCB with me and helped me on processing the material for it has a dramatic impact on my thesis.

Lawrence, you are the first person who helped me get settled in the lab on the first day. Albert, you are the one who introduced me to the lab. Shruti, I will never forget the time working with you. You taught me how to read and write papers, reply emails, work with polymers and nanotubes and plan the experiments. Manu, the two silicon wafers from you helped me start the fabrication in the cleanroom. Nash and Albert, I will not forget the countless of hours we spent together in the cleanroom. Sangtak, thank you for helping me with vibrometer, signal generator and bias-T. All other lab mates: Sora, Rabindra, 'Big' Mohammod, 'Small' Mohammod, Mehdi, Yun, Weijie, Yibei, Limin, Siyuan, Champika, Wenzhu, Leon, Hui, Fangjun, Yunhan, Chen, Joe, Yaning, Mingyu, Jame, Jesse, Adam. Thank you all for the helps in the past five years and nice meeting you.

Lastly but foremost, thank you to my dear parents and my beloved, Yao. Thank you for the company and support for they are vital to me finishing the PhD.

Table of Contents

AUTHOR'S DECLARATION ii

Abstract iii

Acknowledgements iv

Table of Contents v

List of Figures viii

List of Tables xii

Chapter 1 Introduction 1

1.1 Motivation 1

1.2 Contribution and Thesis Organization 3

Chapter 2 Literature Review and Methodology 5

2.1 A Review of CMUT Fabrication Techniques 5

2.2 Comparison and Selection of Adhesives 17

2.3 Wafers for Bonding 19

2.4 Objectives 20

Chapter 3 Process Study 21

3.1 Chemistry in BCB Coating and Wafer Bonding Process 21

3.2 Experimental Study: Chemical Group Characterization 25

3.3 Photo BCB Coating 28

3.3.1 Non-patterned Photo BCB Film 28

3.3.2 Patterned Photo BCB Film 32
3.4 Summary of Process Study 34
Chapter 4 First-Generation Adhesive Wafer Bonded CMUT 35
4.1 Fabrication Process 35
4.2 Fabrication Issues 38
4.2.1 Bonding Strength and Structural Dimensions 38
4.2.2 Photo BCB and Dry-Etch BCB for Wafer Bonding 41
4.3 Characterization 43
4.3.1 Pull-in Voltage and In-air Resonance Frequency 43
4.3.2 Acoustic Characterization 45
4.4 Summary 48
Chapter 5 Fabrication Process Optimization 50
5.1 Problem Analysis and Process Modification 50
5.2 Device Characterization 53
5.2.1 Structure Dimensions 53
5.2.2 In-air Characterization 56
5.2.3 Immersion Characterization 59
5.2.4 Discussion in Collapse Voltage 61
5.3 Summary 62
Chapter 6 Second-Generation Adhesive Wafer Bonded CMUT 64
6.1 Fabrication Process 64
6.2 Two-layer Membrane Modelling 66
6.3 Device Characterization 67
6.3.1 Structure Dimensions 67

6.3.2 In-air Characterization ... 71
6.3.3 Immersion Characterization ... 73
6.3.4 Discussion in Collapse Voltage ... 74
6.4 Summary ... 76
Chapter 7 Conclusion and Future Works ... 77
7.1 Summary of Works ... 77
7.2 Future Works ... 79
7.3 Concluding Remarks ... 83
Letter of Copyright Permission ... 85
Bibliography ... 90
Appendix A CMUT Modelling ... 98
A.1 Lumped Model ... 98
A.1.1 Loading Force ... 99
A.1.2 Mechanical Force ... 100
A.1.3 Electrostatic Force ... 104
A.1.4 Force of Inertia ... 106
A.2 Pull-in Effect ... 106

List of Figures

Figure 1: Illustration of basic CMUT structure 1

Figure 2: General surface micromachining process for CMUT fabrication [6]. 7

Figure 3: SOI-oxide wafer bonding process for CMUT fabrication [56]. 8

Figure 4: CMUT fabrication based on LPCVD SiN-SiN wafer bonding [58]. 9

Figure 5: CMUT fabrication based on anodic wafer bonding [59]. 11

Figure 6: Vacuum sealed cavities fabrication process [62]. 12

Figure 7: Coating-patterning-bonding process comparison between dry-etch BCB and photo BCB 22

Figure 8: Monomers of BCB and DVS-bis-BCB [77, 78] 23

Figure 9: Reactions during BCB curing process [78] 24

Figure 10: bis-aryl azide and its reaction under UV exposure [77, 79] 24

Figure 11: IR Absorbance spectrum of the BCB film after coating, annealing and curing processes. 27

Figure 12: Photo of BCB coated silicon wafer with spin rate of 3000 RPM. Contaminations caused thickness variations. 30

Figure 13: Thickness distribution before and after soft cure with different spin rate. 31

Figure 14: Stress map of wafers with different BCB thicknesses before and after soft curing process. 32

Figure 15: Cavity depths on difference location of the wafer before and after soft cure were measured with profilometer. The measurement results are marked at the corresponding measurement location that are illustrated in this figure. 33

Figure 16: Fabrication process of the first-generation photo BCB CMUTs 38

Figure 17: Cross sectional view of a CMUT cell through a window opened by FIB. The image was taken from slanting angle of 54°. The smaller image on the top left corner is taken by microscope, indicating the position of the opened window relative to the CMUT cell. 39

Figure 18: Deformation process of the BCB layers under compressive bonding force during wafer bonding step. 40

Figure 19: Temperature profiles of photo BCB and dry-etch BCB for wafer bonding. The profile of photo BCB showed better time efficiency than dry-etch BCB. 41

Figure 20: Microscopy images of the fabricated CMUT with no soft cure 42

Figure 21: Resonance frequency measurement under bias voltages of 50 to 300 V by sweeping frequencies of AC signal with amplitude of 7.5 V 44

Figure 22: VNA measurement result under bias voltage of 125 V, 150 V, 175 V and 200 V. The impedance magnitude is plotted in logarithmic scale. 45

Figure 23: The setup of T-CMUT and R-CMUT 46

Figure 24: The signal that inputs into T-CMUT for ultrasound generation. The signal was presented in both time domain (left) and in frequency domain (right). The signal presents a relatively flat frequency band between 0 and 20 MHz, but a peak in amplitude appeared around 31 MHz. 46
Figure 25: Output of the hydrophone in both time domain (left) and frequency domain (right). The center frequency is 3.1 MHz and the -3dB fractional bandwidth is 106.3%. The signal indicates an acoustic pressure of 79.28 kPa at the position of the hydrophone tip. 47
Figure 26: Receive test result showing output of the transimpedance amplifier in both time domain (left) and in frequency domain (right). The center frequency is 3.0MHz and the -6 dB fractional bandwidth is 137.7%. The signal indicates a receive sensitivity of 2.36 μV/Pa 48
Figure 27: illustration of the paths for applying DC bias. 51
Figure 28: Modified fabrication flow. The newly added annealing process and HF dip step are highlighted with color blue. 52
Figure 29: Thickness measurement of two of the purchased silicon nitride wafers. 53
Figure 30: Microscopy image of 16-element CMUT. Dimensions were calculated based on the cell to cell distance and the ratio of interested dimensions to the cell to cell distance. 54
Figure 31: Cross section view of CMUT cell through a window opened by FIB and the image was taken from slanting angle of 54°. The BCB deformation effect was not found through the images. The microscopy image on the top right corner of image b) shows the position of the cutting window. 55
Figure 32: Resonance frequency of one of the element in 1-D array under bias voltages of 25 to 100 V by sweeping frequencies of AC signal with amplitude of 2.5 V 56
Figure 33: Resonance frequencies of each element in 1-D array under bias voltages of 25 to 100 V with AC signal amplitude of 2.5 V 57
Figure 34: Resonance frequency of one of the one-element CMUT under bias voltages of 25 to 100 V by sweeping frequencies of AC signal with amplitude of 2.5 V 57
Figure 35: VNA measurement result under bias voltage of 25 V, 50 V, 75 V and 100 V. 58
Figure 36: Network analyzer measurement results at bias voltages of 145 V and 200 V, respectively. High frequency peaks appeared gradually starting from at 145 V bias and the peaks became more obvious with the increased bias voltage. 59
Figure 37: The ultrasound signal pulsed by PZT transducer for ultrasound generation. The signal was presented in both time domain (left) and in frequency domain (right). The signal presents a peak frequency at 2.05 MHz. The -3 dB band is from 1.19 to 3.42 MHz with center frequency of 2.31 MHz. The peak to peak voltage is 34.25 mV indicating a sound pressure of 639 kPa at the hydrophone tip. 60

Figure 38: Use CMUT in receive mode setup in transimpedance configuration with a 25kΩ-gain to receive the ultrasonic signal from the PZT transducer. The CMUT was biased at 100 V showing 0-dB-peaks in frequency domain at 1.27 MHz. 61
Figure 39: Pull-in voltage calculation based on structure dimensions. 62
Figure 40: Theoretical calculation results: Maximum plate deflection under bias voltage from 1 V to the calculated pull-in voltage. 62
Figure 41: Fabrication process of the second-generation photo BCB CMUTs 65
Figure 42: Cross section view of CMUT cell through a window opened by FIB and the image was taken from slanting angle of 54°. The microscopy image on the top left corner of image a) shows the position of the cutting window. 68
Figure 43: SEM images for cross-section inspection on mechanically broken CMUT at different slanted angle. The images showed that the membrane was not touching the bottom Cr electrodes. 69
Figure 44: Microscopy image of Generation 2 1D CMUT array. Dimensions were calculated based on the cell to cell distance and the ratio of interested dimensions to the cell to cell distance. 70
Figure 45: VNA measurement result of second generation CMUT under bias voltage of 20 V to 100 V. The measured element in 1-D CMUT array locates in the centre region of the wafer during fabrication. 71
Figure 46: VNA measurement result of second generation CMUT under bias voltage of 20 V to 100 V. The measured one-element CMUT locates at the edge of the wafer during fabrication. 72
Figure 47: Resonance frequencies of each element in second generation 1-D array CMUT under bias voltage of 100 V with AC signal amplitude of 2.5 V. The average resonance frequency over 16 elements is 6.4 MHz with standard deviation of 0.27MHz. 72
Figure 48: Immersion test result of the second generation CMUT. The immersion resonance 73
Figure 49: Received ultrasound signal of both the optimized first generation and the second generation CMUTs, which are both biased at 100 V under receive mode against ultrasound waves with same sound pressure. 74
Figure 50: Pull-in voltage calculation based on structure dimensions. 75
Figure 51: Theoretical calculation results: Maximum plate deflection under bias voltage from 1 V to the calculated pull-in voltage. 76
Figure 52: Illustration of 2D CMUT array fabrication process. 80
Figure 53: A process designed for integrating CMUT fabrication with a fabricated ASIC chip. 81
Figure 54: Microscopy image of the ASIC chip. The size of the chip is about 3.5 mm by 3.5 mm. Electrodes for amplifier setup are also illustrated. 82
Figure 55: Illustration of flexible CMUT fabrication process. 83
Figure 56: Spring-mass damping system 98

Figure 57: Both atmosphere pressure ($patm$) and electrostatic force ($p0$) will induce membrane deflection. 101

Figure 58: The intersection between the curve of electrostatic force and the spring force are the equilibrium states. The upper-left one is the non-stable one corresponding to higher energy and the lower-right one is the stable one corresponding to lower energy. When bias voltage is equal to the pull-in voltage, two equilibriums are merged. 107

List of Tables

Table 1: Comparison among fabrication techniques 13
Table 2: Process details of reviewed fabrication techniques 14
Table 3: Absorbance IR peaks summary and corresponding vibrations [81-84] 27
Table 4: Ellipsometer measurement results: average thickness and standard deviation. 31
Table 5: Summary of cavity depths and depth decrease percentage. 33
Table 6: Structural dimensions of the fabricated one-element CMUT 40
Table 7: Fabrication process comparison 49
Table 8: Photo mask design parameters 53
Table 9: Structural dimensions of the CMUT fabricated with improved process 56
Table 10: Statistical analysis of resonance frequency measurement results for 1-D array CMUT .. 57
Table 11: Structural dimensions of the second generation CMUT. 70

Chapter 1 Introduction

1.1 Motivation

Capacitive micromachined ultrasonic transducers (CMUTs) are capacitive parallel-plate transducers for ultrasonic applications. A typical CMUT structure is illustrated in Figure 1. The basic structure of CMUT is called a cell, which contains a top and a bottom electrode. The two electrodes are separated by a membrane and an insulating layer. A cavity structure within the insulating layer allows for membrane vibration. Cells become a CMUT element when multiple cells have common top and bottom electrodes. A CMUT transducer array contains multiple elements with electrodes separated. When CMUTs are used as an ultrasound transducer, they are biased with DC voltage to pre-deflect the membrane. Under transmit-mode, a pulse is applied to vibrate the membranes transmitting ultrasound. And under receive mode, the incoming ultrasound cause the membranes to vibrate, which induces a change in device capacitance and produces current. Transmit and receive mode operation can be switched for pulsing and echo detection.

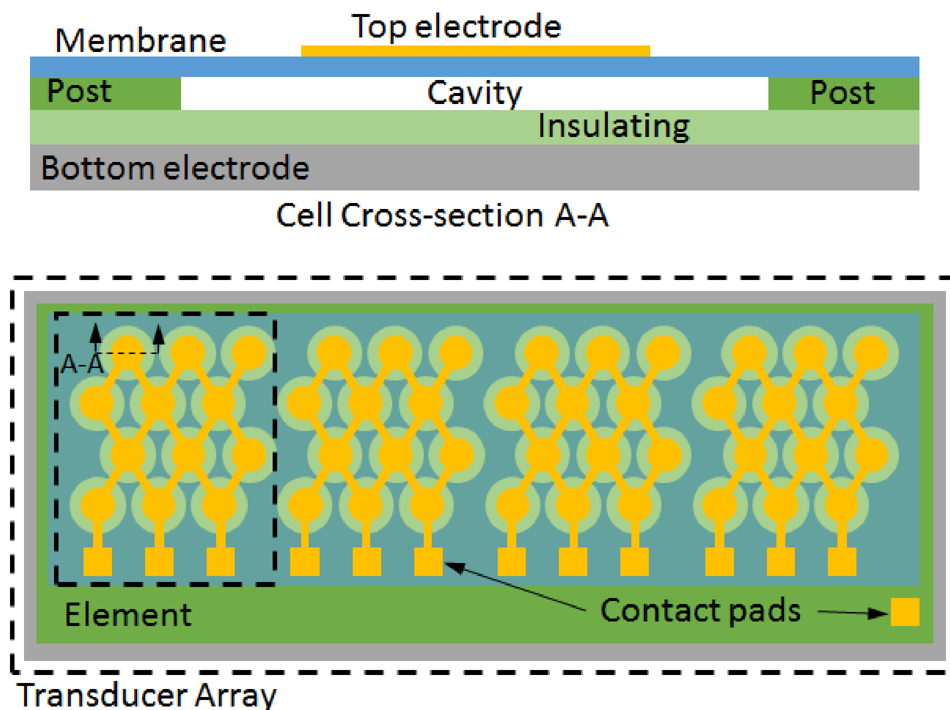

Figure 1: Illustration of basic CMUT structure

CMUTs were first introduced for air-coupled ultrasonic non-destructive testing (NDT) applications [1]. Later on, immersion applications using CMUTs, such as bio-medical imaging, became far more dominant [2-4]. Compared with piezo-based ultrasonic transducers, CMUTs have broader bandwidth that enhances lateral resolution in imaging applications [5]. Secondly, CMUT fabrication technologies are better at producing precise transducer arrays and miniaturized devices due to the use of microfabrication methods [6]. Furthermore, CMUT fabrication processes are potentially CMOS compatible once process temperature can be controlled to less than 400°C [7-9]. A CMOS compatible CMUTs can be fabricated directly on integrated circuits with advantages in transducer performance and device packaging [10-12]. As a result, CMUTs are an alternative to piezo-based transducers and attract major research interest. Besides medical imaging and NDT, CMUTs were also widely studied for extensive applications such as blood flow measurement, distance sensing, pressure sensing, fluid properties measurement and cancer treatment [3, 13-28].

CMUTs can also be used as resonators for gas sensing or biomolecules detection based on the gravimetric method [29-33]. For gas sensing applications, CMUT membranes can be coated with a layer of gas sensing film. When gas molecules are absorbed by the sensing film, a membrane mass change is induced, and the membrane resonance frequency will be shifted accordingly. The sensitivity to the gas concentration change is proportional to the resonance frequency [29]. Thus, high frequency CMUT arrays are able to achieve multiple gas detection with high sensitivity and low detection limit.

On the other hand, there are still limitations to the CMUT technology, such as relatively low output power in ultrasound transmission, dielectric charging induced performance durability, and membrane crosstalk [5, 6, 17]. Works for device optimization that tended to overcome the limitations also attracted research interests [28, 34-38]. However, all of the aforementioned studies required fabrication of CMUTs, which is difficult and expensive to achieve. Various reported CMUT fabrication techniques have limitations including but not limited to wafer cost, process complexity, restriction to dust-free fabrication environments, trade-offs between fabrication efficiency and device performance, process controllability and repeatability. As a result, the motivation of this project is to develop a CMUT fabrication process that requires low-cost and fewer fabrication constrains from both materials and

equipment standpoints. Moreover, the process should also leave enough space for other researchers to modify and optimize according to their applications.

1.2 Contribution and Thesis Organization

The major contribution of this thesis is the process development, demonstration and optimization of using patterned photosensitive polymer adhesive for CMUT fabrication through wafer bonding. Low-cost silicon nitride wafers were successfully bonded with silicon wafers without using chemical mechanical polishing processes in a weak-dust-controlled fabrication environment. Basic characterizations were performed including both in-air and immersion resonance frequency measurements and ultrasonic signal transmit and receive tests. The second contribution is on structure design toward improving the receive sensitivity of CMUTs. The designed novel structure enhanced the receive sensitivity to more than twice the sensitivity of CMUTs with the conventional structure illustrated in Figure 1. Lastly, the fabrication steps of the developed process are minimized. Therefore, the reported process is the simplest one compared with previously reported processes and results in lower cost and shorter turn around time. Moreover, methods on fabricating flexible CMUTs, 2D-array-CMUTs and CMOS integrated CMUTs are suggested based on the reported fabrication processes. As a result, not only the future students in our lab, but also all the other researchers can be guided on future works of polymer wafer bonding based CMUT fabrication and related applications.

This thesis will be presented as follows. In Chapter 2, conventional CMUT fabrication techniques are reviewed and discussed. Then, the objectives of fabrication toward achieving the research goal are given. After reviewing the fabrication techniques, in Chapter 3, the mechanism of adhesive wafer bonding is analyzed and discussed in order to provide guidance for the fabrication process design. At the end of Chapter 3, properties that relate to coating polymer adhesive on silicon wafer are characterized and discussed. Chapters 4 to 6 describe the three iterations of developing the polymer wafer bonding based CMUT fabrication process. The first iteration is a preliminary study demonstrating the fabrication feasibility and the capability of ultrasound generation and receiving. The second and third iterations are about the improvement and structure design for process optimization and function enhancement. Lastly,

Chapter 7 summarizes the achievement and proposes future works, including discussions on various CMUT structure design considerations. Moreover, though the focus of the research is on studying and developing the fabrication process of CMUTs, some of the theoretical calculations and models are still needed to evaluate and explain the performance of the fabricated transducers. Therefore, works that relates to the theoretical calculation and structure modelling are summarized and given in Appendix A.

Chapter 2 Literature Review and Methodology

Conventional ultrasonic transducers are based on piezoelectric effects and lead-zinconate-titanate ceramic (PZT) is one of the most commonly used piezoelectric materials for ultrasonic applications. PZTs have high electromechanical conversion efficiency, but it requires precise dicing, multiple impedance matching and acoustic backing layers and acoustic lenses for achieving specific operation frequency requirements, better impedance matching, larger bandwidth and beam focusing, respectively. However, these requirements sacrifice the acoustic power.

On the other hand, CMUTs, based on the structure of parallel plate capacitors, offer an alternative ultrasonic transducer solution. CMUTs generate and receive ultrasound through thin membrane vibration, which results in larger bandwidth and better impedance matching [5, 39, 40]. Precise transducer arrays can also be fabricated through CMUT technology by surface micromachining processes. Compared with PZTs, the fabrication process of CMUTs is also potentially CMOS compatible toward compact, miniaturized and low cost ultrasonic device design. However, the fabrication yield and cost, process compatibility with CMOS and transducer performance of CMUTs are still limited with practical issues, which will be reviewed and discussed in this chapter.

2.1 A Review of CMUT Fabrication Techniques

Conventional fabrication methods can be categorized as either surface micromachining or the wafer bonding method.

Surface Micromachining

The CMUT fabrication based on surface micromachining method has been extensively studied since its inception in 1994 [1, 41-54]. A general surface micromachining process is illustrated in Figure 2.

One of the keys in fabricating CMUTs is to achieve cavity structures that allow membrane to vibrate. In surface micromachining method, structures are deposited and patterned layer by

layer. Sacrificial material is first deposited inside the cavities prior to membrane deposition. Next, through-membrane holes (releasing holes) are patterned and etched in order for the sacrificial materials to be removed through a wet etch process. Cavities can be in vacuum by sealing the releasing holes through CVD processes that are processed in low pressure chambers.

When fabricating CMUTs using the surface micromachining method, trade-offs among fabrication efficiency, device performance, process controllability, and repeatability need to be made during the design process by adjusting factors such as the material selection for the sacrificial and membrane layer, the release hole geometry and placement, the etchant type, and structural design of the CMUT cells. Therefore, optimizing all of the design parameters and fabrication is not feasible. Furthermore, surface micromachined CMUTs also present a limitation in fill factor, which is the ratio of the CMUT area to the total aperture area, since release holes are patterned on the same membrane layer for removing the sacrificial layer [1, 6]. Consider that the cell area is inversely proportional to the operation frequency, the fill factor will decrease as the frequency increases since the diameter of releasing holes is limited to several micrometers. A small fill factor results in a low output power, receive sensitivity and thus signal-to-noise ratio.

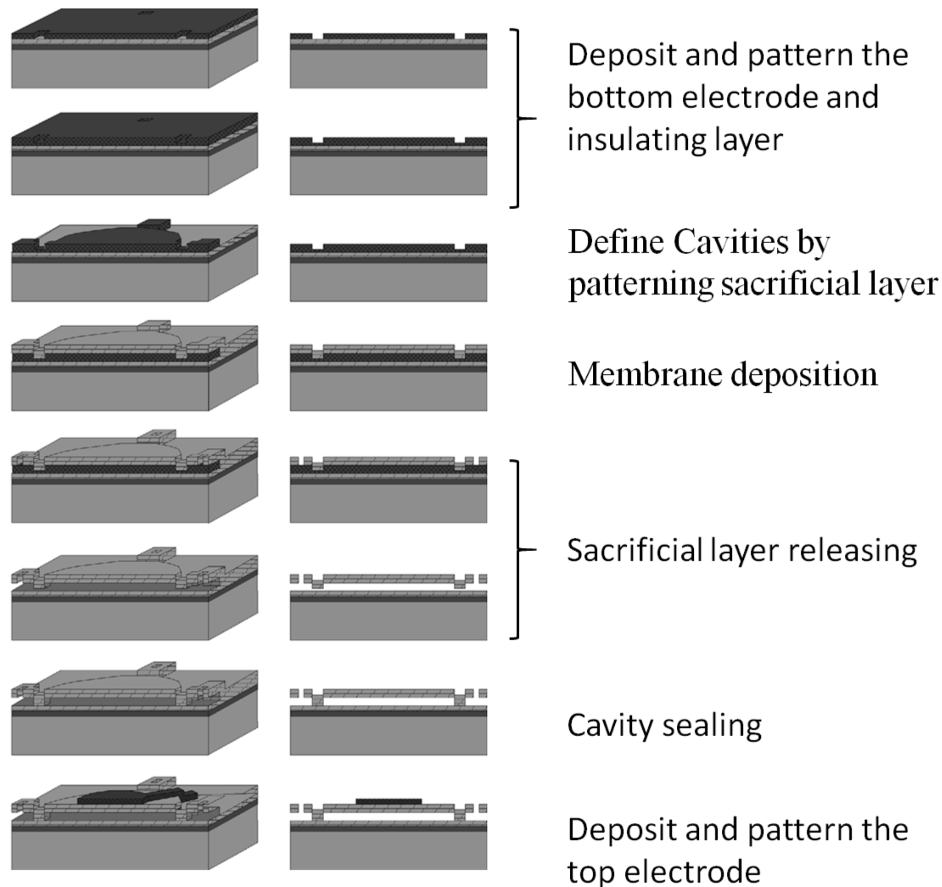

Figure 2: General surface micromachining process for CMUT fabrication [6].

Direct Wafer Bonding

The CMUT fabrication technique experienced a breakthrough in 2002 [55]. Membrane layer was directly attached on cavities through wafer bonding technique in a vacuum environment. Cavities are firstly patterned on one wafer (bottom wafer) while the membrane layer is deposited on another wafer (top wafer). When the top and bottom wafers are brought in contact, molecular bonds can be generated between two wafers forming strong bonds. This bonds can become inseparable if a subsequent high temperature annealing process is executed. The generic wafer bonding process is illustrated in Figure 3. First, the bottom wafer, which is a highly doped silicon wafer, goes in a high temperature furnace in order to grown an oxide layer on both surfaces. The top wafer is a silicon-on-insulator (SOI) wafer where the device silicon layer will be used as the membrane layer. The two wafers are then bonded via a wafer bonder at a high force followed by annealing at a high temperature to form covalent bonds.

The top wafer's handling layer and buried oxide layer are then removed via wet-etching and a vacuum cavity with suspending silicon membrane is achieved.

Compared with the surface micromachining method, the direct wafer bonding method does not require release holes and channels so that the CMUT's effective device area can be optimized with ease [5, 56]. The cavity depth can be shallower, which allows a lower DC bias since a stronger electrostatic force can be achieved. The cavity depth and diameter are defined during the patterning process and they are not affected by the remaining process steps, so fabrication repeatability and controllability can be achieved [6].

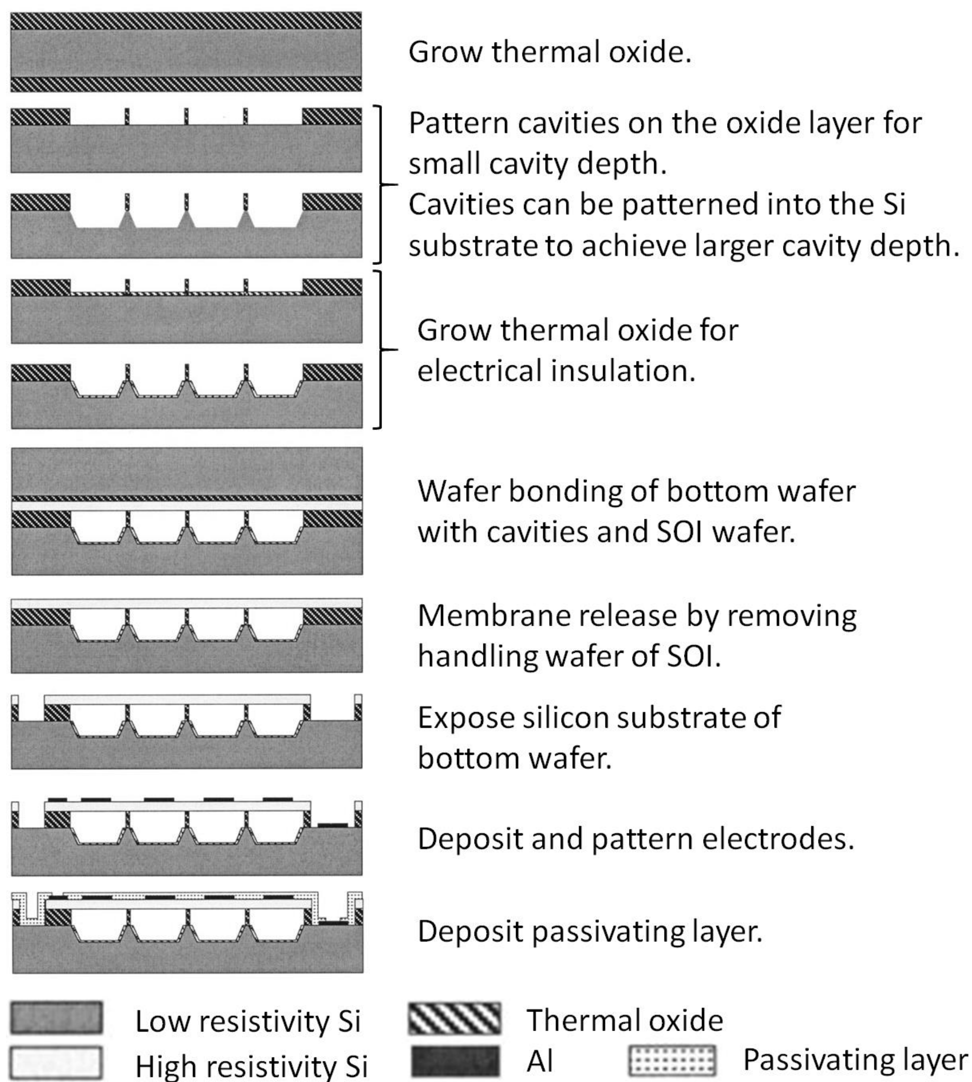

Figure 3: SOI-oxide wafer bonding process for CMUT fabrication [56].

Another direct wafer bonding method based on silicon nitride to silicon nitride (SiN-SiN) bonding was also reported for 1-D and 2-D CMUT array fabrication [5, 57]. The process is illustrated in Figure 4. Compared with the SOI to oxide wafer bonding method, SiN-SiN bonding enables fabricating CMUTs with an electrical-insulating membrane where as the silicon membrane layer is highly conductive. The benefits of using electrically insulating membrane will be discussed later in Section 2.3.

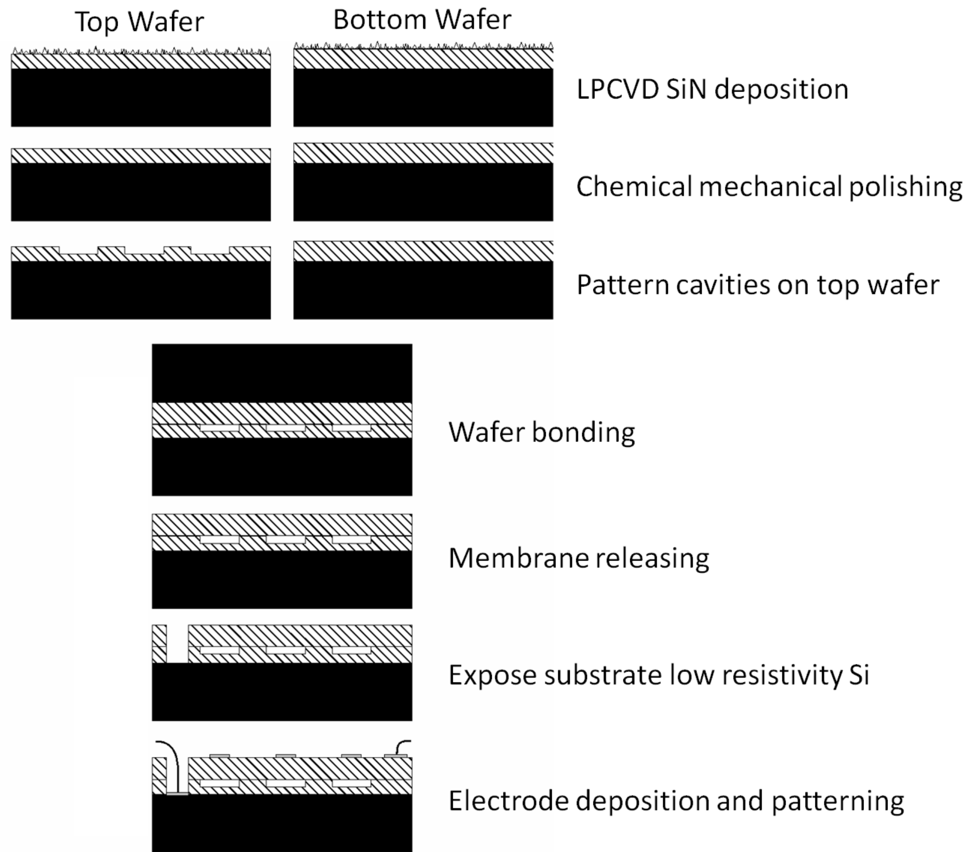

Figure 4: CMUT fabrication based on LPCVD SiN-SiN wafer bonding [58].

The main drawback of the direct wafer bonding is that the yield is highly governed by the wafers' surface roughness, which is typically minimized by either purchasing very expensive SOI wafers or processed wafers that underwent strict surface treatment such as chemical mechanical polishing (CMP) [5, 6, 56, 59]. Furthermore, the required annealing process, which typically operates at 800°C~1100°C, makes the fabrication process incompatible for CMOS fabrication [7]. A CMOS compatible process, where the maximum process temperature is under 400°C, could enable fabricating CMUTs directly on integrated circuits (ICs). An IC-

integrated CMUT would have dramatic advantages in transducer performance and device packaging. For example, parasitic effects can be minimized when the transducer is integrated with the receive circuit. Prior studies have introduced metallic intermediate layer and wafer surface treatments to avoid the high-temperature annealing process [8, 9]. However, these bonding processes still have costly requirements on the wafer bonding process [60]. Last but not least, SIMOX-based SOIs are extremely difficult to obtain for wafers under 8 inches. This means high quality and thin SOIs are not readily available. Majority of CMUT-appropriate SOI wafers but also suffer from significant variations in thickness.

Anodic Wafer Bonding

Anodic wafer bonding involves bonding alkali-containing glasses with silicon wafers through establishing an ion exchange under strong electrostatic field. The glass is connected with cathode and silicon is connected with anode. The alkali cations, which are typically Na+ or K+, move toward the cathode and create a layer called "cation-depleted layer" at the bonding interface. The silicon wafer act as an anode and the electrostatic field helps to pull the silicon towards the glass thus narrowing the gap between two wafers. Once the silicon surface is pulled strong enough with the cation-depleted layer, Si-O-Si bonds are generated such that permanent bonds are formed [7].

Recently in 2015, Yamaner et. al. reported a fabrication process based on anodic wafer bonding [59]. The process is illustrated in Figure 5. Although the use of anodic wafer bonding technique reduces the requirement in wafer surface quality at the bonding interface, the membrane is still the semiconductive silicon from the device layer of SOI wafer. Issues of high cost and uniformity of membrane layer are still not avoided. Furthermore, since the glass is non-conductive, a bottom electrode has to be patterned followed by depositing an insulating layer and a strong insulating material is difficult to be achieved in this method.

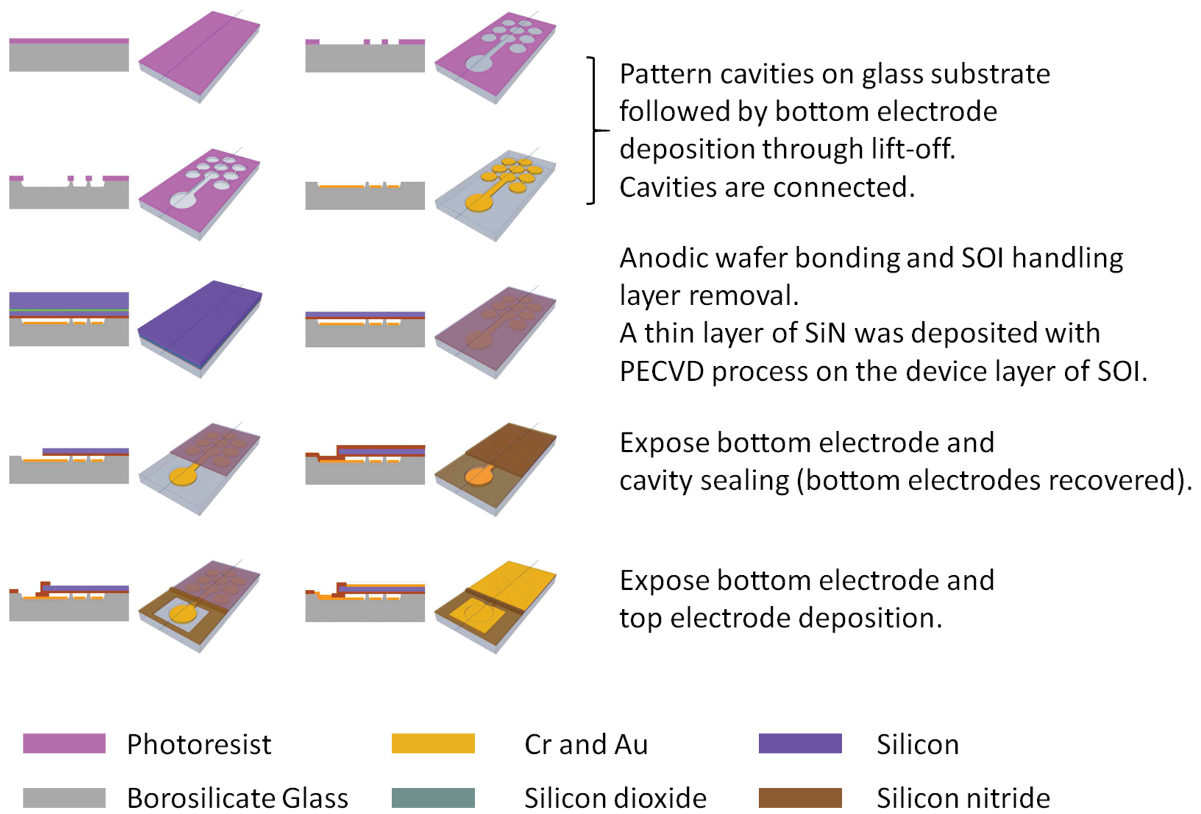

Figure 5: CMUT fabrication based on anodic wafer bonding [59].

Polymer Adhesive Wafer Bonding

Polymer-adhesive-based wafer bonding techniques are also proposed for CMUT fabrication [7]. Since the wafer surface is first coated with a polymer layer in liquid-phase, minor contaminations and defects on the wafer surface can be tolerated. The coated adhesive layer is then partially cured such that the adhesive transforms from liquid to solid phase. When the top and bottom wafers, which are both coated with partially cured adhesives, are brought into contact, they are bonded through an additional heat and compressive force until the adhesive is fully polymerized. There are four main advantages associated with the polymer bonding method [7, 61]. First, since the polymer prior to bonding is soft and conformable, the final bonding area between the wafers and the adhesive is maximized to enable a strong bonding force. For the case of the brittle silicon wafers, a significant wafer bow can reduce the bonding area. Second, the conformability of the polymer layer, prior to curing, results in low stress on the bonded wafer. Third, any surface defects or contaminations can be covered by the polymer, thus preventing the formation of voids or debonding. Lastly, the bonding temperature

is decided by the relatively low polymer curing temperature, which is usually less than 400°C [7]. Therefore, this technique is compatible with CMOS fabrication process.

The feasibility of using benzocyclobutene as polymer adhesive to fabricate vacuumed cavity structure for CMUT fabrication has been demonstrated by Bakhtazad et. al., and the process is shown in Figure 6 [62]. However, the fabrication still used SOI wafers and the process was not as noticeably simpler than the conventional direct wafer bonding method. Moreover, transducer characterization was not presented in [62].

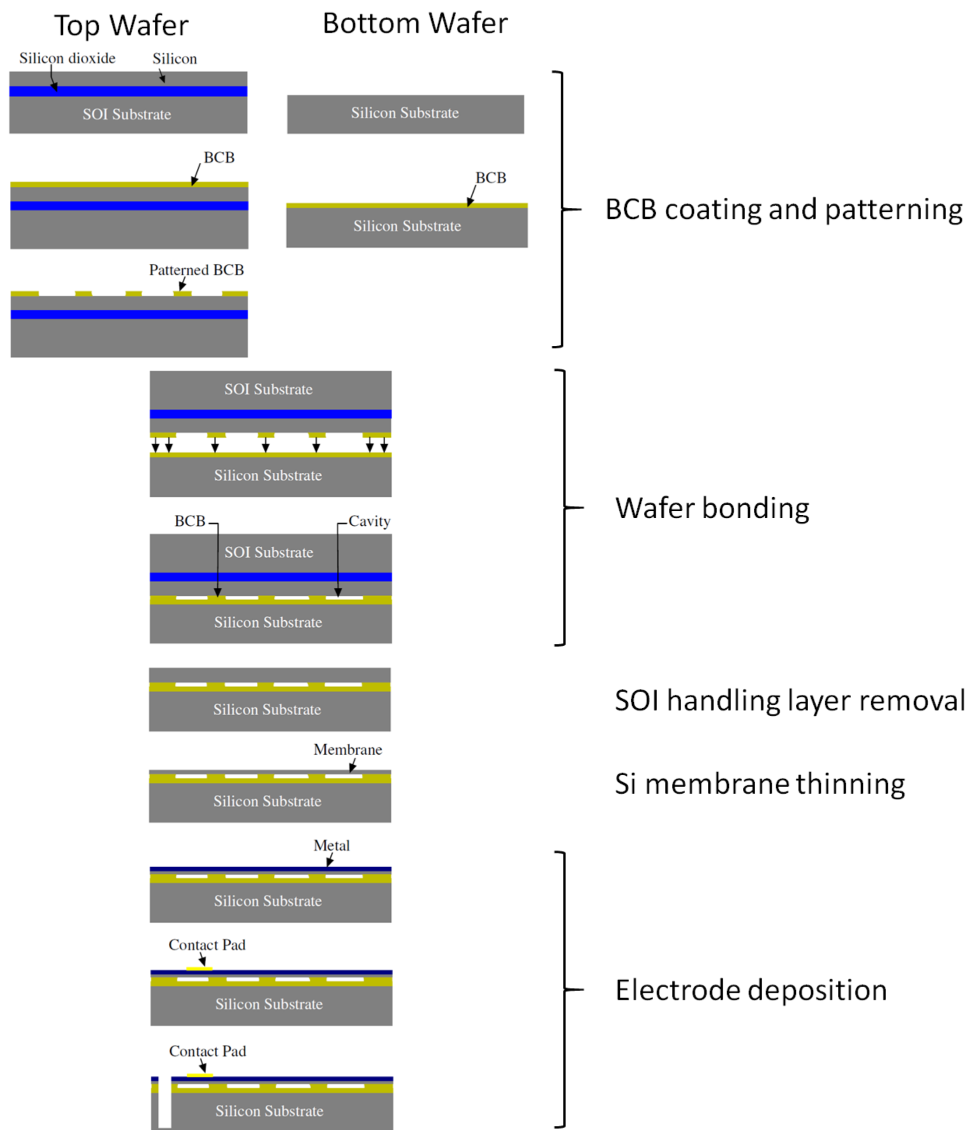

Figure 6: Vacuum sealed cavities fabrication process [62]. [1]

[1] © Springer. Reproduced with permission.

Comparison of Fabrication Techniques

The reviewed CMUT fabrication techniques in section 2.1 are the widely-adopted methods used by current researchers. Improvements based on these methods were also developed and reported [8, 36-38, 63]. However, these improvements and optimization methods did not show significant change in in achieving a vacuumed cavity structure, thus they are not discussed.

In order to compare fabrication techniques, one must consider not only the end performance of the CMUTs but also process cost, equipment limitations, process simplicity, design flexibility, and parameter accuracy control. Table 1 compares the reviewed fabrication techniques according to the criteria. The comparison was made mainly based on the information given by the published papers and partially based on the personal experience about material sourcing and cleanroom fabrication.

Table 1: Comparison among fabrication techniques

Criteria		Wafer Cost[1]	Equip. Lim.[2]	Simplicity[3]	Flexibility[4]	Para Acc. Ctrl.[5]
Surface Micromachining		Low	Medium	Complex	Low	Good
Wafer Bonding	SOI-Oxide	High	Low	Simple	Low	Good
	SiN-SiN	Low	High	Medium	Low	Good
	Anodic	High	Low	Medium	Low	Good
	Adhesive	Low	Low	Simple	High	Medium

The first criterion is the wafer cost. Wafer cost usually occupies a small percentage of total fabrication cost compared with the cost in accessing the equipment in clean room. However, the current use of SOI wafers are preferred by most of researchers who have interest in wafer bonding techniques. The cost of a 4”-SOI wafer (~$300 to $800) is about four to ten times more expensive than a 4”-out-sourced-LPCVD-SiN wafer ($70 to $80). The cost of LPCVD SiN wafers are more scalable than SOI wafers since the fabrication of SOI wafer itself requires an additional costly bonding step that is not done in the batches. LPCVD silicon nitride, on the other hand, can be deposited in trays of 25 wafers or higher. Furthermore, it is extremely difficult for researchers to fabricate their own SOI wafers. As a result, the cost of SOI make wafer cost an important criterion to compare.

The second criterion is about the limitation in equipment accessibility and usage cost. The equipment usage for each fabrication technique is given in Table 2. Adding more equipment

to the process increases the chance for error as there are many factors associated with the guaranteeing the outcome of a machine. Some machines are also not common. For example, a CMP machine for angstrom level surface finish is difficult to come by. Even if it is available, maintaining the machine to have fresh polishing chemicals and pads is often challenging. Outsourcing can be considered a way to reduce the equipment limitation, but it can easily increase the fabrication cost and lead time.

Table 2: Process details of reviewed fabrication techniques

	Lithography	Wet Etch	Dry Etch	Wafer Bonder	LPCVD Furnace	CMP machine	Annealing Furnace	Metal Deposition	PECVD Chamber
Surface Micromachining	Y	Y	Y		Y			Y	Y
SOI-Oxide	Y	Y	Y	Y			Y	Y	
SiN-SiN	Y	Y	Y	Y	Y/O	Y/O	Y	Y	
Anodic	Y	Y	Y	Y/A				Y	Y
Adhesive	Y	Y	Y	Y	OP/O			Y	

Y = Yes, it is required
Y/A = Yes, it is required, but it also requires additional settings, such as external electrical field.
Y/O = Yes, it is required, but it can also be out sourced.
OP/O = Optional, but if required, it can also be out sourced.
Empty = not required.

The third criterion is the simplicity of the fabrication process. In Table 1, the process simplicity is compared according to the number of factors that are related to the yield for achieving vacuumed cavities. Surface micromachining method requires carefully design of film thickness, release-hole diameter, release-channel dimension, selectivity of materials during wet etching and so on [6]. In comparison, wafer bonding methods has less constraints. Thus, the surface micromachining method is considered more complex. SiN-SiN bonding requires a CMP process before bonding and anodic bonding requires a machine that can apply external electric field at the same time of heating during bonding. As a result, SiN-SiN bonding and Anodic bonding are considered medium in simplicity level. SOI-Oxide bonding and adhesive bonding does not have extra treatment step or additional bonding requirement, so they are considered simple.

The fourth criterion is about the flexibility in structure design. Flexibility of a fabrication process can be interpreted as flexibility in selecting wafer material and structure design

parameters. As discussed in the previous review section, all fabrication techniques except adhesive wafer bonding are very strict in the compatibility of the wafer and deposition materials. Furthermore, trade-offs have to be made when applying surface micromachining method between fabrication feasibility and device performance. As a result, only the adhesive wafer bonding method can be considered as high in flexibility.

The last criterion is about the parameter accuracy control. It can be found from Table 1 that only the polymer adhesive wafer bonding method is evaluated as medium in parameter control.

Parameter accuracy control during design and fabrication process relates to the tolerance for controlling the structural dimension and material properties. Polymer adhesive has an inherent limitation in coating thickness and the applied chemicals and the temperature control during coating and curing process would greatly affect the material properties of the adhesive. Moreover, the deformation of adhesive and the resistance to wet-etch chemicals during fabrication process are also of significant concerns. The use of dry-etch BCB as polymer adhesive for wafer bonding is a good example showing the advantage and disadvantage in CMUT fabrication [62].

As reported by Bakhtazad et. al., the applied polymer adhesive is a Cyclotene 3000 series dry-etch BCB from Dow Chemical. According to the standard coating process instructed by the product specification, dry-etch BCB can achieve coating thickness in the range of 1 to 26 μm [64]. The cavity depth and insulating layer thickness of a CMUT depends on the thickness of the adhesive layers on the top and the bottom wafer, respectively. The intended bias voltage, collapse voltage and breakdown voltage when designing CMUT relies on the precision in controlling the cavity depth and insulating layer thickness, which can be from 100 nm to several micrometers depends on application needs. Therefore, the achievable coating thickness of dry-etch BCB cannot satisfy the thickness requirements in the range of 100 nm to 1 μm. Bakhtazad et. al. therefore reduced the viscosity of the dry-etch BCB by diluting it with organic solvent in order to reduce the coating thickness to as low as 200 nm. Using dilution agent is not a bad idea in reducing adhesive layer thickness, but the trade-offs of applying dilution agent still needs to be considered. Although it was not reported in [62], diluting agent removal is

difficult and time consuming. Residuals of the diluting agent lead to voids during bonding process and affect the structure properties. Different adhesives also require specific types of diluting agent. Thus, adhesive dilution is not an universally applicable method for thickness control and new methods are needed.

Another limitation of applying polymer adhesive for wafer bonding is about the deformation of polymer adhesive under compressive force during wafer bonding. Polymer adhesive is not only used for providing a permanent bond between two wafers, but also a part of CMUT structure. Compared with the materials involved in direct wafer bonding and anodic wafer bonding process, such as silicon, silicon oxide and silicon nitride, polymer adhesive presents a lower Young's modulus and larger Poisson's ratio. The compressive bonding force required for wafer bonding and the stress from the vibrating membrane during CMUT operation can both deform the adhesive layer. Although deformation effect was not reported in [62], it must be considered during design and fabrication process when applying polymer adhesive.

Even if polymer adhesive has limitation in coating thickness and material stiffness, the advantages of polymeric materials should not be ignored. Polymers are very flexible in coating, patterning and properties modification. Filler materials can be dispersed in the polymer matrix to reinforce the properties of polymer matrix [65-68]. Secondly, dilution strategy is not the best, but it still provides solutions in thickness control. Thus, polymers have great potential to be optimized for specific applications and their weakness compared with silicon-based materials are not permanent. Take both the advantages and disadvantages, polymer adhesive wafer bonding method was evaluated as medium for parameter control.

Selecting a Method for CMUT Fabrication

Through the comparison among reviewed fabrication methods according to the five criteria, it is not difficult to conclude that polymer adhesive wafer bonding method is a good candidate for achieving the research goal. It shows low cost, low equipment limitation, non-complicated process and high design flexibility. Nonetheless, applying polymer adhesive has difficulties in parameter control, and it will be the major focus in this research project.

2.2 Comparison and Selection of Adhesives

The first step in designing CMUT fabrication process using polymer adhesive is to choose an adhesive. There are different types of polymer adhesives reported for different applications including thin wafer handling, device packaging, and 3-dimensional structure fabrication [61, 69, 70]. Commonly used adhesives such as polyimide, wax, polydimethylsiloxane (PDMS), poly (methyl methacrylate) (PMMA) and photoresists are not difficult to access and commercial products are available. Moreover, Cyclotene 3000 and 4000 series benzocyclobutene (BCB) polymer from Dow Chemical Company has also been widely reported as good adhesive for void-free wafer bonding [61, 62, 71, 72]. In order to select one of the adhesives, following four concerns need to be firstly considered.

Concern 1: Commercialized Product

Using commercialized polymer adhesives can help standardize the fabrication process. By processing the material with standard processing steps, the material properties can be secured and therefore ensure the repeatability. In this regards, polyimide adhesive PI2555 from DuPont, PDMS prepolymer and curing agent set Sylgard 184 from Dow Corning, BGL series wax products from AI Technology Inc., and Cyclotene BCB products from Dow Chemical company are all mature commercialized product available in the market.

Concern 2: Achieving void free bonding

Void generation is a major concern in the wafer bonding process. Voids can be introduced by contaminations, surface defects, and outgassing during bonding. In regards to avoiding voids generation, adhesives that subject to out-gassing, solvent evaporation or any other by-products in the final curing step would considered not suitable. In this regards, polyimide-based adhesives are not considered [61]. Furthermore, using dissolving agent or diluting agent is a common way of applying polymer thin film coating. However, the applied organic solvent must be completely removed before wafer bonding, which is extremely difficult to achieve according to my previous experience using PMMA and PDMS. On the other hand, Cyclotene BCBs was reported as excellent adhesives for void free wafer bonding due to the features of low stress and no out gassing during curing.

Concern 3: Temperature and chemical resistance

Wet etch and lithography processes are needed after wafer bonding steps. Processing temperature can go up to 120°C if apply AZ3312 positive for patterning. Wet etch solutions, such as potassium hydroxide (KOH), metal etchant (contains mainly water and acids such as acetic acid or nitric acid), or wafer cleaning bases (acetone and isopropanol) should not attack the adhesive in order to avoid debond due to adhesive loss. In regards of temperature and chemical resistance, adhesives including positive photoresist, wax and PMMA are considered not suitable.

Concern 4: Feature Patterning

As an intermediate layer between membrane (top wafer) and bottom electrodes (bottom wafer), the adhesive needs to provide electrical insulation while accommodating cavity patterning. The cavity patterning step should be applied before wafer bonding; thus, the patterning procedure should not affect the bonding efficiency. Dry etching accompanied with extra patterned photoresist layer is one of the solution for cavities patterning. Cyclotene 3000 series BCB is considered as one of the best choices for dry-etch cavity patterning. However, if the adhesive layer itself is photosensitive, cavities can be one-step patterned with lithography process with no need of extra layer of photoresist and extra dry/wet etching step. Therefore, using photosensitive adhesive such as SU-8 or Cyclotene 4000 series BCB (photo BCB) will be preferred.

Concern 5: Permanent Bonding

Wafer bonding step is to achieve permanent bond between two wafers. Photoresist based wafer bonding usually presents weaker bonding force since two bonded wafers can be separated by mechanical force [61]. Wax products were mostly developed to achieve temporary bond for applications such as ultra-thin wafer handling. In comparison, adhesives such as polyimide and BCB are usually used for permanent bonding. Wafers are not able to be separated unless broken the wafers.

Choose Adhesive for CMUT Fabrication

According to the aforementioned five concerns, the ideal polymer adhesive for this research should be a commercialized product that features the following properties:

- Photosensitive
- Generate permanent bond
- Temperature and chemical resistance
- Prevent by-product during polymer curing

Cyclotene 4000 series photosensitive BCB polymer adhesive perfectly matches with the features and therefore, it is chosen for developing the CMUT fabrication process.

2.3 Wafers for Bonding

Two wafers are needed for wafer bonding. The bottom wafer is usually the substrate. If a highly-doped silicon wafer is used as bottom wafer, the bottom wafer can be directly used as the bottom electrode when designing one dimensional CMUT array. On the other hand, membrane layer is usually pre-deposited on the top wafer. Most of the wafer bonded CMUTs use SOI wafer as top wafer. The device layer, which is a layer of highly doped silicon, is the membrane layer and serves as the top electrodes. In comparison with semiconductive membrane, electrically insulating LPCVD silicon nitride is popular choice as a membrane material when CMUTs are fabricated with surface micromachining or SiN-SiN fusion bonding methods.

Conventionally, there are two benefits by using electrically insulating membrane 1) Electrode size can be optimized to further improve the transduction efficiency; and 2) Parasitic capacitance can be minimized [5, 35, 73]. There is one more benefit that was recently found from the needs of fabricating annular CMUT array [28]. Elements of annular CMUT array have to be arranged concentrically. If highly doped silicon was used as the membrane, through-membrane trenches need to be etched for isolating neighbored elements. Wires for connecting inner annular elements and bonding pads therefore need to go across outer elements and the deep trenches. Metals such as Cr/Au or Cr/Al are usually evaporated with thickness of around 100 nm to 200 nm and patterned through lift-off process to make the connecting wires. The metal deposition at trenches requires good step coverage, or else the metal at the corner could

be very thin and may be damaged due to the accumulated heat generated by the pass-by-current. However, if electrically insulating membrane is used, at least one lithography step and one etching step can be removed from the fabrication process by avoiding trench etching. Deposited metal wires between elements and bonding pads also become durable with no need of going across the trenches.

The reason that most researchers still prefer silicon membrane might be due to the restriction of wafer surface roughness to achieve direct wafer bonding. Silicon nitride membrane require CMP before wafer bonding, which is not easy to achieve. However, adhesive wafer bonding has very good tolerance to wafer surface roughness, contaminations and defects. There will be no need to use CMP even if silicon nitride is selected as membrane material. As a result, silicon wafer with silicon nitride deposited through LPCVD process is chosen to be used as top wafer.

2.4 Objectives

In summary, this project aims at designing a CMUT fabrication process based on a polymer adhesive wafer bonding process. The CMUT will have highly doped silicon as substrate/bottom electrode. The top wafer will be a silicon wafer with a layer of LPCVD silicon nitride deposited and this LPCVD silicon nitride layer will be used as CMUT membrane. No polishing operation will be performed on the silicon nitride surface. Conventional wafer bonding techniques are not able to achieve such a bonding between silicon and non-polished silicon nitride wafers, so cyclotene 4000 series photosensitive BCB will be used as adhesive for wafer bonding. As this is the first report of its use in CMUT design, various parameters that govern the electrical, mechanical, and acoustic properties will be studied. Fabrication challenges in controlling cavity depth and insulating layer thickness will also be addressed.

Chapter 3 Process Study

The CMUT fabrication process is based on adhesive wafer bonding using photosensitive benzocyclobutene (photo BCB) polymer. Basic idea about using photo BCB for wafer bonding is to apply the non-cured or partially cured photo BCB on two wafers separately. When two wafers are brought into contact, cross-linking among monomers of photo BCB are formed by applying compressive force and heat, which enable bonding of two wafers. Furthermore, in order to fabricate CMUTs, one of the photo BCB layers will be patterned with cavities before bonding. Thus, photo BCB will be both the insulating layer and the structural layers.

Before going into structure design and fabrication process development, the mechanism and processing issues that are related to apply photo BCB were studied. Thus, the related chemical reactions in BCB coating, patterning and polymer curing processes will be firstly discussed in this chapter. Second, since photo BCB is spin-coated on the wafer, the CMUT structure dimensions, which depend on the film dimension of photo BCB, will be controlled by spinning parameters. As a result, the photo BCB coating process was experimentally studied and the results will be reported in the second portion of this chapter. Lastly, based on the process study, considerations about structural dimensions will be discussed at the end of the chapter.

3.1 Chemistry in BCB Coating and Wafer Bonding Process

There are two types of BCB products: 1) Cyclotene 3000 series dry-etch BCB that can be patterned with another layer of patterned photoresist followed by RIE; and 2) Cyclotene 4000 series photo BCB, which itself can be patterned in a way that is the same as negative photoresist. Photo BCB was developed based on dry-etch BCB by adding photoreactive crosslinker. However, the additional features brought by negative reactive crosslinker simplified the BCB patterning process and allows unique performance during wafer bonding process.

The coating-patterning-bonding procedures of dry-etch BCB and photo BCB are briefly summarized in Figure 7. The illustration of the process was also given by Oberhammer et. al. [74]. The major differences between the two are about their patterning methods and the

requirement of annealing process, which is to generate reflow of coated BCB and improved the coating uniformity. Both dry-etch BCB and photo BCB are spin coated on the wafer surface. The photo BCB can be patterned immediately after coating with photo lithography process but the dry-etch BCB needs to be patterned after the annealing process, which would require about 4 hours including the heating and cooling process.

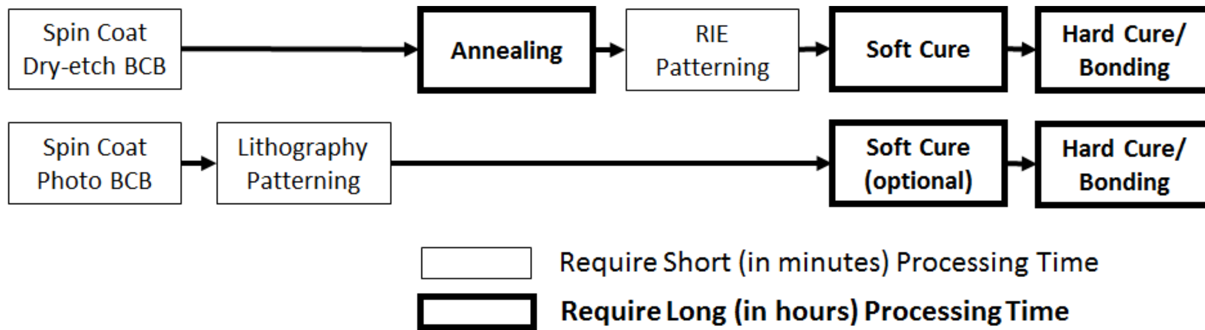

Figure 7: Coating-patterning-bonding process comparison between dry-etch BCB and photo BCB

The last two steps for achieving wafer bonding are soft cure and hard cure/bonding. The soft cure is to achieve cross linking by certain percentage of the BCB monomers. This is needed to avoid generating voids during wafer bonding when using dry-etch BCB. The hard cure/bonding enables complete crosslinking of BCB monomers. Wafers can be bonded after this process when compressive force is applied. Both soft cure and hard cure require long processing times, typically in hours. Detailed explanation about the chemical reactions during coating and curing processes are reviewed and summarized.

Adhesive Promoter

Adhesive promoter AP3000 is recommended to be applied as an intermediate layer between BCB and substrate with several nanometers in thickness. According to the material safety data sheet, AP3000 contains mainly propylene glycol monomethyl ether and other components including organosilicate polymer, water and 2-methoxy-1-propanol [75]. When applying AP3000 to wafer surface, Si-O or Si-OH bonds are generated on the silicon or silicon nitride surface through the condensation of silanols [76]. On the other side of the AP3000 layer, the covered organosilane has better connection with the later coated BCB layer.

BCB Curing

According to the publications from Dow Chemical, the dry-etch BCB is B-staged DVS-bis-BCB in mesitylene [77]. Mesitylene residual can be removed during soft bake process after spin coating. The formula of DVS-bis-BCB is given in Figure 8. The monomers start thermal polymerization when it is heated up. As shown in Figure 9, curing process of DVS-bis-BCB is mainly the Diels-Alder reaction. Monomers can also dimerize or polymerize when it is lack of dienophiles [78].

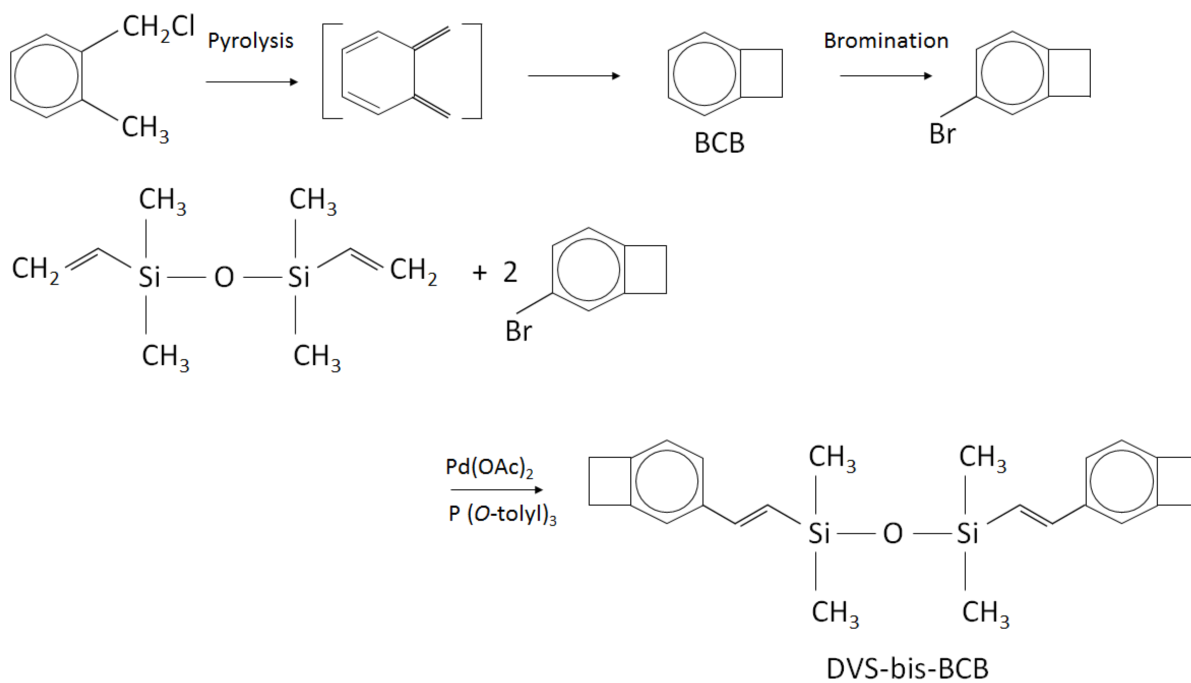

Figure 8: Monomers of BCB and DVS-bis-BCB [77, 78]

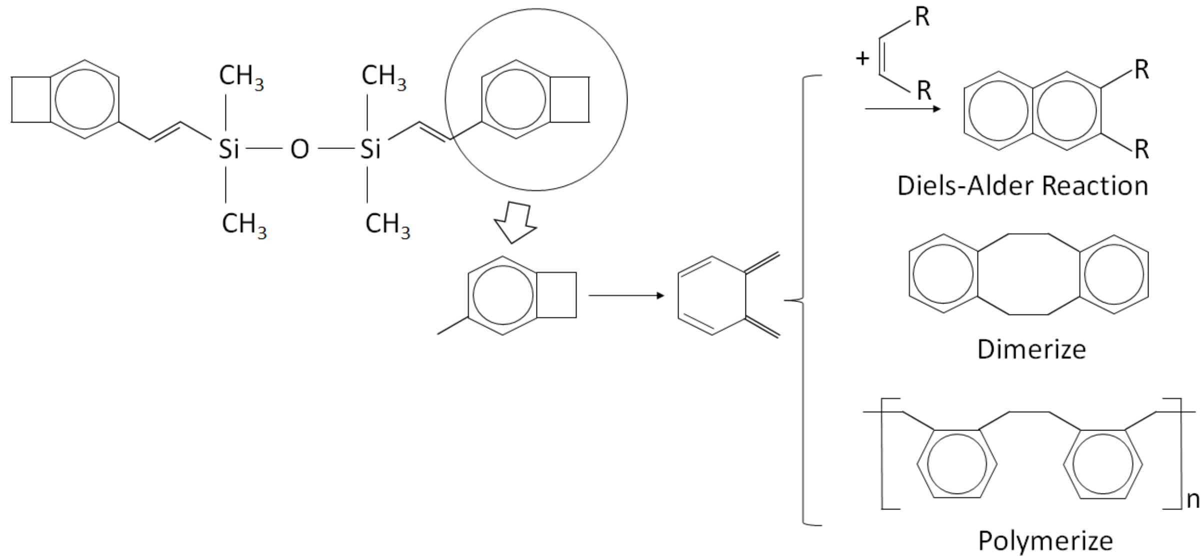

Figure 9: Reactions during BCB curing process [78]

Photosensitive reaction in Photosensitive BCB

By adding bis-aryl azide, as shown in Figure 10, the product becomes photosensitive with negative reaction [77]. Bis-aryl azide produces nitrene under UV irradiation [79]. The highly reactive nitrenes then cross link with trans vinyl. As a result, the B-staged DVS-bis-BCB combined with bis-aryl-azide can be patterned with masked UV exposure.

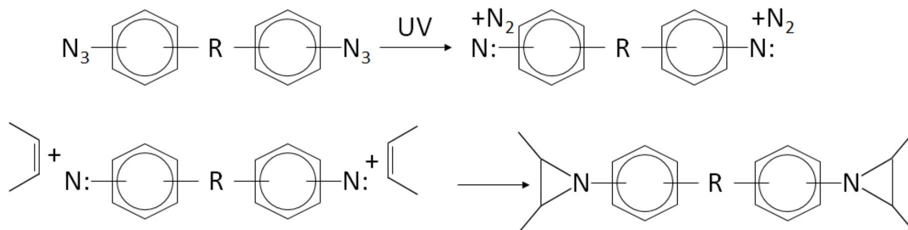

Figure 10: bis-aryl azide and its reaction under UV exposure [77, 79]

According to the reactions happening in BCB curing process, it is considered that the wafer bonding through BCB is achieved based on the following two aspects:

1. Wafer surface with silicon based materials (silicon, silicon oxide, silicon nitride and so on) bond with BCB through adhesive promoter. Si-O or Si-OH bonds are generated between the silicon based materials and the adhesive promoter, while organosilane groups in the adhesive promoter could provide strong covalent bond with BCB.

2. Two wafers are both coated with BCB, thus the two BCB layers are bonded with each other during full curing process through cross linking among monomers of the two wafers.

3.2 Experimental Study: Chemical Group Characterization

According to the previous analysis, it is considered that the cross linking among BCB monomers is the key factor of achieving success bonding between two BCB films. Therefore, effects of any thermal treatments to the bonding of BCB films can be inspected by checking the key chemical groups that are related to the crosslinking process of BCB monomers. Fourier Transform Infrared Spectroscopy (FTIR) can be used to identify the infrared absorbance spectrum of different chemical groups within the polymer. By inspecting BCB films after different processing steps using FTIR, the process can be determined if it is suitable for processing BCB film.

Sample Preparation

A 4-inch boron-doped silicon wafer in <100> orientation with a thickness of 500 µm and resistivity of 0.001 Ω-cm was diced into small pieces in size of 1.5 cm by 1.5 cm. The test piece was used as substrates for BCB coating. The adhesive promoter was firstly coated on a silicon wafer test piece. The coating recipe was 3000 RPM for 15 seconds. The wafer was then baked on the hotplate under temperature of 120°C for 1 minutes. After applying adhesive promoter on another silicon test piece, BCB was spin-coated by recipe of 500 RPM for 10 seconds followed by 5000 RPM for 30 seconds. The wafer was then baked on the hotplate under temperature of 60°C for 1.5 minutes. The wafer was directly exposed under UV with energy of 3mJ/cm^2 and then baked on the hotplate under temperature of 50°C for 1 minute.

Processing Techniques and Thermal Treatments

1) Soft Cure:

The sample was placed in a vacuum oven. The oven temperature was increased from room temperature to 190°C and hold for one hour. The sample was then cooled down back to room temperature. According to the data provided by Dow Chemical, this process is to achieve cross linking level of around 50%.

2) Hard Cure:

The sample was placed in a vacuum oven. The oven temperature was increased from room temperature to 150°C and hold for 15 minutes. The temperature was then heated up to 250°C and hold for one hour. The sample was then cooled down back to room temperature.

Key Chemical Groups / Bonds

The FTIR results of the sample after coating, soft cure and hard cure are given in Figure 11. Both the non-patterned BCB and reference BCB samples were FTIR-inspected and no difference were found. Important IR peaks are summarized and analyzed in Table 3. The observed peaks show coincidence with the FTIR results provided by Dow Chemical so that the material handling and processing method is considered as valid [80].

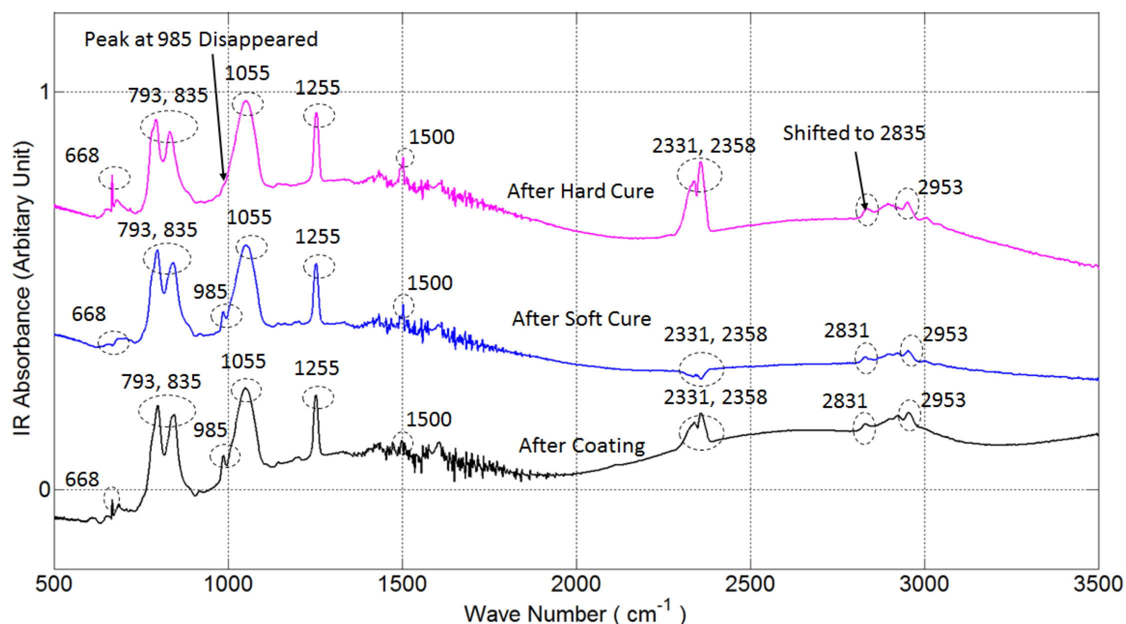

Figure 11: IR Absorbance spectrum of the BCB film after coating, annealing and curing processes.

Table 3: Absorbance IR peaks summary and corresponding vibrations [81-84]

Peak (cm^{-1})	Comments	
668	Carbon dioxide (O=C=O) gas in the measurement environment.	
793	Si-O bend	
835		
985	Trans vinyl group, appeared only in the spectrum of BCB sample after coating and after soft cure. This peak disappeared after hard cure due to the consumption of trans vinyl during the cross linking process of BCB monomers.	
1055	Si-O-Si	
1255	Si-CH3	
1500	Aromatic C=C stretch	
2331	Carbon dioxide (O=C=O) gas in the measurement environment.	
2358		
2831	Methylene C-H stretching	Peak of 2831 was found only in the spectrum of BCB sample after coating and after soft cure. The peak 2835 was found only in the spectrum of BCB sample after hard cure. The peak shift from 2831 to 2835 indicates the cross linking of BCB monomers.
2835	Tetrahydronaphthalene	
2953	$Si\text{-}(CH_3)_2$	

As discussed in section 3.1, photo BCB films on two wafers to be bonded need monomers to generate crosslinks before the wafer bonding step. According to the FTIR spectrums in Figure 11 and the analysis in Table 3, the absorbance peak that relates to BCB crosslinking process is at 985 cm^{-1} and shifting of 2831 cm^{-1} to 2835 cm^{-1}. In other words, if samples are

inspected with FTIR and do not show peaks of 985 cm^{-1} and 2831 cm^{-1}, the samples might not have enough monomers toward success wafer bonding.

3.3 Photo BCB Coating

In general, process of photo BCB coating and patterning is very similar to negative photoresist, such as the AZ nLof 2035, which contains spin coat, soft bake, UV exposure, post exposure bake and developing. During UV exposure, the UV-irradiated portion of photo BCB remains after developing. On the other hand, the non-exposed portion will be removed by developer forming patterns. As a result, the photo BCB film that is to be used as insulating layer on one of the wafers does not require feature patterning, so the entire wafer with photo BCB coating will be exposed with UV irradiation and there is no need of developing. On the other hand, the photo BCB coating on another wafer need to be patterned with cavities. Thus, photo mask is needed during UV exposure and developing process is also required. Consider the process-difference, even though the difference is minor, processes for preparing both the patterned and the non-patterned photo BCB film were studied separately.

One of the focuses of studying photo BCB coating is to investigate the coating thickness, which highly depends on the applied spinning parameters. In general, the higher spin rate and the longer spin duration, the thinner the coating thickness. More specific, factors such as the quantity of applied photo BCB on wafer surface before spinning, the environment temperature and humidity, the spin acceleration speed and even different spinner could also alter the resulting thickness. Therefore, the spin parameters given in this subsection can be used by other researchers only as a reference. Researchers need to develop their own spinning recipes. The discussion in this subsection therefore focus on general properties instead of specific numbers of thickness measurements.

3.3.1 Non-patterned Photo BCB Film

Sample Preparation

The silicon wafers used for BCB coating are 4-inch boron-doped silicon wafers in <100> orientation with thickness of 500 μm and resistivity of 0.001 Ω-cm. The wafers are the same

as the one that was used as bottom wafer for CMUT fabrication. Adhesive promoter AP3000 was first spin-coated on the wafer surface with a spin rate of 3000 RPM for 15 seconds. After baking the wafer at 120°C for 30 seconds, the photo BCB was then spin-coated with different spin rate toward different coating thicknesses. Photo BCB with volume of 5 mL was dropped on the wafer surface covering two thirds of the wafer area. Two spinning rates were applied: 1) 500 RPM for 10 seconds followed by 5000 RPM for 30 seconds to achieve a thinner BCB film; and 2) 500 RPM for 10 seconds followed by 3000 RPM for 30 seconds to achieve a thicker BCB film. After soft baking at 60°C for 90 seconds, the wafers were directly exposed in its entirety to UV light with exposure energy of 3 mJ/cm^2 and no photo mask was applied. Post exposure bake at 50°C for 1 minute was then applied to the wafers.

The thickness and stress distribution over entire wafer were firstly measured with ellipsometer after spin coating process. Soft curing process was then applied to both the wafers. The soft curing was done in vacuum oven. The wafers were face-up placed in the vacuum oven at room temperature. Three-time nitrogen-charge-vacuum process was firstly applied to remove oxygen. The wafers were then heated up to 190°C and maintaining for an hour followed by cooling down process in vacuum.

Thickness Measurement

The thickness distributions of the coated BCB layers using different spin rates, before and after soft curing process, were compared in Figure 13. The average thicknesses and standard deviations of the measurement points are summarized and compared in Table 4.

The ellipsometer measured the thickness of transparent film by inspecting the reflection index change corresponding to the change in thickness. It can be found from the Figure 13 that there are some measurement positions showing significant different measurement results compared with other measurement positions. The corresponding reflection indexes were also much more different from the others. These were considered induced by the contaminations on the wafer and were not taken into account when calculating average thicknesses and standard deviations. As shown in Figure 12, for any dust appearing on the wafer before spin

coating, the surrounding film would undergo significant thickness change. Also, if the light was spotted on the contaminations, measurement results will be greatly affected.

According to the results in Table 4, it can be firstly concluded that better thickness uniformity can be achieved with slower spin rate. Secondly, soft curing process caused film shrinkage and the coating uniformity was much improved. It has to be mentioned that the exact thickness also depends on the amount of BCB dropped on the wafer before spinning. Based on the experience during fabrication, 2 mL of BCB dropped on wafer is the minimum amount that can fully cover the wafer surface after spinning. By increasing the BCB volume, coating thickness can be increased accordingly. The use of 5 mL-photo BCB therefore achieved a thicker coating.

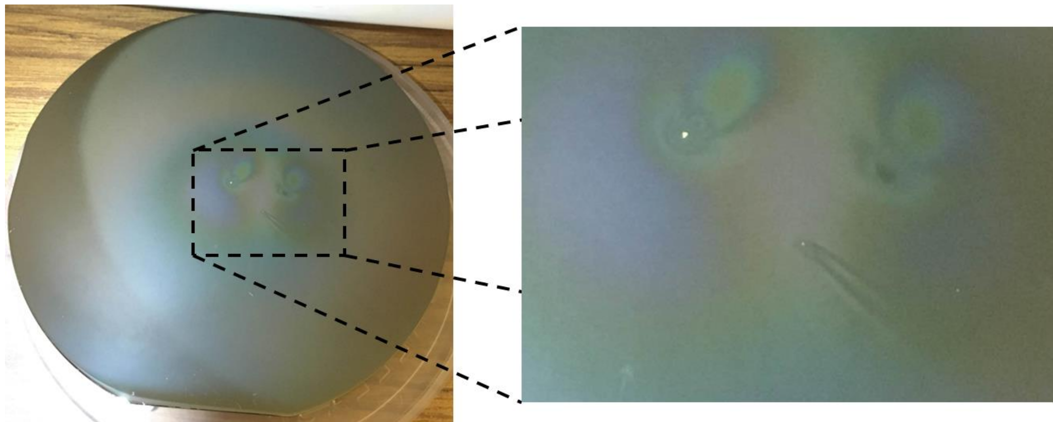

Figure 12: Photo of BCB coated silicon wafer with spin rate of 3000 RPM. Contaminations caused thickness variations.

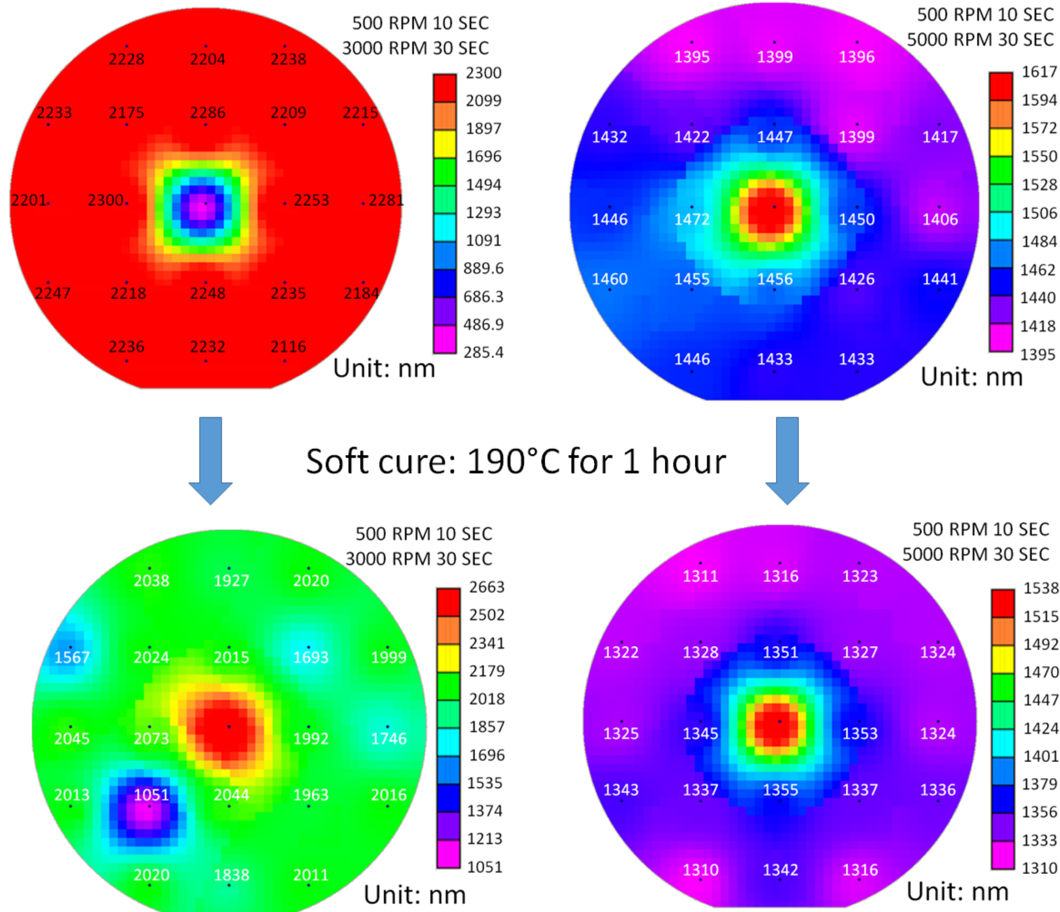

Figure 13: Thickness distribution before and after soft cure with different spin rate.

Table 4: Ellipsometer measurement results: average thickness and standard deviation.

	3000 RPM			5000 RPM		
Soft Cure	Before	After	Decrease	Before	After	Decrease
Average Thickness	2221.9 nm	2013.3 nm	9.39 %	1440.4 nm	1331.3 nm	7.57%
Standard Deviation	40.3 nm	34.8 nm	n/a	46.4 nm	13.8 nm	n/a

Stress Analysis

Figure 14 summarizes and compares the BCB coating induced stress on wafers. The wafers right after spin coating appeared low stress (± 20 MPa) distribution and the thicker film induced slightly higher average stress. After applying soft curing process with elevated

temperature up to 190°C, the stress distribution appeared more uniform while the average stress was increased to around 22 to 24 MPa, which is closer to the reported values (28±2 MPa) in the specification of the product.

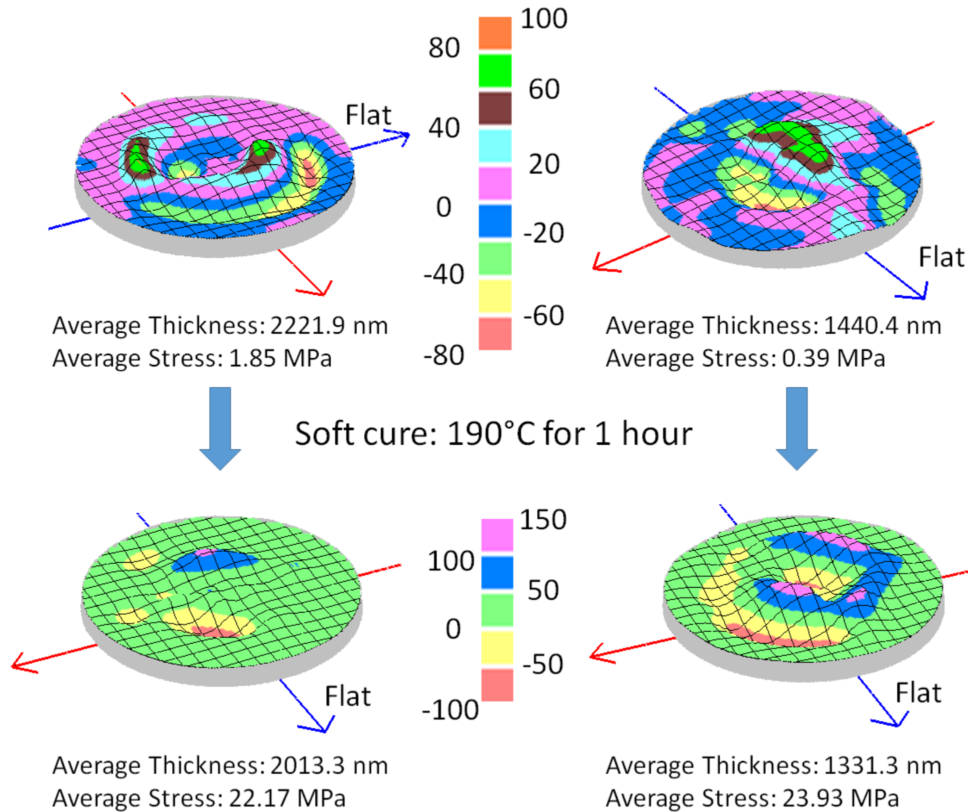

Figure 14: Stress map of wafers with different BCB thicknesses before and after soft curing process.

3.3.2 Patterned Photo BCB Film

Sample Preparation

The process for preparing patterned photo BCB film has no difference from the one for non-patterned one before the step of UV exposure. Thinner photo BCB film will benefit CMUTs with better receive sensitivity and lower bias voltage, so only 5000 RPM spin rate was applied for film inspection. During UV exposure, photo mask with patterns of cavities (circular-shape-dots with diameter of 50 μm) was applied to partially irradiate the photo BCB film. After post exposure baking at 50°C for 1 minute, puddle developing step was applied to remove the unexposed photo BCB and having cavity structure appeared.

Cavity Depth

The cavity depths on different positions of the wafer were measured with profilometer after puddle developing. The soft curing process was performed in the same way of the one for the non-patterned film. Cavity depths were then measured again to inspect the effect of soft curing on the patterned photo BCB film. Measurement positions are illustrated in Figure 15. Positions during two different profilometer measurements, before and after soft curing, cannot be controlled precisely to be the same. The positioning error is estimated of about ±5 mm.

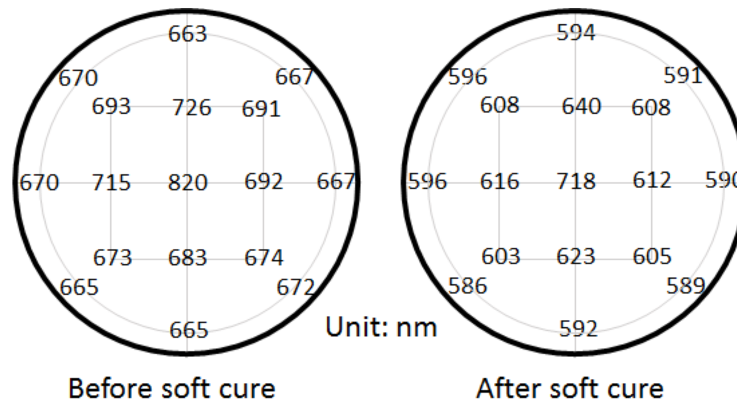

Figure 15: Cavity depths on difference location of the wafer before and after soft cure were measured with profilometer. The measurement results are marked at the corresponding measurement location that are illustrated in this figure.

The measurement positions are categorized into three regions: wafer centre, half wafer-radius and wafer edge. Average cavity depths of the three regions are summarized in Table 5. It can be found that wafer centre appeared the deepest cavity, which the depth decrease from centre to the edge. The cavity depths also decrease after soft curing by about 11% to 12%. On the other hand, when compare the cavity depths with the non-patterned photo BCB film with spin rate of 5000 RPM, whose measurement results were given and summarized in Table 4 and Figure 13, it is found that the film thickness is much thinner and appear larger percentage in thickness decrease after soft curing.

Table 5: Summary of cavity depths and depth decrease percentage.

Regions	Before Soft Curing	After Soft Curing	Average Depth Decrease
Wafer Centre	820 nm	718 nm	12.44%
Half Wafer-radius	693±19 nm	614±12 nm	11.37%±1.54%
Wafer Edge	667±3 nm	592±3 nm	11.33%±0.6%

3.4 Summary of Process Study

The discussion and experimental results given in this chapter are useful for guiding CMUT structure design and fabrication process development. The wafer bonding mechanism was firstly discussed and the discussion pointed out the key chemical groups that relate to successful wafer bonding. FTIR characterization were used to identify the chemical groups. By inspecting FTIR spectrums of the photo BCB sample after thermal treatments, one can determine if the thermal treatments affect the properties of photo BCB toward wafer bonding.

Second, coating of photo BCB by spin coating were studied and discussed. Based on the given spinning parameter, photo BCB film was found thicker in the wafer centre and thinner at the edge of the wafer. Soft curing process could improve the coating uniformity and decrease the film thickness, but wafers with soft cured photo BCB films should still be able to be bonded according to the FTIR results. It was also noticed that patterned photo BCB film appeared thinner than the film with no patterns. This must be taken into account during structure design.

Moreover, knowing the thicknesses of the spin coated patterned and non-patterned photo BCB films, one can have an roughly concept on the thickness of insulating layer and the cavity depth in a typical CMUT structure, as illustrated in Figure 1. However, compressive force is needed during the wafer bonding step, so the final achieved insulating layer thickness and the cavity depth can only be measured after the wafer bonding step by inspecting the cross-section structure.

Chapter 4 First-Generation Adhesive Wafer Bonded CMUT

The goal of the first-iteration for process development was to demonstrate the feasibility of using photo BCB for CMUT fabrication. The fabrication steps were minimized in order to minimize the unexpected factors. The resulted first-generation CMUTs were characterized with in-air and immersion tests for exploring the issues that related to applying BCB. The reported work in this chapter with majority of its work was also described in [85, 86]. [2]

4.1 Fabrication Process

The bottom wafer is a 4-inch boron-doped silicon wafer in <100> orientation with a thickness of 500 μm and resistivity of 0.001 Ω-cm, which allows the bottom wafer to be directly used as the bottom electrode. The top wafer is another 525 μm thick <100> orientated boron doped silicon wafer. A 600- nm-thick low stress (< 200 MPa) stoichiometric silicon nitride layer was deposited on the top wafer by LPCVD process, which was performed by University Wafers Company. Photo BCB (Cyclotene 4000 series, Dow Chemical) is used as both the bonding adhesive and the insulating structure [87]. The chemicals AP3000 and DS2100, which are also from Dow Chemical, were applied for photo BCB coating and patterning. AP3000 is an adhesive promotor that is applied between the BCB and the wafer surfaces to improve the adhesion. DS2100 is a developer for dissolving the portion of photo BCB unexposed to UV light. The spinner used for BCB coating is a WS-400 spin processor from Laurell Technologies Corporation. The temperature control, vacuum environment, and compressive force required for the bonding process was provided by a wafer bonder (AWB 04, AML). The RIE process was achieved using a Phantom II Reactive-ion Etching system.

Figure 16 illustrates the eight fabrication steps, which required three photo masks. The fabrication started with RCA1 cleaning of both the top and bottom wafers (Step 1). The RCA1 solution contained NH_4OH, H_2O_2, and H_2O with volume ratio of 1:4:20 and the solvent temperature was maintained at 70°C.

---

[2] © IOP Publishing Ltd. Reproduced with permission.
http://iopscience.iop.org/article/10.1088/0960-1317/26/11/115019/meta

Photo BCB was deposited on both the top and bottom wafers in step 2. Adhesive promoter AP3000 was first spin-coated on the wafer surface with a spin rate of 3000 RPM for 15 seconds. After baking the wafer at 120°C for 30 seconds, the photo BCB was then spin-coated with spin rate of 500 RPM for 10 seconds followed by 5000 RPM for 30 seconds. After soft baking at 60°C for 90 seconds, the wafers were ready for lithography. UV light with energy of 3 mJ/cm^2 was applied to the top wafer through photo mask 1 using a SUSS MA6 mask aligner under hard contact mode. Photo mask 1 was designed to expose the cavity features. The bottom wafer was directly exposed in its entirety to UV light using the same exposure energy with no photo mask applied. Post exposure bake at 50°C for 30 seconds was then applied to the wafers. There was no thickness change observed after UV exposure and after post exposure bake. The developer was drop cast on the top wafer for 2 minutes and the dissolved photo BCB was then spun-off the wafer under a spin rate of 500 RPM for 10 seconds followed by 2000 RPM for 30 seconds. After the top wafer with patterned cavities was blow-dried with nitrogen, both the top and bottom wafers were ready to be bonded.

In the wafer bonding step (step 4), the top and bottom wafers were first separately held by mechanical clamps in the vacuum chamber under a pressure of 0.05 mbar. The two wafers were then brought into contact under an applied compressive pressure of 0.4 MPa over the whole wafer area. The compressive pressure was controlled by controlling the distance between the clamps, which held the wafers in place. For any thickness change happened in the photo BCB film during heating process, the wafer bonder was able to automatically adjust the clamp position in order to maintain the same pressure level. The full curing process was then achieved by heating up the wafer pair to 150°C, maintained for 15 minutes and then heating up to 250°C, maintaining for one hour. The bonded pair was then allowed to cool below 150°C, while the compressive pressure was maintained.

The next step of membrane release (step 5), required the removal of the silicon substrate of the top wafer. Since the back side of the top wafer also had another layer of silicon nitride deposited during the LPCVD process, this layer of silicon nitride needed to be removed by an RIE process prior to the silicon etching process. The RIE process used a gas mixture of oxygen (O_2) and tetrafluoromethane (CF_4) with flow rates of 105 sccm and 10 sccm, respectively. The power was set to 100 W with chamber pressure of 80 mTorr and etching time of 12 minutes.

The silicon substrate of the top wafer was removed by wet etching with a 25% KOH at 70°C for 12 hours. In order to protect the bottom wafer from being etched, a layer of polydimethylsiloxane (PDMS, Sylgard 184 from Dow Corning) was drop casted on the back side of bottom wafer before immersing into KOH. Surface tension prevented the drop casted uncured PDMS from flowing over the edge of the wafer and on to the other side. The PDMS layer was then processed with degassing in a vacuum oven under room temperature for half an hour. Full curing of the PDMS was achieved by placing the wafer in an oven at 80°C for two hours. The PDMS layer was peeled off from the bottom silicon wafer after the silicon substrate of the top wafer was fully dissolved.

The last three steps were for the deposition of top and bottom electrodes. A thin layer of chromium (Cr) was applied to enhance the adhesion between aluminum (Al) and the silicon or silicon nitride surfaces. An Al electrode allowed easy wire bonding with Al wires and also acted as passivation layer to protect the Cr from oxidation. In step 6, top electrodes and bonding pads were deposited and patterned (photo mask 2) by lift-off technique with e-beam evaporation of 30 nm Cr and 55 nm Al consecutively. The silicon substrate was used as the bottom electrode and was exposed by a two-step RIE (step 7 using of photo mask 3) and then deposited with metal (30 nm Cr and 55 nm Al) (step 8). In the two-step RIE process, the nitride membrane layer was first etched through with settings as described in step 5. The BCB layer was then etched with the gas mixture of CF_4 and O_2 but with flow rates of 20 sccm and 80 sccm, respectively. The power was set to 100 W with chamber pressure of 50 mTorr and an etching time of 5 minutes. Once the aforementioned fabrication steps were finished, CMUTs were diced from the wafer and wire bonded with the supporting circuits for further characterizations.

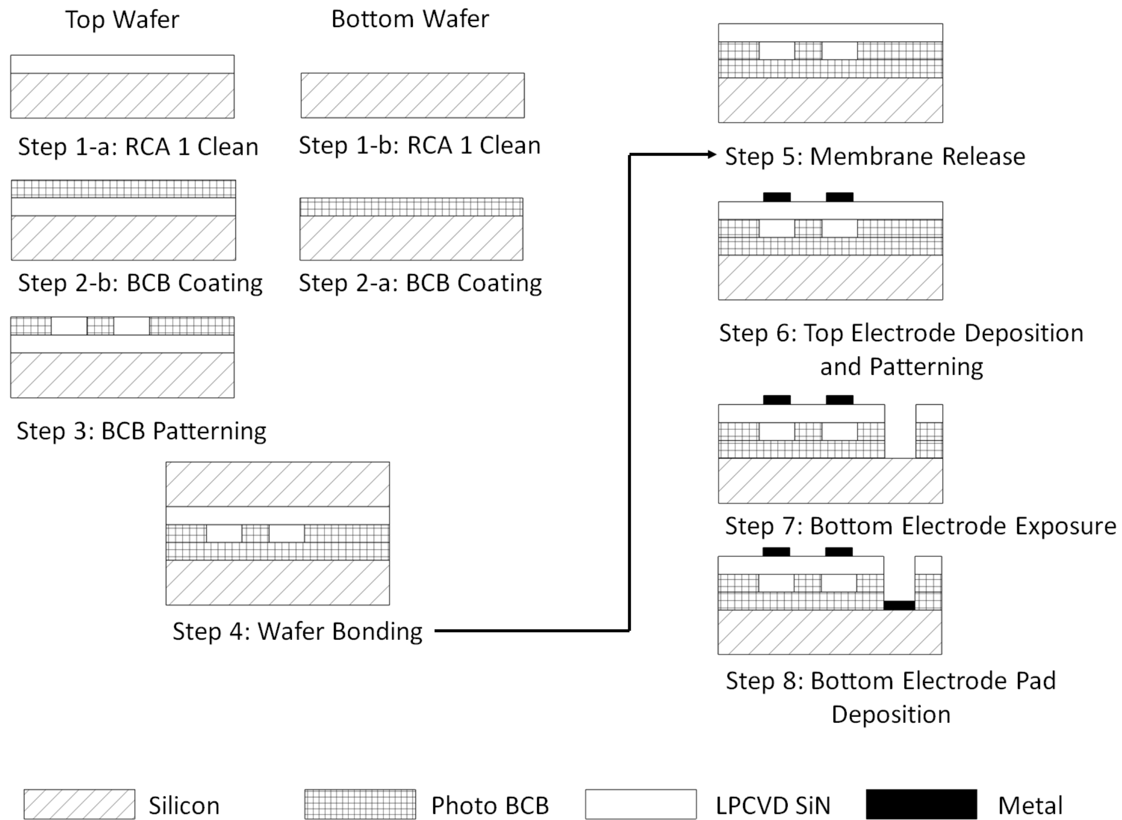

Figure 16: Fabrication process of the first-generation photo BCB CMUTs

4.2 Fabrication Issues

4.2.1 Bonding Strength and Structural Dimensions

According to application notes and previously reported works, the bonding strength of photo BCB on silicon and silicon nitride surface is about 40 to 60 J/m^2 [88, 89]. The reported adhesive wafer bonding in this paper was achieved by following the recommended temperature profile for photo BCB curing from Dow Chemical [87]. Therefore, the bonding strength was believed to be within the range of previous reported works. On the other hand, the fabricated CMUT displayed no de-bonding effects after more than 160 hours of operation, which could be considered as experimental evidence of strong bonding.

In order to inspect the effect on BCB structure from the bonding pressure, one of the CMUT cells was opened with focused ion beam (FIB) and the cross section of the cell structure was then inspected with SEM, as which is shown in Figure 17.

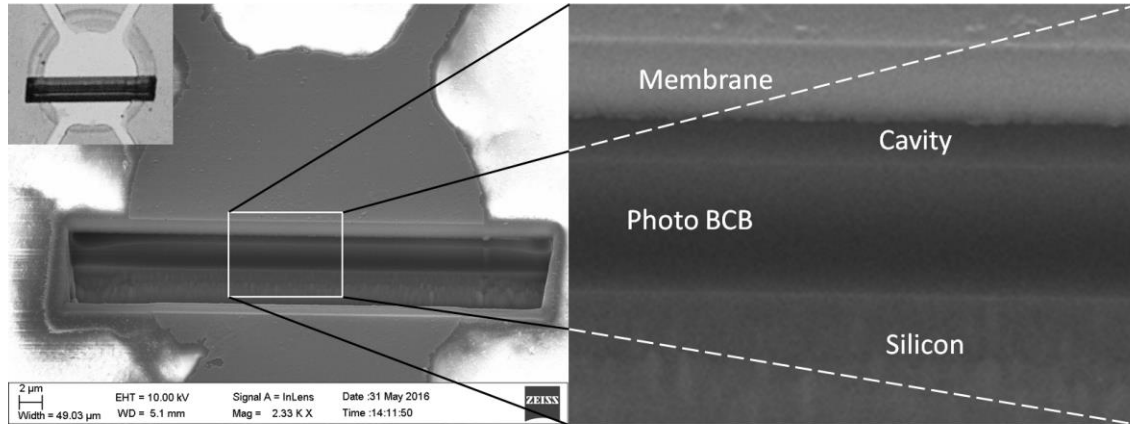

Figure 17: Cross sectional view of a CMUT cell through a window opened by FIB. The image was taken from slanting angle of 54°. The smaller image on the top left corner is taken by microscope, indicating the position of the opened window relative to the CMUT cell.

The BCB layers were found thicker in the center of the cavity region and thinner in the cavity edge. This structure was also repeatedly observed from the cross sections of CMUTs which were mechanically cracked across the cavities. Mechanically cracking the CMUTs were to verify that the shape of the observed structure was not induced by the FIB. Therefore, it can be concluded that BCB layers were deformed after the bonding process. The deformation was considered to be induced by the applied compressive force during the bonding process. During the wafer bonding step, compressive force was applied before increasing the temperature and the BCB at this moment is not stiff enough to maintain its shape. As shown in Figure 18, assume that there was no weight loss during the deformation process, the total BCB thickness decrease would induce expansion of the BCB layer on the top wafer (structural BCB) into the cavity area, which resulted in a decrease of cell diameter. On the other hand, the BCB layer on the bottom wafer (insulating BCB) was not able to expand along the wafer surface because it is a uniform layer with no cavities. As a result, the insulating BCB layer could be squeezed into the cavity region to make the insulating layer increase in thickness at the center of the cavities.

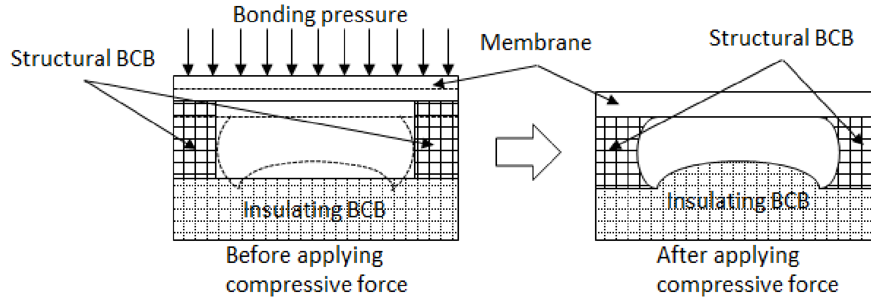

Figure 18: Deformation process of the BCB layers under compressive bonding force during wafer bonding step.

Table 6 summarizes the dimension information. The before-bonding dimensions were measured by a Dektak 8 stylus profilometer. The after-bonding dimensions are given based on the SEM image. And there was also a BCB layer thickness increase of about 323 nm in the insulating layer in the center region of the cavity, which occupied about 64% of the cavity area. And the thicknesses changes of BCB layers resulted in a final cavity depth of 323 nm.

Table 6: Structural dimensions of the fabricated one-element CMUT

	Before Bonding	After Bonding	
Membrane diameter (μm)	50	46	
Membrane thickness (nm)	600	600	
Cavity depth (nm)	700	323 (center)	646 (edge)
Insulating layer thickness (nm)	600	923 (center)	600 (edge)
Cell to cell distance (μm)	55		
Cell number per element	360		
Aperture size	1 mm by 0.95 mm		
Electrode diameter (μm)	33.5		
Electrode thickness	Cr 30 nm with 55 nm Al on top		

The deformation was not taken into account during the design process, but the resulting structure reduced the effective distance between the top and the bottom electrodes due to the increase of insulating thickness and the decrease of cavity depth. The decrease of effective electrode distance further increases the transducer capacitance and as a result, the receive sensitivity can be improved.

The deformation effect was not reported in either of the insulating and structural layers of the dry-etch BCB wafer bonding process [62]. This may be because the deformation was too small to be observable since the thickness of dry-etch BCB insulating layer was only 140 nm. Secondly, the structural layer of dry-etch BCB was patterned with an RIE process and the side

wall of the cavity was already curved, unlike the side wall of the photo BCB cavity which was straight before bonding.

4.2.2 Photo BCB and Dry-Etch BCB for Wafer Bonding

The initial and the major reason we proposed to use photo BCB for wafer bonding instead of dry-etch BCB was to simplify the cavity patterning process. Only the film coating parameters and the UV light exposure parameters need to be controlled to pattern the photo BCB. Furthermore, cavities are patterned directly through lithography process. Thus, the size variance among cells is controlled by the mask resolution. The resolution of the masks that were used in the reported fabrication process is ± 0.5 µm. In contrast, the dry-etch BCB requires an extra layer of photoresist as a masking layer for RIE patterning. Having fewer control parameters, the photo BCB fabrication process can be more repeatable and controllable. On the other hand, the photo BCB structures undergo deformation due to the applied compressive force.

Another advantage of photo BCB is its much shorter time duration for achieving wafer bonding. In order to present a clear comparison between the processing times, we derived temperature profiles, as shown in Figure 19, according to the process of using dry-etch BCB described by Bakhtazad et. al. [62], and the first generation fabrication process based on photo BCB.

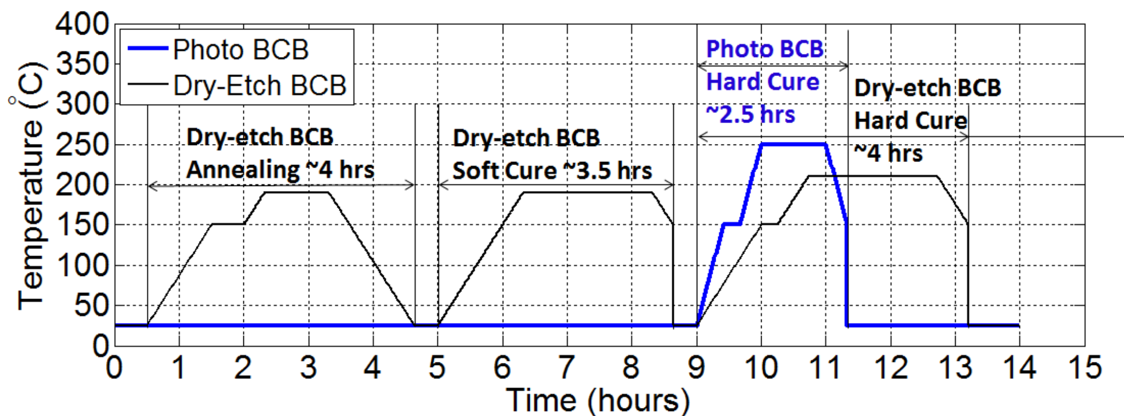

Figure 19: Temperature profiles of photo BCB and dry-etch BCB for wafer bonding. The profile of photo BCB showed better time efficiency than dry-etch BCB.

By comparing the temperature profiles, it is first found that the maximum required temperature for curing photo BCB is 250°C, which is 40°C higher than required for curing dry-etch BCB. However, the required maintaining time at maximum temperature of photo BCB is one hour, which is only half that required for processing dry-etch BCB. Secondly, according to the results from Bakhtazad et. al., if the soft cure process of dry-etch BCB is not performed before bonding, voids will appear at the bonding interface [62]. Voids that were found in the cavity areas would definitely affect device operation. In comparison, when using photo BCB and no-soft-cure step, voids only appeared in regions with no cavities, as shown Figure 20. The voids may have been induced by the solvent residuals evaporating from the photo BCB surface during curing. The solvent residuals can be developers or absorbed moistures from environment. The evaporated solvent can also diffuse into nearby cavities instead of getting trapped within the bonding interface, which would result in further voids. The phenomenon of gas diffusion into cavities was also reported in [90].

The voids around the cavities did not affect the remaining fabrication steps or the operation of the device. As a result, the soft cure was not included in the proposed photo BCB CMUT fabrication process. In summary, the total time toward achieving wafer bonding by using photo BCB is about 2.5 hours, which is only one fifth of the time required when using dry-etch BCB. Thus, the fabrication cost can be further reduced.

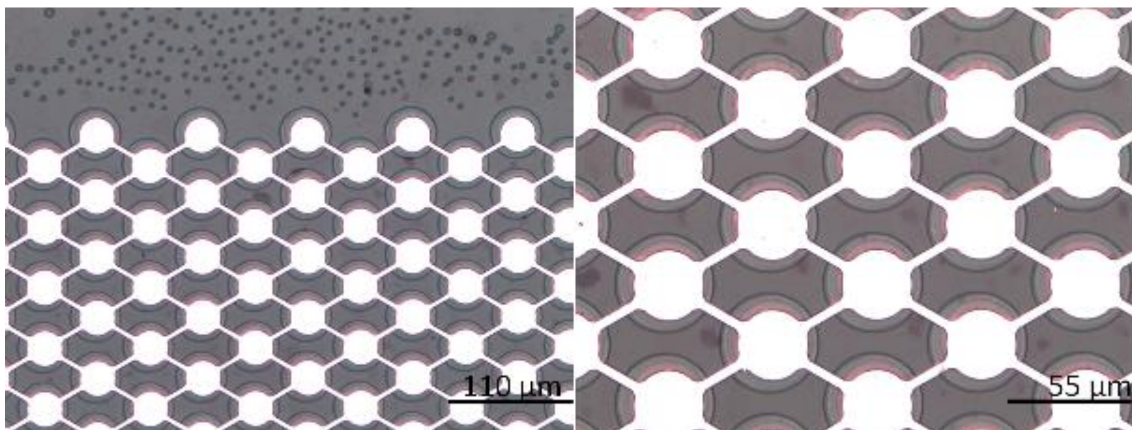

Figure 20: Microscopy images of the fabricated CMUT with no soft cure

4.3 Characterization

4.3.1 Pull-in Voltage and In-air Resonance Frequency

A Polytec OFV-5000 single point vibrometer was used to measure the vibration amplitude of the fabricated CMUT during operation. The CMUT was biased with a DC voltage supplied by a voltage source (Keithley 6487) and activated with continuous sinusoidal waves supplied by a signal generator, Tektronix AFG 3022B. The vibration amplitude of CMUT membrane varies with the applied bias voltage and the frequency of the AC signal.

The pull-in voltage was determined by increasing the bias voltage and monitoring the vibration amplitude. Pull-in occurred when the vibration amplitude dropped from around 70 nm to zero at a bias voltage of 345 V. Electrical breakdown of the insulating layer should be avoided during device operation. The device was biased up to 500 V (45% higher than the pull-in voltage) and showed no breakdown effect. Therefore, the device when operated below pull-in voltage is safe from breakdown.

The in-air resonance frequency of the CMUT at certain bias voltage can be found by sweeping the frequency of the AC signal. The membrane vibration amplitude reaches its maximum when the AC signal frequency is adjusted to the membrane resonance frequency.

By adjusting the frequency of the AC signal with an amplitude of 7.5 V and a step change of 10 kHz, the in-air resonance frequency was measured as 5.47 MHz with vibration amplitudes of about 70 nm under a bias voltage of 300 V. As shown in Figure 21, the resonance frequency was slightly reduced with increased bias voltage due to the spring softening effect [91]. At lower bias voltage, 50 V for example, the resonance frequency was 5.59 MHz, but with much smaller vibration amplitude of around 12 nm. The measured in-air resonance frequency is closed to the predicted value (~5.45 MHz).

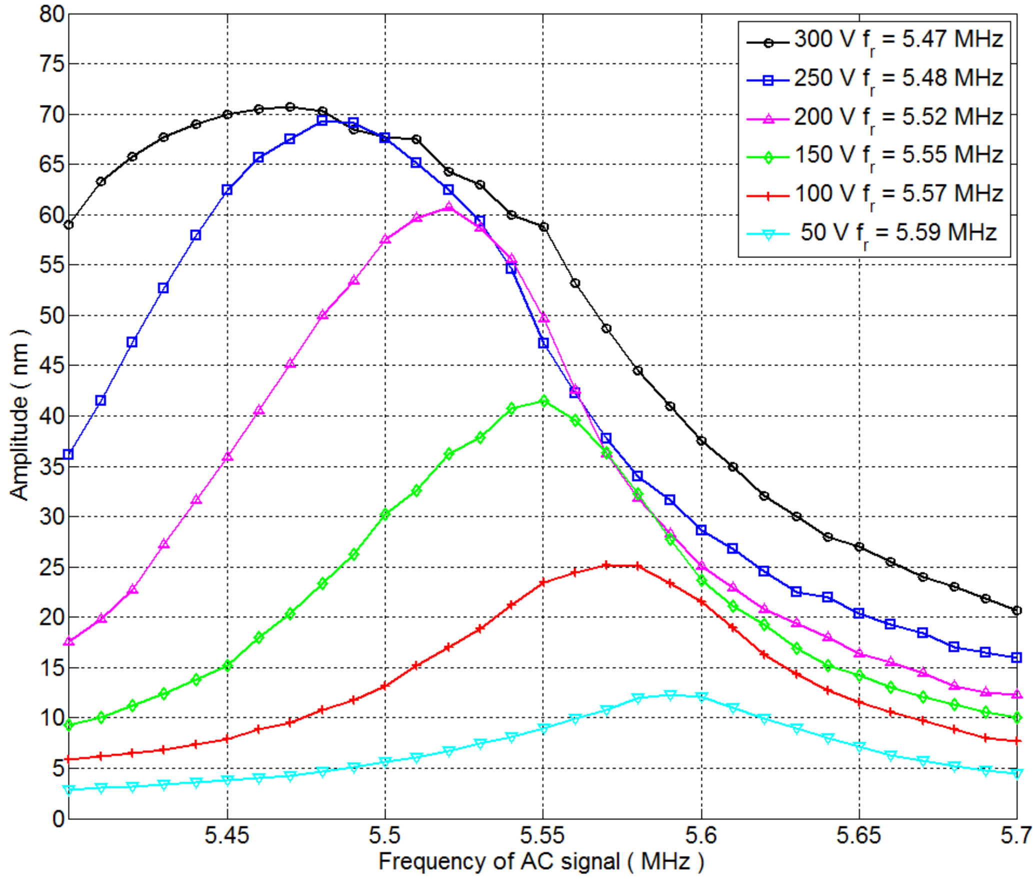

Figure 21: Resonance frequency measurement under bias voltages of 50 to 300 V by sweeping frequencies of AC signal with amplitude of 7.5 V

The vibrometer can only be focused on one single cell for resonant frequency measurement. In order to evaluate the average resonance effect of the entire CMUT element, network analyzer (Rohde & Schwarz ZNB 20) was used to measure the s-parameter of the CMUT. The measurement results of S_{11} were further converted to the impedance of the CMUT following Equation 1. The Z_{system} is the system impedance, which is usually assumed to be 50 Ω.

$$Z = Z_{system}\frac{S_{11}+1}{S_{11}-1} \qquad \text{Equation 1}$$

The magnitude and the real impedance are plotted in Figure 22. Consider the series resonance frequency is the local peak of real impedance, the series resonance frequencies under bias voltage of 200 V was found at 5.49 MHz with -0.03 MHz difference with vibrometer measurement results.

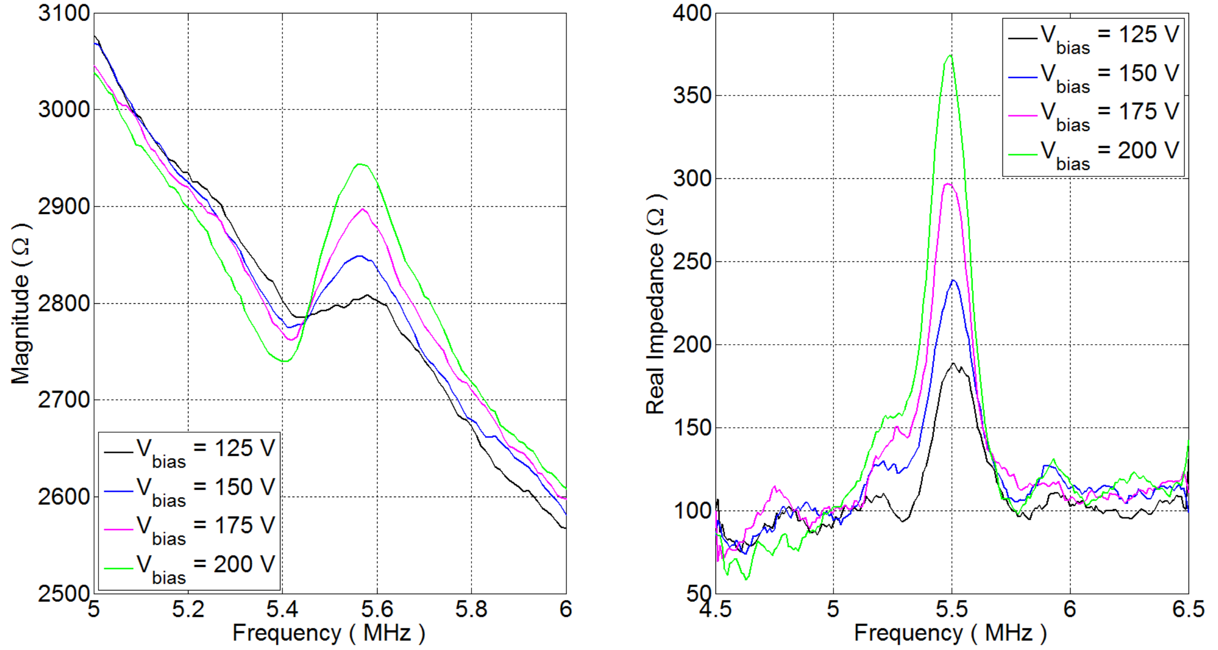

Figure 22: VNA measurement result under bias voltage of 125 V, 150 V, 175 V and 200 V. The impedance magnitude is plotted in logarithmic scale.

4.3.2 Acoustic Characterization

An acoustic characterization was carried out to demonstrate the ultrasound generation and receiving capabilities of the fabricated CMUTs. As illustrated in Figure 23, there were two CMUTs from the same wafer used for the acoustic characterization. One is a transmitting-CMUT (T-CMUT) for generating ultrasound signal. The other one is a receiving-CMUT (R-CMUT) for receiving the ultrasound signal. Both the T-CMUT and the R-CMUT were immersed in vegetable oil, which was purchased from a local retailer. According to [92, 93], the sound speed in the vegetable oil was estimated to be 1470 m/s, and the attenuation coefficient in the vegetable oil can be estimated by: $\alpha = Af^n$, while A = 7.83×10^{-12}, n = 1.84.

Both of the T-CMUT and R-CMUT were biased with 300 V. A pulser (Panametrics NDT 5073PR) was used to drive the T-CMUT for generating ultrasound signal. The signal from the pulser is presented in both time and frequency domain, as shown in Figure 24. An operational amplifier (OPA354, Texas Instruments) in a transimpedance configuration with a 25kΩ-gain was used to amplify the ultrasonic signal received by the R-CMUT.

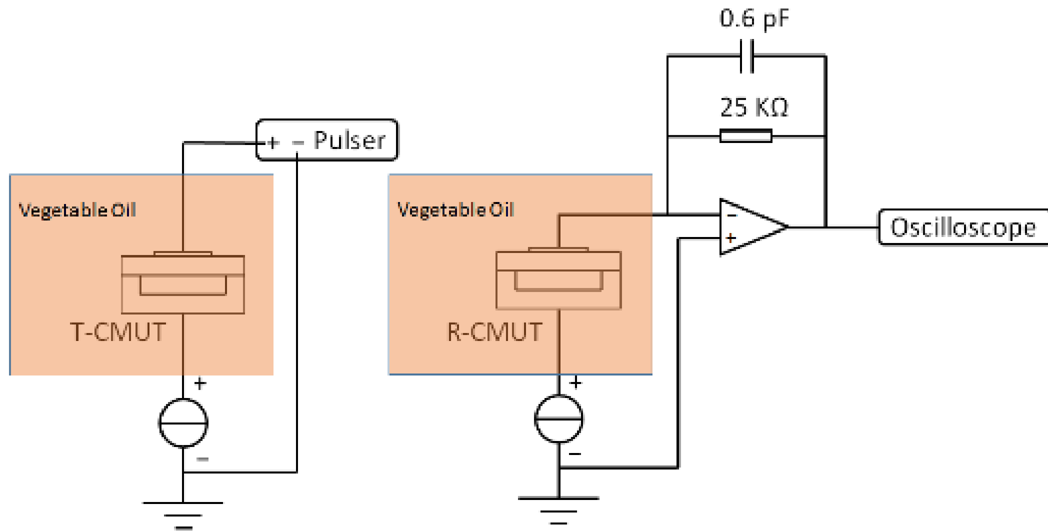

Figure 23: The setup of T-CMUT and R-CMUT

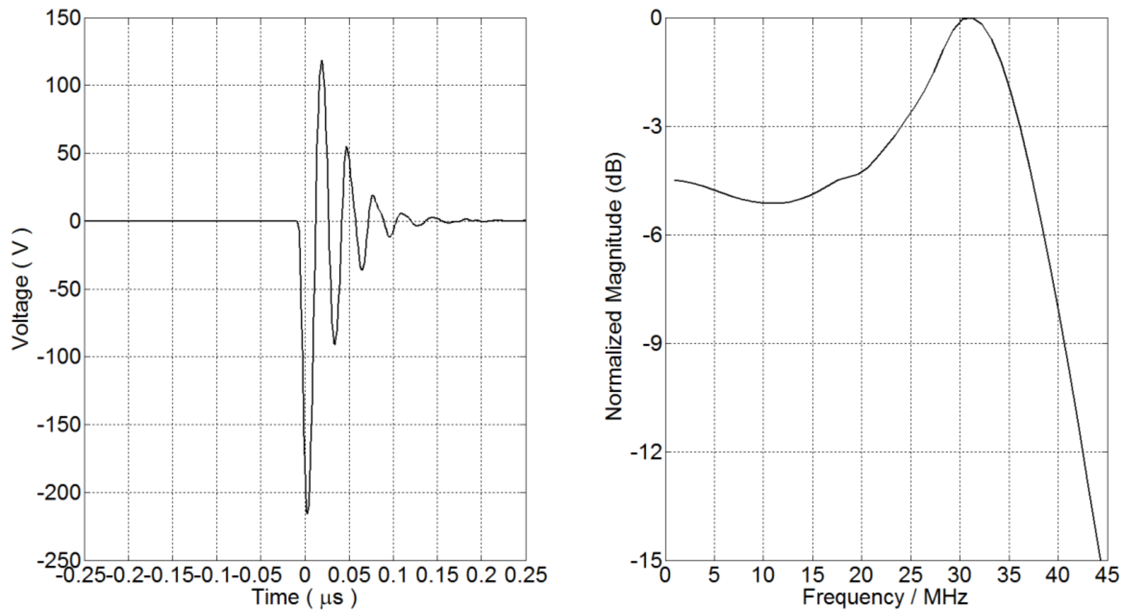

Figure 24: The signal that inputs into T-CMUT for ultrasound generation. The signal was presented in both time domain (left) and in frequency domain (right). The signal presents a relatively flat frequency band between 0 and 20 MHz, but a peak in amplitude appeared around 31 MHz.

The transmission capability of the CMUT was demonstrated by pitching ultrasound with the T-CMUT and receiving the signal by a hydrophone (Onda HGL-0200) with a 20 dB pre-amplifier (Onda AH-2010). The hydrophone tip was placed in the far field with distance of about 10 mm in front of the T-CMUT. The ultrasound signal captured by the hydrophone is presented in both time and frequency domain, in Figure 25. The center frequency is 3.1 MHz

and the -3dB fractional bandwidth is 106.3%. Based on the calibrated sensitivity data of the hydrophone (51.7 nV/Pa at 3.1 MHz), the acoustic pressure at the hydrophone tip is 79.28 kPa. Based on the estimated acoustic attenuation coefficient and beam spreading, the acoustic pressure exerted from the CMUT can be calculated to be 428.44 kPa [94]. This value is in the same order of magnitude of the one reported by Logan et. al. who also used LPCVD silicon nitride as membrane [95].

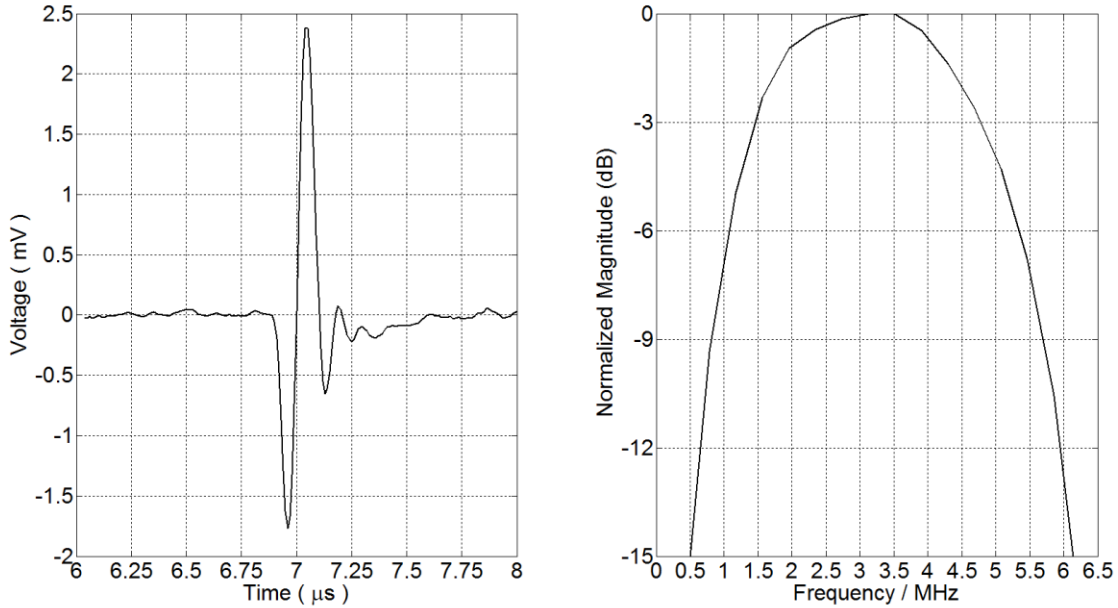

Figure 25: Output of the hydrophone in both time domain (left) and frequency domain (right). The center frequency is 3.1 MHz and the -3dB fractional bandwidth is 106.3%. The signal indicates an acoustic pressure of 79.28 kPa at the position of the hydrophone tip.

The capability to receive ultrasound was demonstrated by pitching an ultrasound signal with T-CMUT and catching the signal with R-CMUT. The two CMUTs, separated by about 10 mm, were placed facing each other. The output of the transimpedance amplifier in both time and frequency domains are given in Figure 26. It shows a center frequency of 3.0 MHz with a -6dB fractional bandwidth of 137.7%. Based on the acoustic pressure obtained by hydrophone test, the receive sensitivity is estimated to be 2.36 μV/Pa.

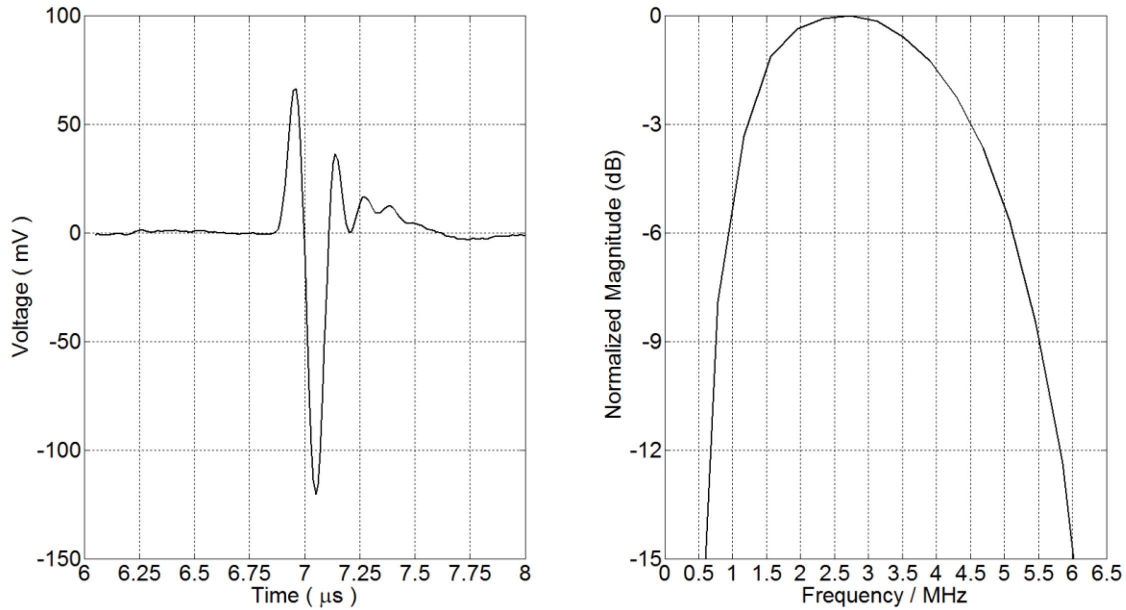

Figure 26: Receive test result showing output of the transimpedance amplifier in both time domain (left) and in frequency domain (right). The center frequency is 3.0MHz and the -6 dB fractional bandwidth is 137.7%. The signal indicates a receive sensitivity of 2.36 µV/Pa.

It was found that the measured center frequencies in both hydrophone test and receive test were around 3 MHz, which was higher than the estimated immersion resonance frequency (~1.8 MHz) based on the model given in [96]. It is hypothesized that the shift in center frequency was caused by the membrane touching the bottom of the cavity during vibration. According to the setup shown in Figure 23, the potential at the bottom electrode was 300 V due to the applied bias voltage. The strong pulse applied to the top electrode could then make the potential difference between two electrodes be more than 500 V.

4.4 Summary

The first generation BCB CMUT proved the feasibility of adhesive wafer bonding based CMUT fabrication process using non-polished-LPCVD silicon nitride as membrane. The fabrication process showed most simplified process with low wafer cost and lowest process temperature when compare with direct bonded CMUT and surface micromachined CMUTs. The comparisons are detailed in Table 7.

Table 7: Fabrication process comparison

	Surface micromachining	Direct bonding		Adhesive bonding (Photo BCB)
Reference	[6]	[6]	[5]	
Bonding wafer pair	N/A	SOI Si	LPCVD SiN LPCVD SiN	LPCVD SiN Si
Bonding restrictions	N/A	N/A	CMP required	Photo BCB as adhesive
Requirement to surface quality	N/A	Restrict	Restrict	Low (highest bond yield)
# of Masks	5 (most)	3	3	3 (least)
# of Wet etch steps	3	4 (most)	1	1 (least)
# of Dry etch patterning steps	4 (most)	2	2	1 (least)
# of high temp. steps (>500°C, involving substrate wafer)	5 (most)	3	1	0 (least)
Max. process temp. (processes with substrate wafer)	785°C	1100°C (highest)	1000°C	250°C (lowest, CMOS compatible)
Process complexity	High	Low	Low	Lowest
Wafer cost	Low	High	Low	Low
CMOS compatibility	Poor	Poor	Poor	Good

Further improvements are still required in following aspects:

- Reduce bias voltage during operation
- Minimize adhesive film deformation for better performance estimation

Detailed analysis regarding to these two aspects will be given in the next chapter.

Chapter 5 Fabrication Process Optimization

The first-generation CMUTs resulting from this work required high bias voltage for operation and displayed adhesive structure deformation. The second iteration of process development was performed to solve these issues. In this chapter, possible reasons related to high bias voltage and structure deformation are discussed. This is followed by detailed descriptions about process modifications. Lastly, based on the characterization results of the CMUTs produced in the second iteration, improvements on device performance are demonstrated.

5.1 Problem Analysis and Process Modification

High Operation Voltage

As illustrated in Figure 27, bias voltage was applied to the top and bottom electrodes of the CMUT through cables, aluminum bonding wires and a short path in the bottom silicon wafer. The resistance of the cables, copper pad, aluminum wires and metals (electrode pads) were proved to be small as far as enabling beeping when using multimeter for a shorting test. It was deemed likely that the RCA1 processing performed to remove the contaminants from the bottom silicon wafer strongly oxidized the surface of silicon forming a layer of oxide. As a result, there could have been an electrically insulating layer between the bottom electrode pad and the silicon substrate, which increased the series resistance. The real potential difference between top and bottom electrodes was likely smaller than the applied DC voltage. According to previous fabrication experience, a 3-second 10%-HF dip would be enough to remove the oxide layer of silicon, this was added to the modified process.

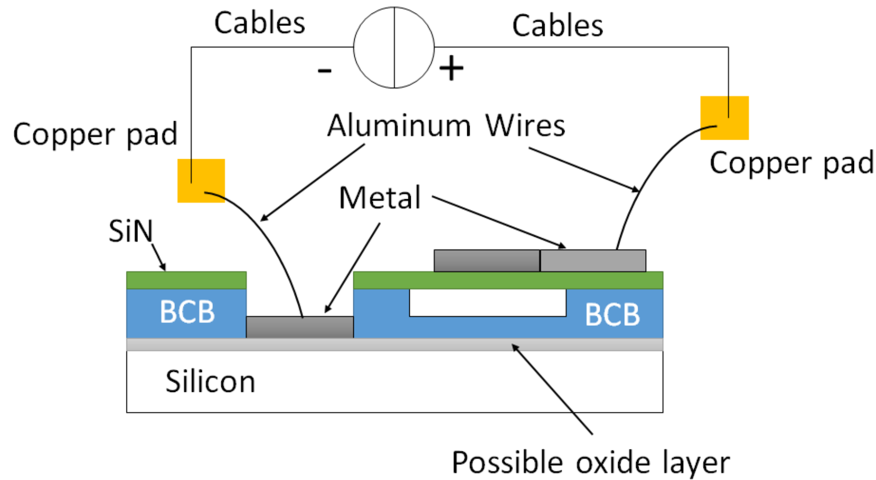

Figure 27: illustration of the paths for applying DC bias.

Adhesive Layer Deformation

The BCB layer deformation introduced difficulties in structural parameter control. According to the dry-etch BCB wafer bonding process [62], there was no obvious deformation reported when using dry-etch BCB after bonding. The soft curing process was one of the major differences between processes using dry-etch BCB and those using photo BCB. It was previously thought that soft cure of dry-etch BCB before the bonding step could remove voids at the bonding interface. However, we believed it might also help in increasing the stiffness of the adhesive film and enable better maintenance on structure shape. Thus, the soft cure process could be a solution to solving the problem of BCB deformation.

Process Modification

Two processes were added to the previously described fabrication process: soft curing of BCB film before wafer bonding and a 3-second HF dip, which is illustrated in Figure 28.

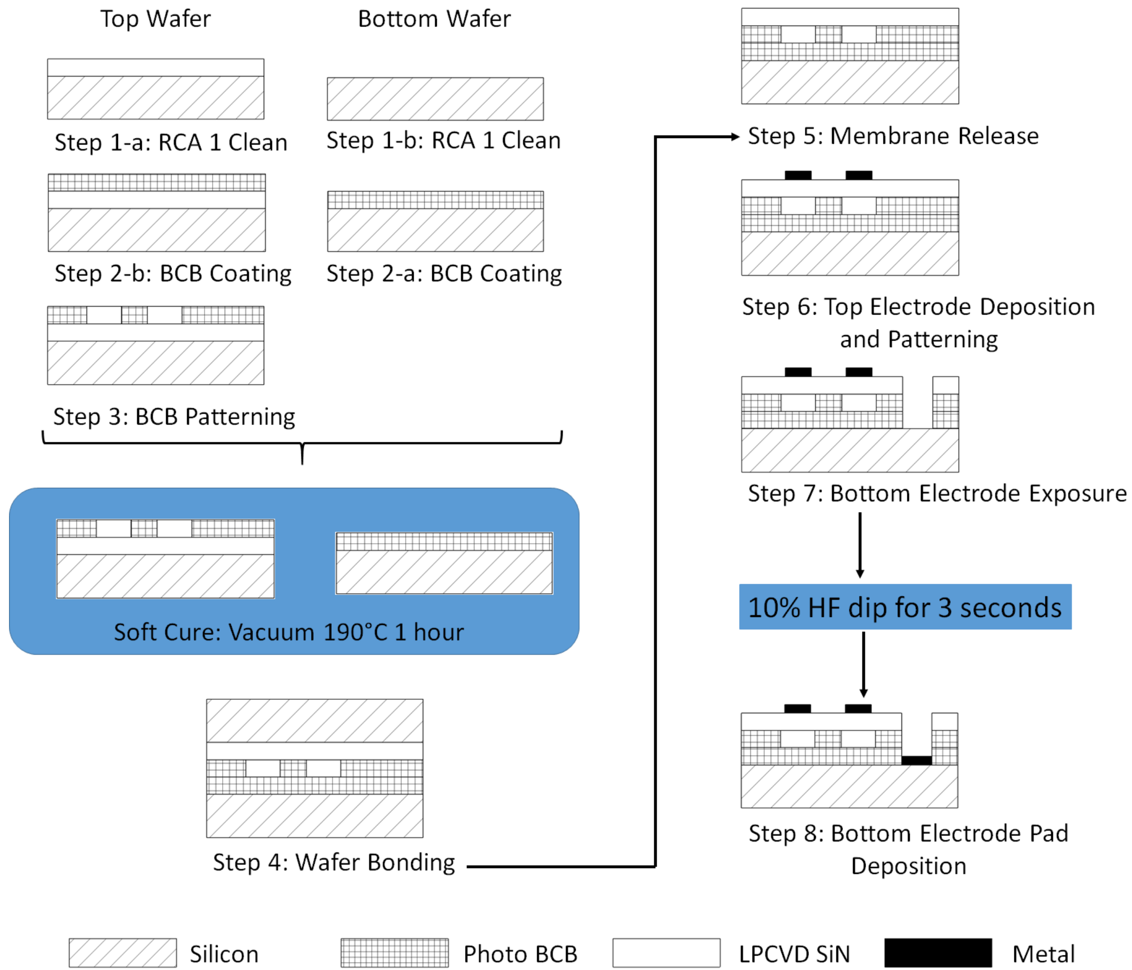

Figure 28: Modified fabrication flow. The newly added annealing process and HF dip step are highlighted with color blue.

The soft curing was done in a vacuum oven. After BCB coating and patterning on both bottom and top wafers, they were placed face-up in the vacuum oven at room temperature. A nitrogen-charge-vacuum process was thrice applied to remove oxygen. The wafers were then heated up to 190°C and maintaining for an hour followed by a cooling down process in vacuum.

Array Design and Electrode Size Decreasing

The first generation CMUT had only one element with 360 cells. The output power for immersion characterization was too small to measure. This was also one of the reasons that high bias voltage was required for operation and to obtain measurable signals. Therefore, masks were redesigned in order to produce CMUTs with increased cell number per element

with 1-D array layout. There were also one-element CMUTs designed and located at the edge of the wafer. Measurement results of these one-element CMUTs were used to evaluate the performance uniformity across the wafer. Detailed design parameters can be found in Table 8.

Table 8: Photo mask design parameters

	One-element CMUT	16-element CMUT (1-D Array)
Cell diameter (μm)	50	
Cell to cell distance (μm)	55	
Cell number per element (vertical × horizontal)	55 × 64 = 3520	110 × 8 = 880
Element number	1	16
Element size (vertical × horizontal, μm)	3050.8 × 3047.5	6072.5 × 383.4
Pitch (μm)	n/a	400

5.2 Device Characterization

5.2.1 Structure Dimensions

The deposition of silicon nitride on silicon wafer was outsourced. The thickness of silicon nitride layer was supposed to be 600 nm as stated in our specification of LPCVD service. However, in the interest of good practice, the thickness distribution over the entire wafer was inspected in order to have a better understanding of the membrane layer. Two of the obtained wafers were characterized with ellipsometry for a thickness measurement and the results are given in Figure 29. The two measured wafers have average silicon nitride thicknesses of 605.67 nm and 605.31 nm and standard deviations of 9.72 nm and 15.29 nm, respectively. The difference of average thicknesses between two wafers is less than 0.06%.

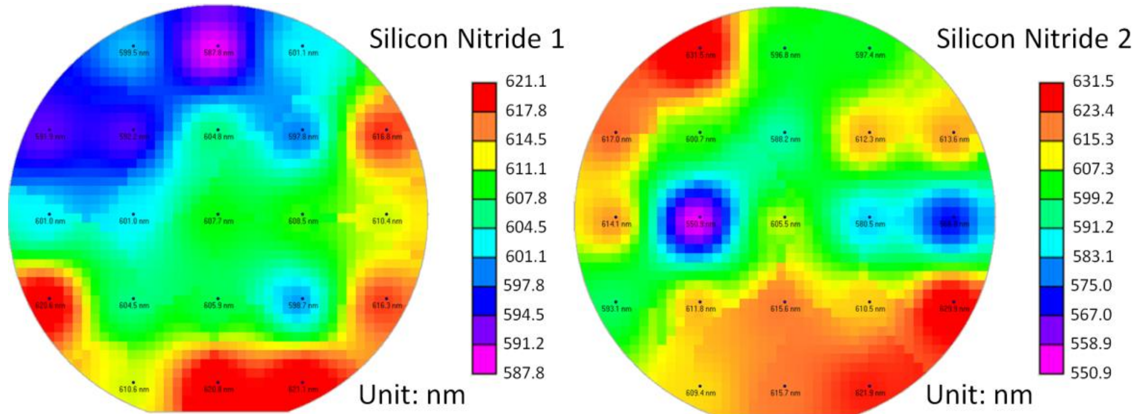

Figure 29: Thickness measurement of two of the purchased silicon nitride wafers.

The cavity depths before and after the soft cure process were measured with a profilometer. Horizontal dimensions of fabricated CMUT including cell diameter, electrode diameter and electrode trace width were measured based on microscopy images, as shown in Figure 30. Cell to cell distance should be equivalent to the one of photomask. Thus, the other dimensions of interest can be calculated by obtaining their ratios to the cell to cell distance in the image. In order to obtain vertical dimensions in side the cells, the cross sections of CMUT cells were inspected using FIB, as shown in Figure 31. The structure dimensions are summarized and compared in Table 9. It was found that the soft cure process induced a BCB film thickness decrease of about 100 nm. Another 214 nm decrease in film thickness also happened after the bonding process. However, the deformation of the bottom BCB layer was not observed.

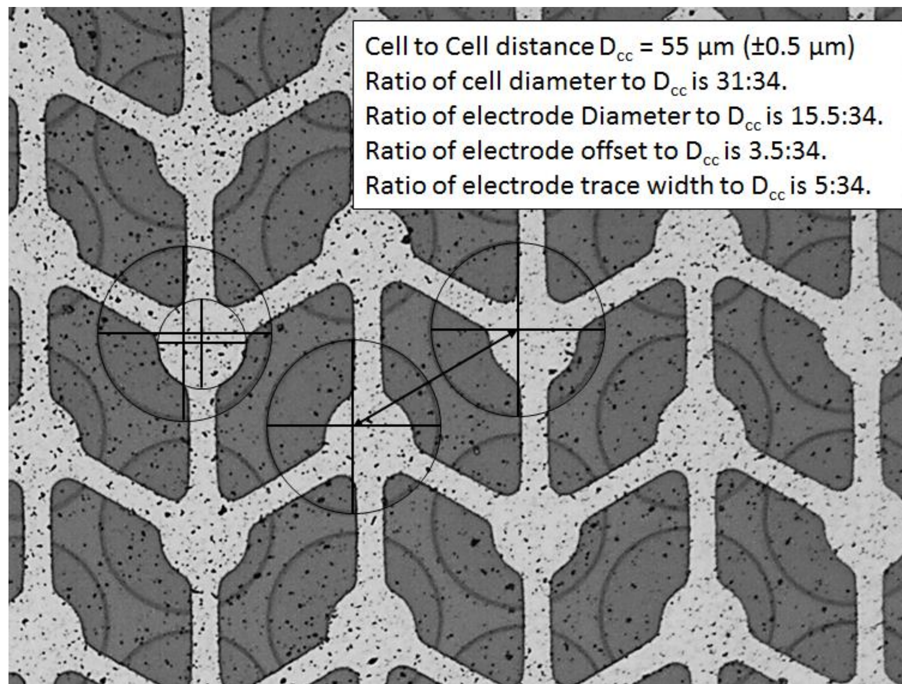

Figure 30: Microscopy image of 16-element CMUT. Dimensions were calculated based on the cell to cell distance and the ratio of interested dimensions to the cell to cell distance.

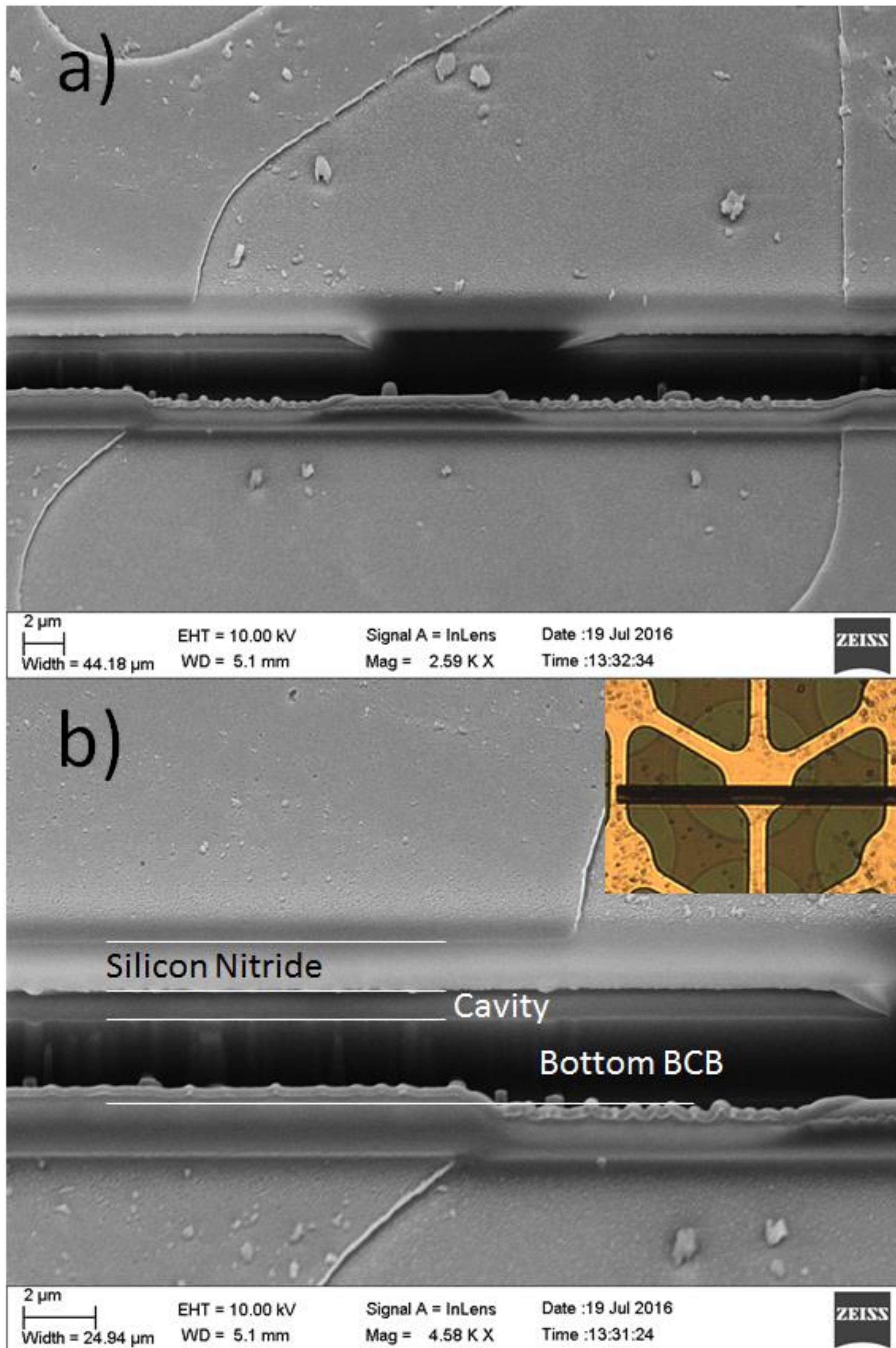

Figure 31: Cross section view of CMUT cell through a window opened by FIB and the image was taken from slanting angle of 54°. The BCB deformation effect was not found through the images. The microscopy image on the top right corner of image b) shows the position of the cutting window.

Table 9: Structural dimensions of the CMUT fabricated with improved process

Membrane diameter (μm)	50
Membrane thickness (nm)	605
Cavity depth (nm)	378
Insulating layer thickness (nm)	1059
Cell to cell distance (μm)	55
Electrode diameter (μm)	25
Electrode thickness (nm)	Cr 30 nm with 65 nm Al on top

5.2.2 In-air Characterization

Vibrometer Test

In-air resonance frequencies were firstly measured using the vibrometer. Figure 32 shows the vibration amplitude versus frequency when measuring a cell in one of the elements, while Figure 33 presents the resonance frequencies of each elements in the array. The average resonance frequencies and standard deviations under different bias voltages are given in Table 10.

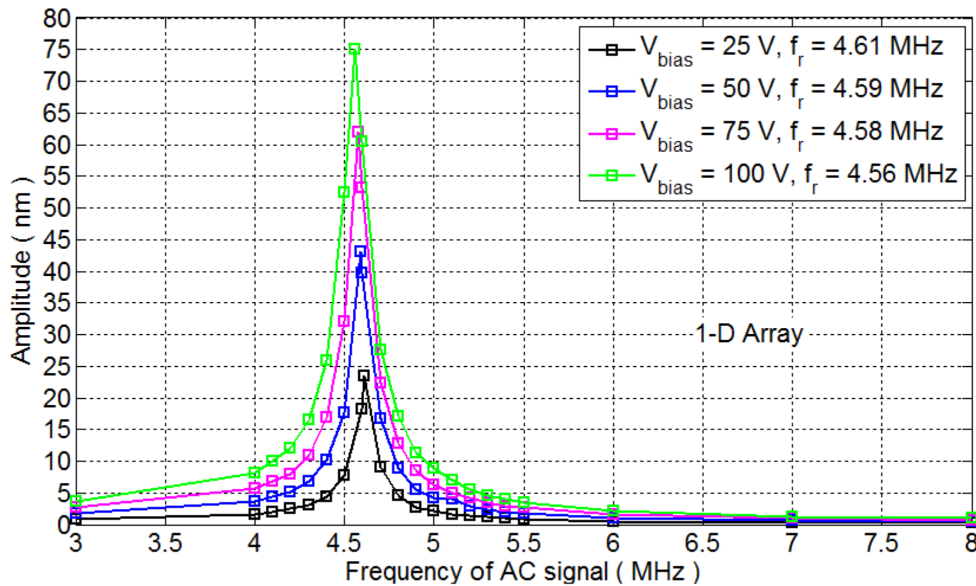

Figure 32: Resonance frequency of one of the element in 1-D array under bias voltages of 25 to 100 V by sweeping frequencies of AC signal with amplitude of 2.5 V

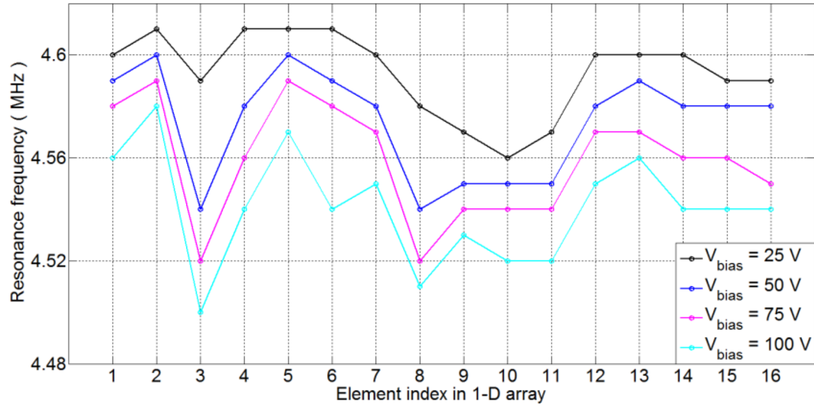

Figure 33: Resonance frequencies of each element in 1-D array under bias voltages of 25 to 100 V with AC signal amplitude of 2.5 V

Table 10: Statistical analysis of resonance frequency measurement results for 1-D array CMUT

	25 V	50 V	75 V	100 V
Average Resonance Frequency (MHz)	4.59	4.57	4.56	4.54
Standard Deviation (MHz)	0.0158	0.0206	0.0222	0.0214

The resonance frequency of single-element CMUTs at the edge of the wafer was also inspected with vibrometer. The measurement results are given in Figure 34. Being compared with the average resonance frequency of the 1-D CMUT array, single-element CMUT presented 0.09 MHz increase in resonance frequency.

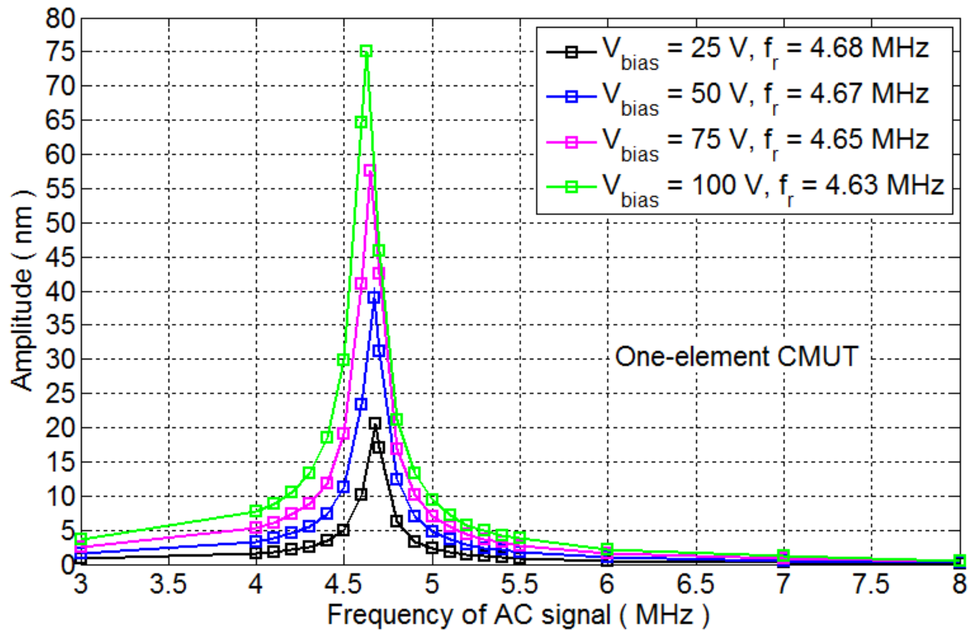

Figure 34: Resonance frequency of one of the one-element CMUT under bias voltages of 25 to 100 V by sweeping frequencies of AC signal with amplitude of 2.5 V

Network Analyzer Test

The impedance of one of the elements (#1 in Figure 33) in 1-D array CMUT was obtained by converting from the s-parameter measurement results using VNA. The magnitude and the real impedance are plotted in Figure 35. Considering the series resonance frequency as the local peak of real impedance, the series resonance frequencies under bias voltage of 100 V was found at 4.56 MHz, which shows accordance with vibrometer measurement results.

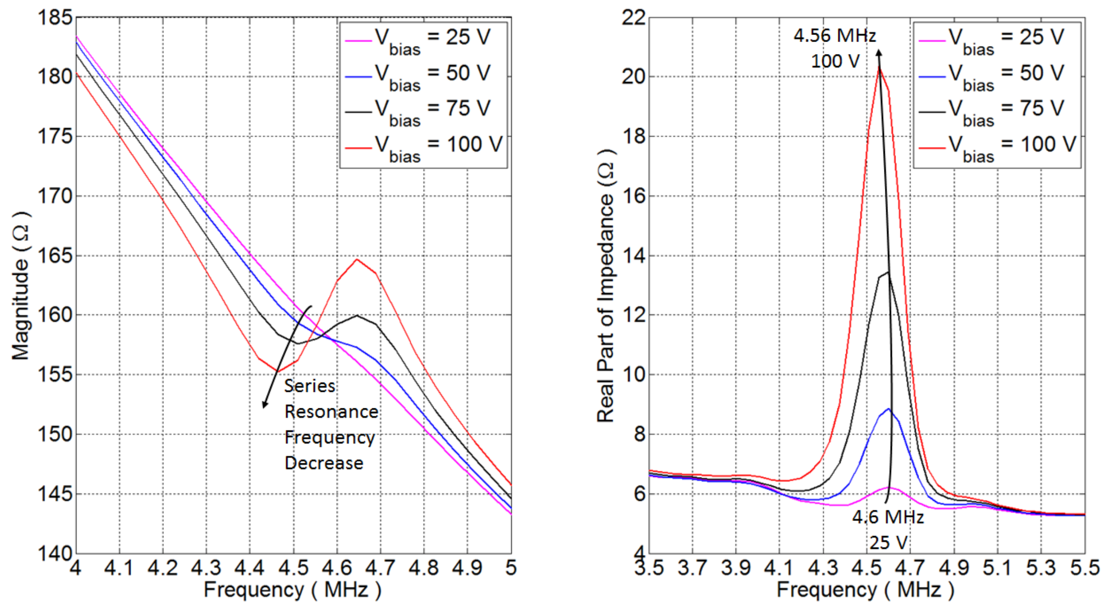

Figure 35: VNA measurement result under bias voltage of 25 V, 50 V, 75 V and 100 V.

A collapse phenomenon was also found during network analyzer measurement. As shown in Figure 36, when bias voltage was increased to round 145 V, the amplitude of the s-parameter clearly showed a peak at higher frequency around 8.4 MHz when bias voltage was increased to more than 145 V. At the same time, the peak indicating fundamental resonance at around 4.6 MHz still exist.

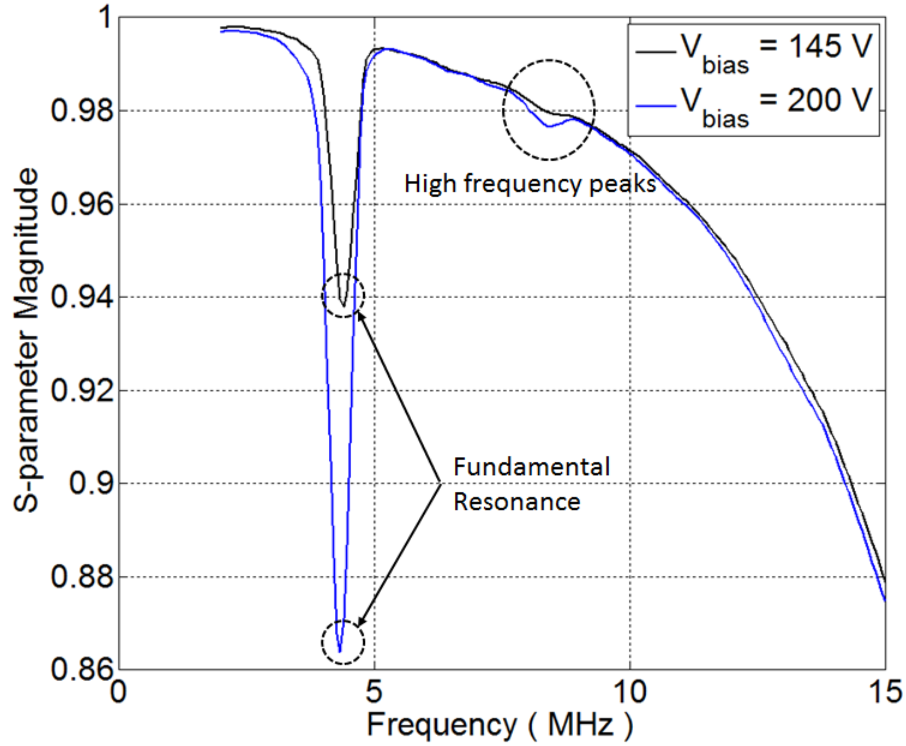

Figure 36: Network analyzer measurement results at bias voltages of 145 V and 200 V, respectively. High frequency peaks appeared gradually starting from at 145 V bias and the peaks became more obvious with the increased bias voltage.

5.2.3 Immersion Characterization

Experimental Setup and Measurement Results

The immersion resonance frequency was measured by pitching ultrasounds using a PZT transducer and receiving the signal with CMUT under receive mode (setup for R-CMUT in Figure 23). The pitched ultrasonic signal was first characterized with a hydrophone, which was placed in front of the PZT transducer at a distance of around 5.3 cm. The obtained hydrophone signal is given in Figure 37 and analyzed in frequency domain.

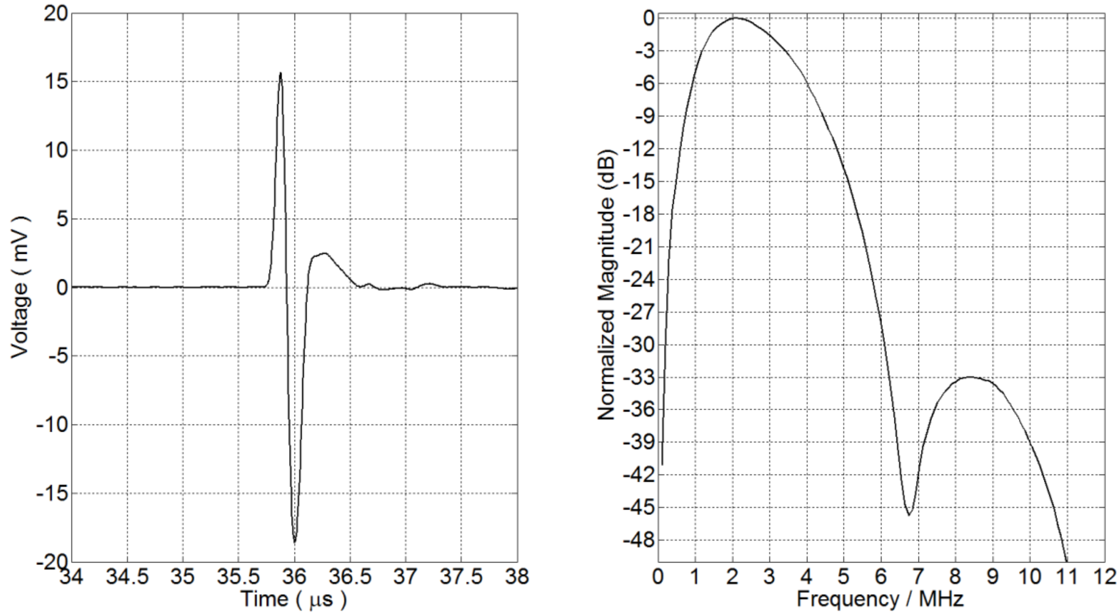

Figure 37: The ultrasound signal pulsed by PZT transducer for ultrasound generation. The signal was presented in both time domain (left) and in frequency domain (right). The signal presents a peak frequency at 2.05 MHz. The -3 dB band is from 1.19 to 3.42 MHz with center frequency of 2.31 MHz. The peak to peak voltage is 34.25 mV indicating a sound pressure of 639 kPa at the hydrophone tip.

The signal from the PZT transducer presents a peak frequency at 2.05 MHz. The -3dB band is from 1.19 to 3.42 MHz with center frequency of 2.31 MHz. According to the calibration data of the hydrophone (sensitivity of 53.6 nV/Pa at 2.3 MHz), The peak to peak voltage is 34.25 mV indicating a sound pressure of 639 kPa at the hydrophone tip. It is expected that when using R-CMUT to replace the hydrophone at the same position, the peak frequency can be shifted toward the immersion resonance frequency of the CMUT. During the measurement, CMUT were biased at 100 V in order to obtain a clear signal before the membrane was pulled-in. Measurement result and the frequency domain analysis are given in Figure 38. The 0-dB-peaks in frequency domain all appeared at 1.27 MHz with -3 dB band from 0.64 MHz to 2.07 MHz. The peak to peak voltage of the receive signal was 330 mV under 100 V bias. According to the estimated sound pressure at CMUT surface (639 kPa) based on the hydrophone data in Figure 37, the sensitivity of the R-CMUT was 516 nV/Pa, which was about 8.9 to 10.1 times (equivalent to about 19 to 20 dB) than that of hydrophone in the -3 dB band. As a result, the peak-frequency-components of PZT signal can be overcome by the resonance components of CMUTs. In this regard, the 0-dB-peaks in Figure 38 reflect the immersion resonance frequencies of CMUT under different bias voltage.

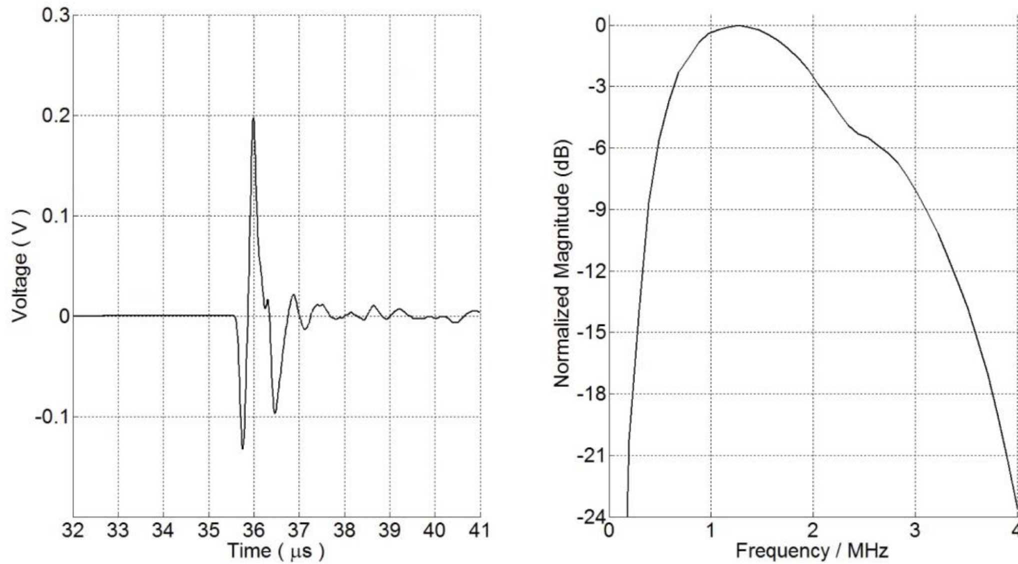

Figure 38: Use CMUT in receive mode setup in transimpedance configuration with a 25kΩ-gain to receive the ultrasonic signal from the PZT transducer. The CMUT was biased at 100 V showing 0-dB-peaks in frequency domain at 1.27 MHz.

5.2.4 Discussion in Collapse Voltage

The easiest way of measuring collapse voltage is to bias the CMUTs without applying any AC signal. By increasing the DC bias and observing cells under microscope, collapse voltage can be obtained at the moment when observe a sudden color change of the membrane. This color change is induced by the contact of membrane with the bottom insulating layer. However, it is not able to achieve such a measurement with the optimized first generation CMUTs. Therefore, indirect measurements were performed. As described in the section 5.2.2, collapse-effect was found at 145-V-bias in the network analyzer measurement. However, the network analyzer measurement result is different from the theoretical calculation based on the model given in the Appendix. Based on the structure dimensions given in Table 9, the collapse voltage was calculated as 110 V as illustrated in Figure 39. The maximum plate deflection under bias voltage from 1 V to 110 V was then calculated as plotted in Figure 40. The membrane touches the insulating layer at 107 V before pull-in. Considering that BCB coating is not very uniform, real voltage values could be more or less than the calculated ones. As a result, the extra peak of the S-parameter magnitude starting at 145-V-bias, which is higher than the calculated values, may indicate the difference of photo BCB thickness between the measured transducer and the value used in calculation.

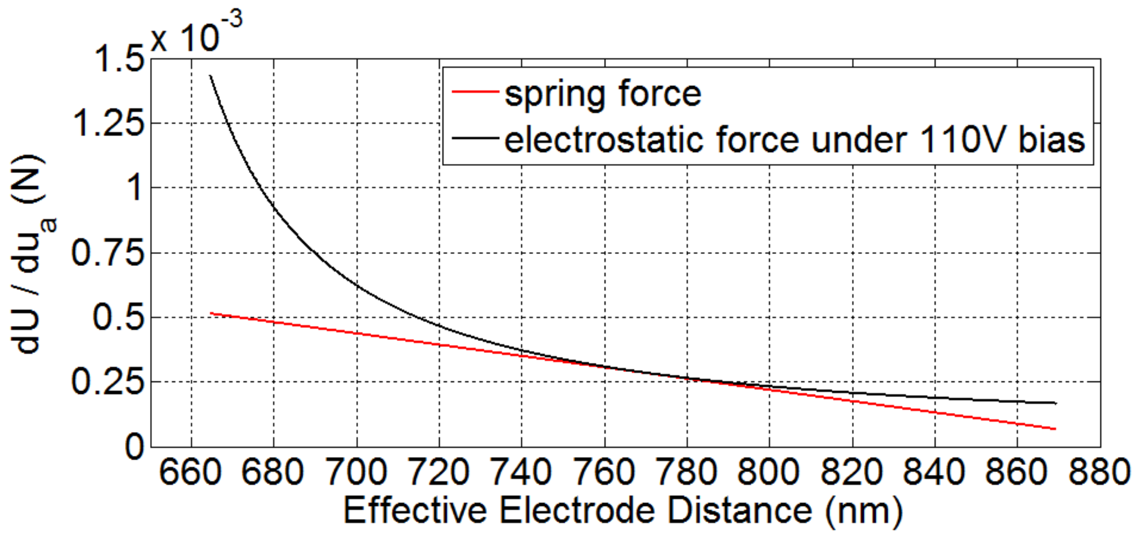

Figure 39: Pull-in voltage calculation based on structure dimensions.

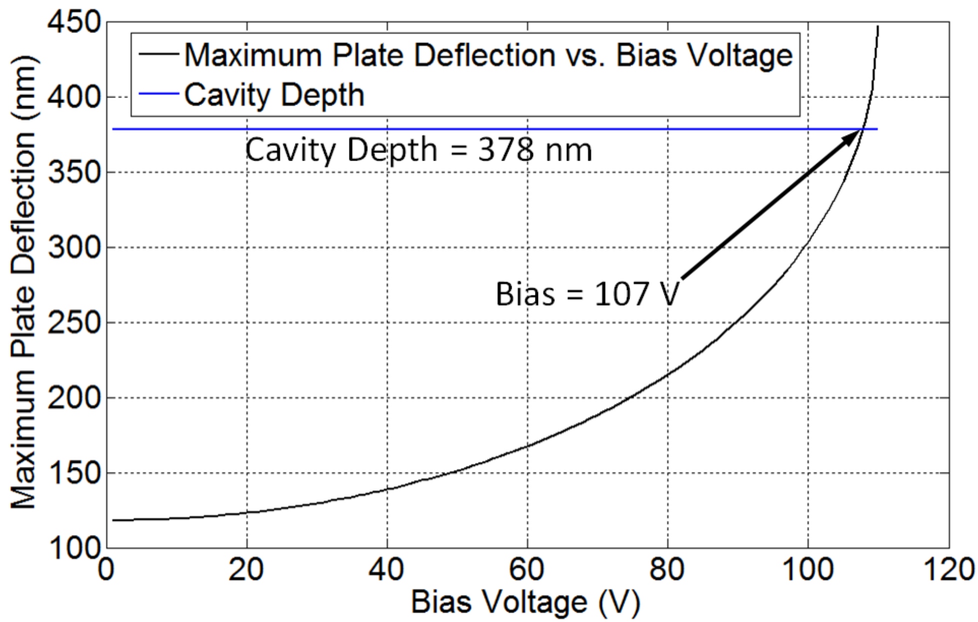

Figure 40: Theoretical calculation results: Maximum plate deflection under bias voltage from 1 V to the calculated pull-in voltage.

5.3 Summary

In this chapter, two improvements were made to the first generation CMUT fabrication process. The soft curing step solved the BCB deformation issue. There was no deformation observed through cross-section inspection using FIB technique. The membrane diameter showed no change after bonding and remained the same as the dimension designed on the photo mask. Secondly, the oxide removal by 3-second HF dip greatly decreased the required

bias voltage for CMUT operation. In order to obtain a vibration amplitude of 75 nm in vibrometer test, the bias voltage decreased from more than 300 V to 100 V and the amplitude of the applied AC signal also decreased from 7.5 V to 2.5 V.

Furthermore, the in-air resonance frequency was found at 4.56 MHz under 100 V bias voltage and the immersion resonance frequency was estimated at 1.27 MHz.

Lastly, it was also found that the membrane could touch the bottom of cavity before pull-in, which make the collapse voltage be difficult to inspect. Strict thickness control and structure inspection need to be performed in future for collapse-mode operation characterization. However, this was not easy to achieve as the cavity depth and the insulating layer thickness are controlled by spinning rate during coating. The achieved coating thicknesses are almost the minimum achievable thicknesses. As a result, further improvements in structure design and fabrication process are still needed in controlling the cavity depth and the insulating layer thickness. Also, the presented fabrication process appeared good feasibility for one element and 1-D CMUT array fabrication. When 2-D CMUT arrays are needed, top and bottom wafers need to be aligned during wafer bonding steps, which is difficult and decrease the process feasibility. The third iteration of process development was carried out.

Chapter 6 Second-Generation Adhesive Wafer Bonded CMUT

The first-generation process and its improved version controlled the cavity depth and the insulating layer thickness by controlling the spin rate when coating BCB adhesive. The maximum spin rate available in the spinner used for fabrication is 7000 RPM. There was no significant decrease in the coating thickness when the spin rate is higher than 5000 RPM, while the thickness uniformity decreased. The currently achieved thicknesses of insulating layer and cavity depth are 956 nm and 336 nm, respectively, under 5000 RPM spin rate are the fabrication limit of the previously described fabrication method.

Besides limitation in thickness control, the fabrication of 2-D CMUT array is not easy due to the need for wafer alignment in the wafer bonding step. In order to fabricate 2-D array, bottom electrodes need to be patterned on the bottom wafer before the wafer bonding step, while cavities are patterned on the top wafer. In order to align cavities with bottom electrodes, wafer pairs must be aligned before contacting with each other. This alignment requirement increases the difficulty of wafer bonding.

In order to break the thickness limitation and simplify the fabrication difficulties for making 2-D CMUT array, the second generation BCB CMUT was designed based on the photo mask design detailed in Table 8. The fabrication process will firstly be described in this chapter. Structure inspection and device characterization both in air and immersion will be given afterward. At the end of the chapter, the limitations and problems of the process will be discussed.

6.1 Fabrication Process

The detailed processing parameters and procedures of BCB coating and patterning, wafer bonding, top electrode deposition and patterning, and bottom electrode pad for wire bonding were not changed in the second-generation process. As illustrated in Figure 41, enhancement was made when preparing bottom wafer for bonding and cavities were patterned on the bottom wafer instead of the top wafer.

After RCA 1 cleaning of the silicon wafer followed with 10% HF dip for 3 seconds (Step 1, bottom wafer), a layer of Cr with thickness of 305 nm was sputtered (step 2). This metal layer was then patterned using photomask 1 (the mask with patterns of cavities) as step 3 with photoresist and wet etching. The resulting chromium circular pads were bottom electrodes, but their top surfaces were higher than the silicon wafer surface. A layer of photo BCB was then spin-coated on the bottom silicon wafer following the same spinning parameter in the first-generation process (step 4). After applying the photolithography process on the coated BCB layer with photomask 1 again, Cr pads were exposed by having cavities patterned. It has to be mentioned that the diameter of Cr pads is slightly smaller than the cavity diameter due to the over etching control in step 3. This could slightly simplify the mask alignment operation when patterning cavities on the photo BCB layer.

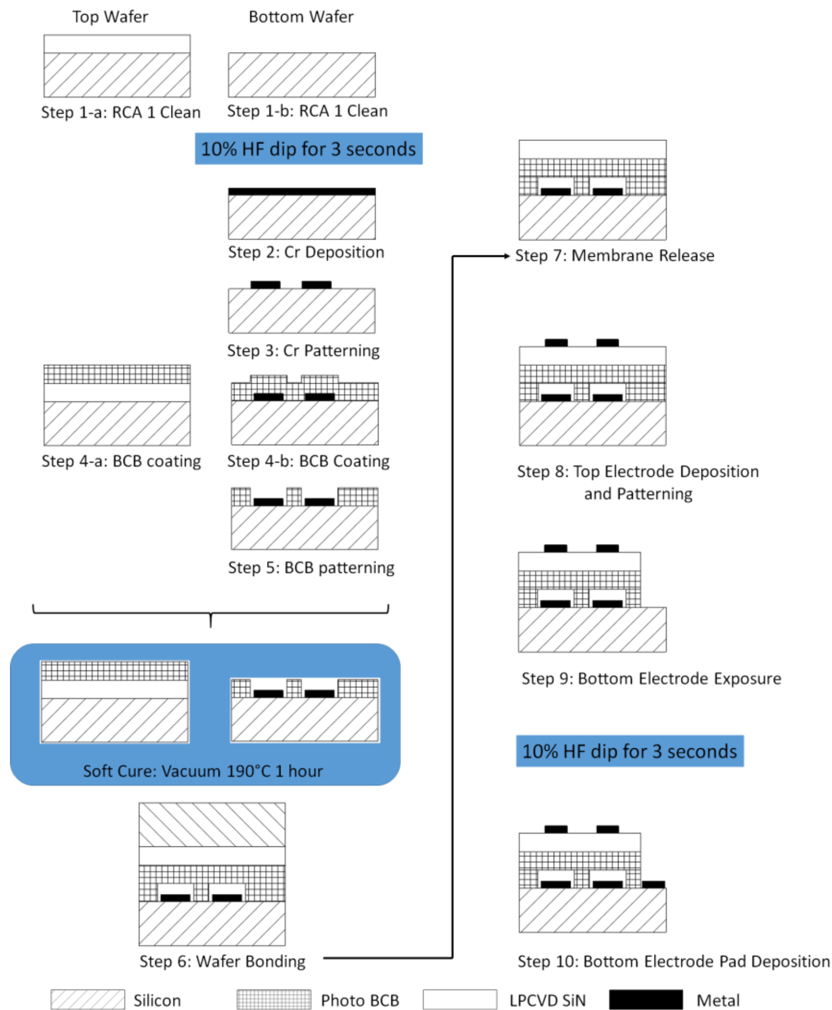

Figure 41: Fabrication process of the second-generation photo BCB CMUTs

After preparing the bottom wafer for bonding, step 4-b, a layer of photo BCB was then spin coated on the top wafer (LPCVD silicon nitride wafer). The coating recipe for adhesive promoter is the same as the one used in the first generation, but the recipe for BCB coating was with lower spin rate (500 RPM for 10 seconds followed by 3000 RPM for 30 seconds). The resulting thickness of photo BCB was about 1.4 μm. The remaining steps have no difference with the ones described in the previous chapter.

6.2 Two-layer Membrane Modelling

The membrane layer of the second generation CMUT is composed of two materials: LPCVD silicon nitride and BCB. Therefore, the vibration performance cannot be simply predicted by the model described in Appendix. Suppose the Young's Modulus, Poisson's ratio, thickness and density of silicon nitride are E_1, ν_1, t_1 and ρ_1; and the ones for photo BCB are E_2, ν_2, t_2 and ρ_2. The transformed flexural rigidity D_t of the two layers can then be calculated by Equation 2 [97].

$$D_t = C - \frac{B^2}{A}$$

$$A = \frac{E_1 t_1}{1 - \nu_1^2} + \frac{E_2 t_2}{1 - \nu_2^2}$$

Equation 2

$$B = \frac{E_1 t_1^2}{2(1 - \nu_1^2)} + \frac{E_2[(t_1 + t_2)^2 - t_1^2]}{2(1 - \nu_2^2)}$$

$$C = \frac{E_1 t_1^3}{3(1 - \nu_1^2)} + \frac{E_2[(t_1 + t_2)^3 - t_1^3]}{3(1 - \nu_2^2)}$$

Then the in-air resonance frequency of the two-layer circular membrane can be calculated by:

$$f_r = \frac{1}{2\pi} \frac{10.22}{\mathrm{a}^2} \sqrt{\frac{D_t}{\rho_1 t_1 + \rho_2 t_2}}$$

Equation 3

6.3 Device Characterization

6.3.1 Structure Dimensions

Focused ion beam was performed to inspect the cross-section dimension of the fabricated CMUT. The FIB-SEM images are given in Figure 42. However, the membrane was found touching the Cr-bottom electrode, which did not coincide with the characterization results performed: the membrane vibrated as expected with no collapse effect under small bias voltage (<100 V). It was thought that the local thermal effect on the BCB film during the ion beam milling process introduced stress in the membrane-BCB film and caused film bending toward bottom Cr electrode [98, 99]. Therefore, another CMUT was physically broken in order to avoid chemical and thermal factors on structure parameters. The SEM images of the physical-broken-cross-section are given in Figure 43. The imaging results showed a non-collapsed membrane, which proves that the 'collapse' effect in FIB-SEM was induced by the ion beam milling. It has to be mentioned that BCB was not completely removed from the cavity area during the lithography process and the BCB residuals partially covered the edge of the Cr bottom electrodes. This can be improved in future by using an extra mask in patterning Cr bottom electrodes with electrode sizes close to the top electrodes.

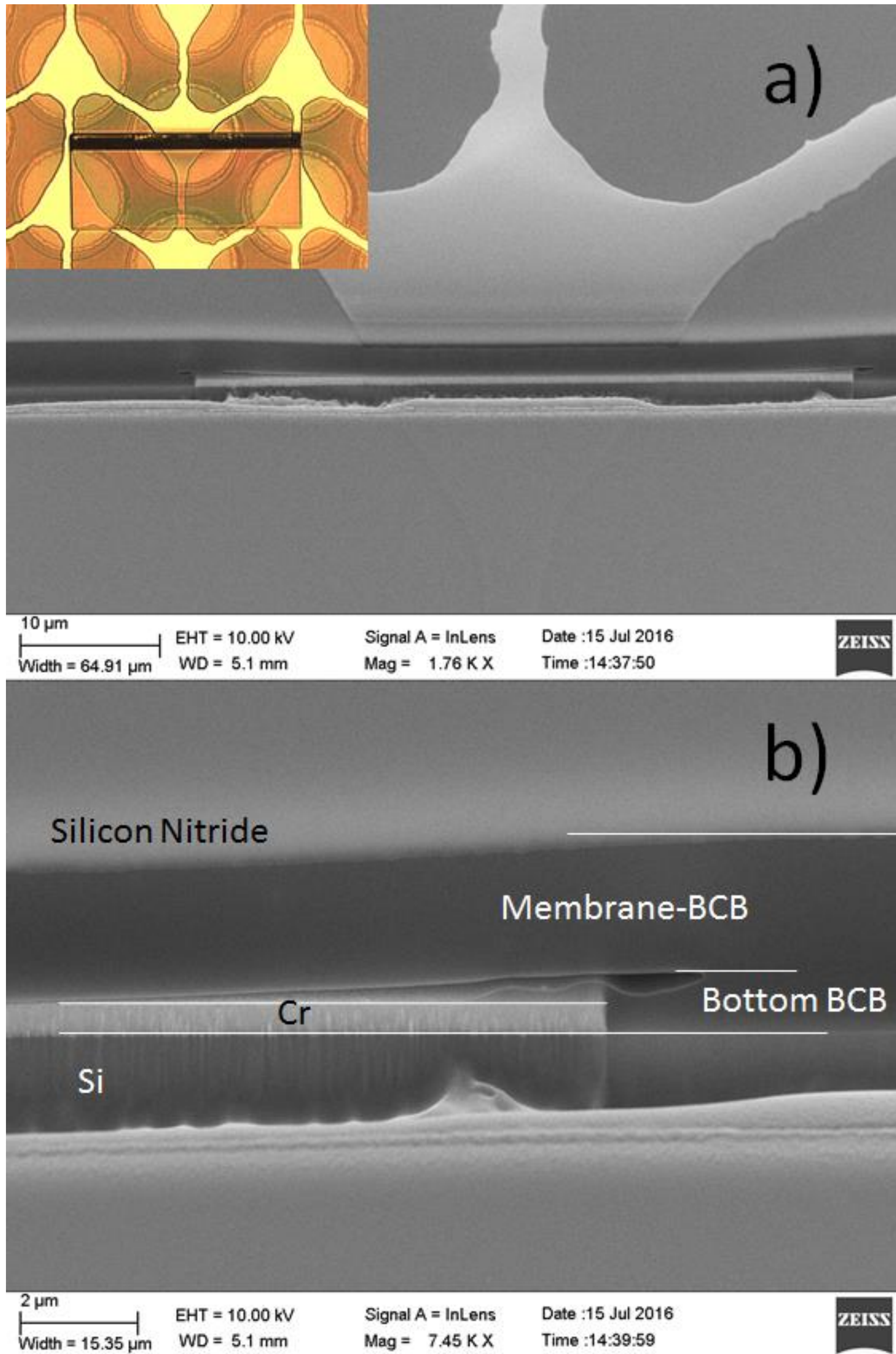

Figure 42: Cross section view of CMUT cell through a window opened by FIB and the image was taken from slanting angle of 54°. The microscopy image on the top left corner of image a) shows the position of the cutting window.

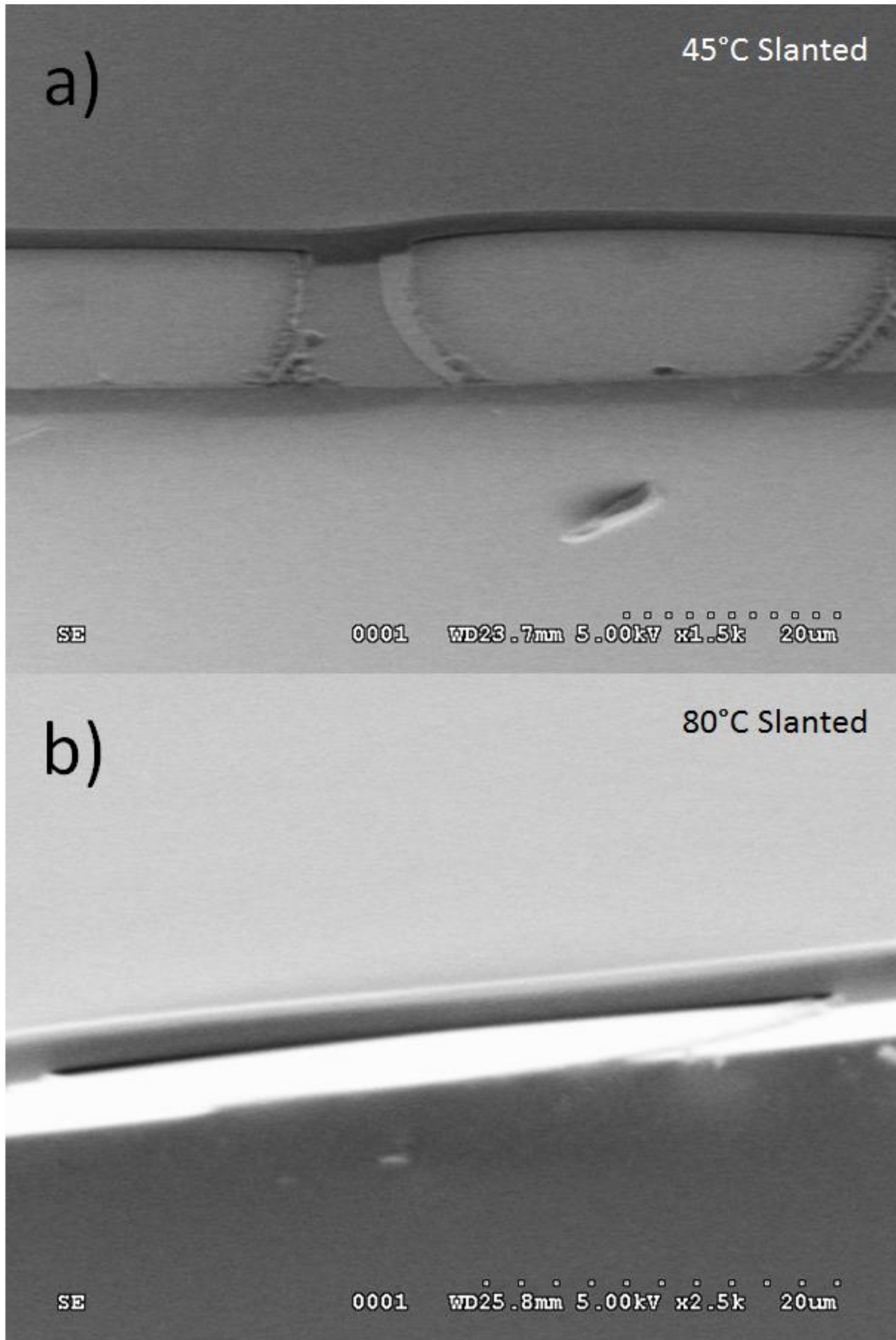

Figure 43: SEM images for cross-section inspection on mechanically broken CMUT at different slanted angle. The images showed that the membrane was not touching the bottom Cr electrodes.

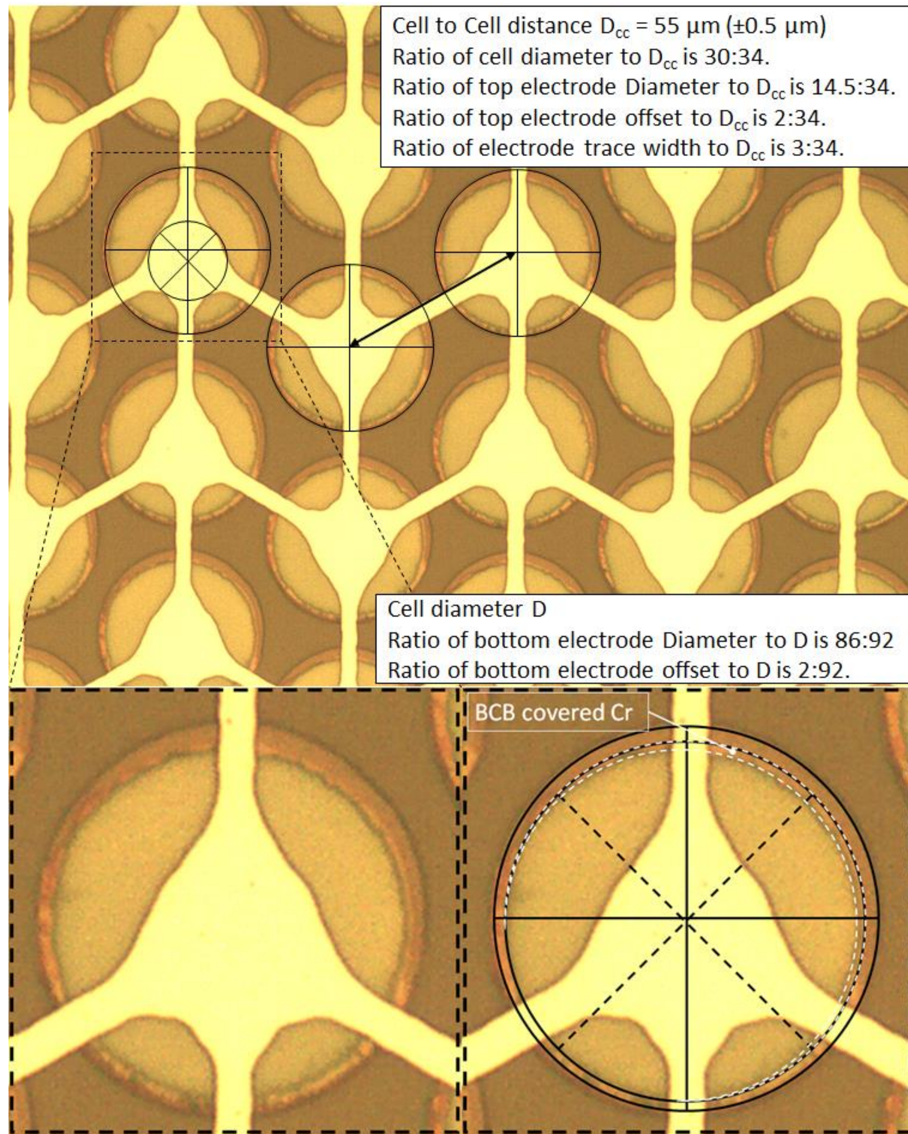

Figure 44: Microscopy image of Generation 2 1D CMUT array. Dimensions were calculated based on the cell to cell distance and the ratio of interested dimensions to the cell to cell distance.

Table 11: Structural dimensions of the second generation CMUT.

Membrane diameter (µm)	48.5
Membrane layer 1 (SiN) thickness (nm)	605
Membrane layer 2 (BCB) thickness (nm)	1311
Cavity depth at wafer centre (nm)	305
Cell to cell distance (µm)	55
Top Electrode diameter (µm)	23.5
Top Electrode thickness (nm)	Cr 30 nm with 65 nm Al on top
Bottom Electode diameter (µm)	45.3
Bottom electrode (Cr section) thickness (nm)	305

6.3.2 In-air Characterization

The VNA measurement results of the CMUT array and the one-element CMUT are given in Figure 45 and Figure 46. The 1-D CMUT array located in the wafer center during fabrication shows resonance frequency of 6.37 MHz, while the one-element CMUT shows 13.3% decrease in resonance frequency (5.52 MHz). This is considered induced by the non-uniform coating of the BCB layer on the top nitride wafer.

As can be found from Figure 13, the non-patterned photo BCB film for process study has average thickness of 1331.3 nm with standard deviation of 13.8 nm after soft cure. Based on the Equation 3, such a small thickness deviation should result in in-air resonance frequency difference of less than 0.2 MHz. However, the measured frequency difference (0.85 MHz) is much larger than the estimated value. In order to explain this disagreement, two possible reasons are considered: 1) photo BCB coating at the edge of the wafer has worse repeatability than the coating in the wafer centre, such that the values obtained from process study can not be used to describe the performance of the CMUTs at the wafer edge; 2) measurement points during ellipsometer measurements in the process study should be increased, such that the photo BCB coating thickness can be evaluated more accurately. Nevertheless, the frequency difference between CMUTs from one wafer requires future work to improve the coating uniformity of photo BCB layer.

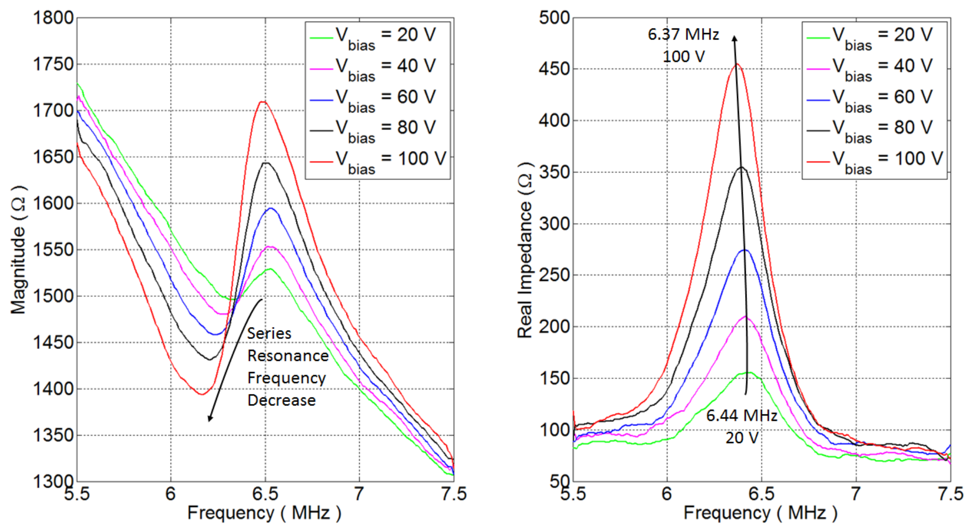

Figure 45: VNA measurement result of second generation CMUT under bias voltage of 20 V to 100 V. The measured element in 1-D CMUT array locates in the centre region of the wafer during fabrication.

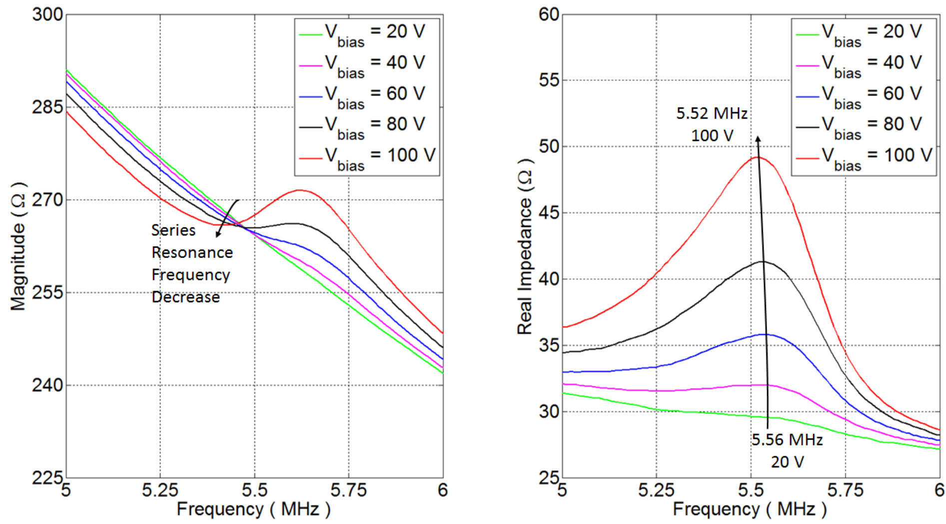

Figure 46: VNA measurement result of second generation CMUT under bias voltage of 20 V to 100 V. The measured one-element CMUT locates at the edge of the wafer during fabrication.

Vibrometer tests were also performed to measure resonance frequencies of each element in the 1-D array. The measurement results are given in Figure 47. The average resonance frequency over 16 elements is 6.4 MHz with standard deviation of 0.27 MHz. The uniformity is much worse than the improved first generation CMUT (deviation of 0.0214 MHz under 100 V bias).

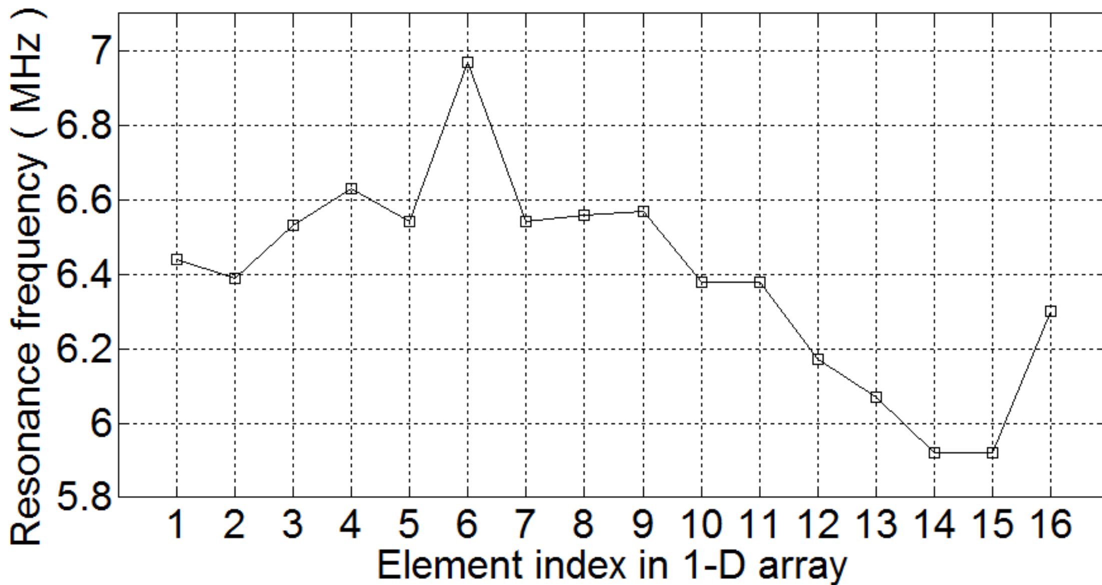

Figure 47: Resonance frequencies of each element in second generation 1-D array CMUT under bias voltage of 100 V with AC signal amplitude of 2.5 V. The average resonance frequency over 16 elements is 6.4 MHz with standard deviation of 0.27MHz.

6.3.3 Immersion Characterization

Same immersion test as described in section 5.2.3 was also performed to the second generation CMUT using one of the element in 1-D array. The measurement result and the frequency domain analysis are given in Figure 48. The immersion resonance appeared at 1.76 MHz when the CMUT was biased at 100 V.

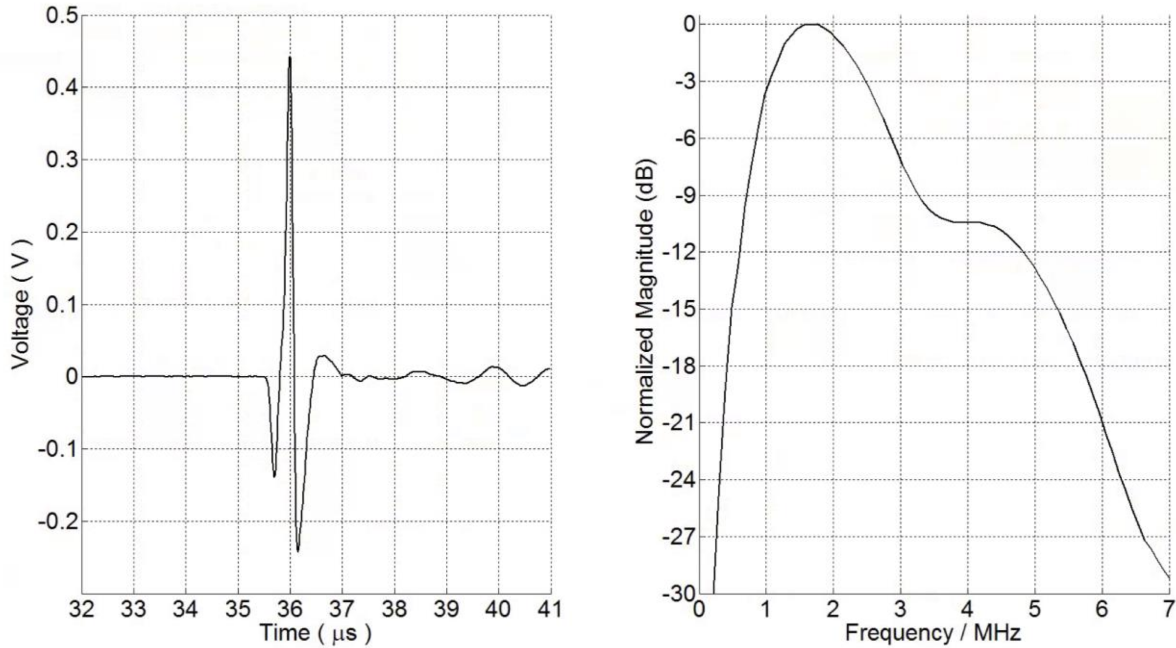

Figure 48: Immersion test result of the second generation CMUT. The immersion resonance

The second-generation design decreased the distance between top and bottom electrode by locally leveling up the bottom electrode top surface. The major effect by doing so is to increase the device capacitance, which further increase the receive sensitivity. In comparison with the receive sensitivity of the optimized first generation CMUT, the ultrasound signal received by the second generation CMUT under the same sound pressure (639 kPa) appeared a peak-to-peak voltage of 684 mV indicating a receive sensitivity of 1070 nmV/Pa, which is more than twice as many as the sensitivity of the optimized first generation (516 nV/Pa). The greatly improved peak to peak voltage, as shown in Figure 49, demonstrated the advantage of second generation CMUT in receiving ultrasound.

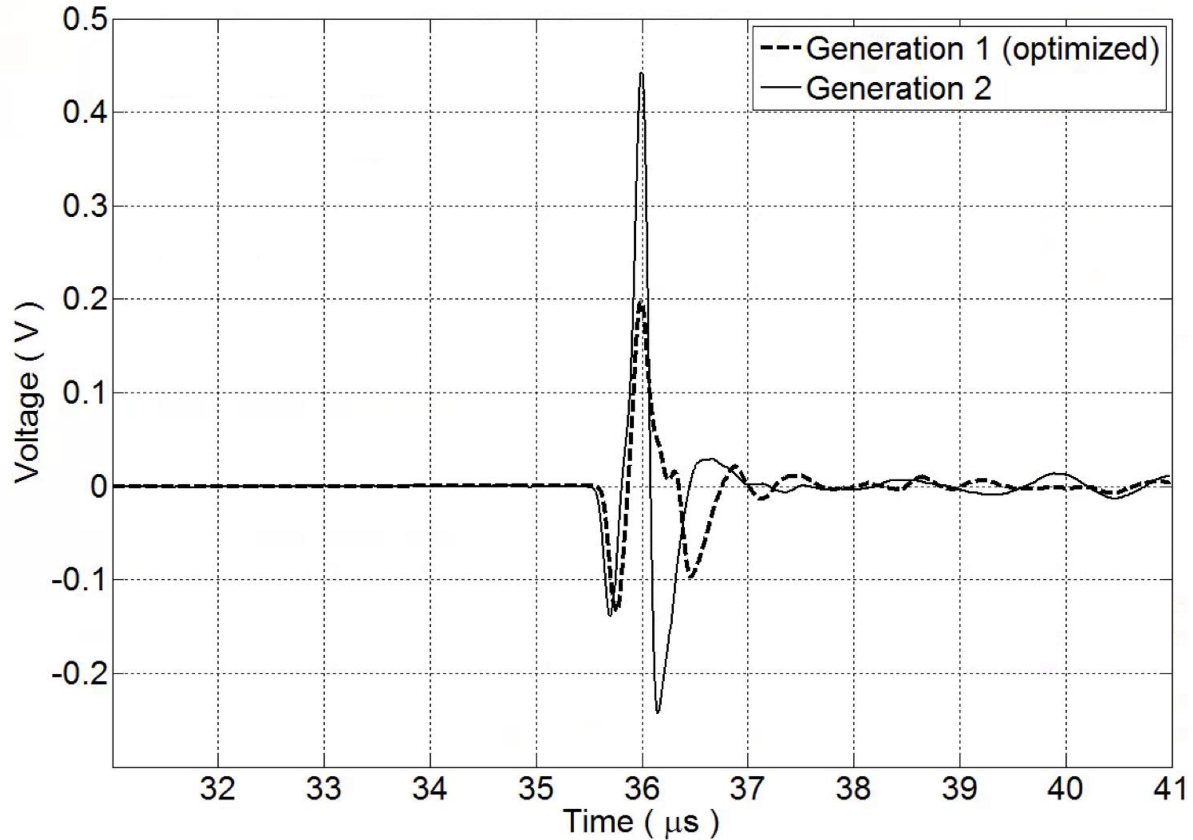

Figure 49: Received ultrasound signal of both the optimized first generation and the second generation CMUTs, which are both biased at 100 V under receive mode against ultrasound waves with same sound pressure.

6.3.4 Discussion in Collapse Voltage

The membrane of CMUTs in the second iteration is one-layer silicon nitride membrane. The membrane of the second generation CMUTs is changed to dual-layer membrane containing both silicon nitride and BCB. Based on Equation 2 and using the same cell diameter and electrode diameter given in Table 11, the flexural rigidities of the one-layer membrane and dual-layer membrane are calculated of 5.22×10^{-9} Pa/m^3 and 9.69×10^{-9} Pa/m^3, respectively. The flexural rigidity of the dual-layer membrane almost doubles the one of the one-layer membrane. It requires larger electrostatic force to deflect the membrane with larger flexural rigidity in order to achieve the same membrane displacement. Therefore, the collapse voltage of the second generation CMUTs could be increased. As illustrated in Figure 50 and Figure 51, the calculated collapse voltage is 183 V, which is higher than the one of the optimized first generation CMUT; and the membrane would also touch the bottom of the cavity before

collapsing. It was still not able to observe any of the collapse effect under microscope. But when network analyzer measurement was performed and the CMUT was bias under DC voltages of up to 200 V, there was no extra peaks showed up, as the one shown in Figure 36. For network analyzer measurement, DC source need to be isolated from the network analyzer with a bias-T in order to protect the network analyzer. The bias-T used for the measure is the model 5530b from Tektronix and it allows maximum DC voltage of 200 V. Thus, it was not able to keep increasing the bias voltage beyond 200 V to inspect the collapse voltage. In this regards, we can only conclude that the real collapse voltage is higher than 200 V, which is also higher than the calculated value and indicates the difference of photo BCB thickness between the measured transducer and the value used in calculation.

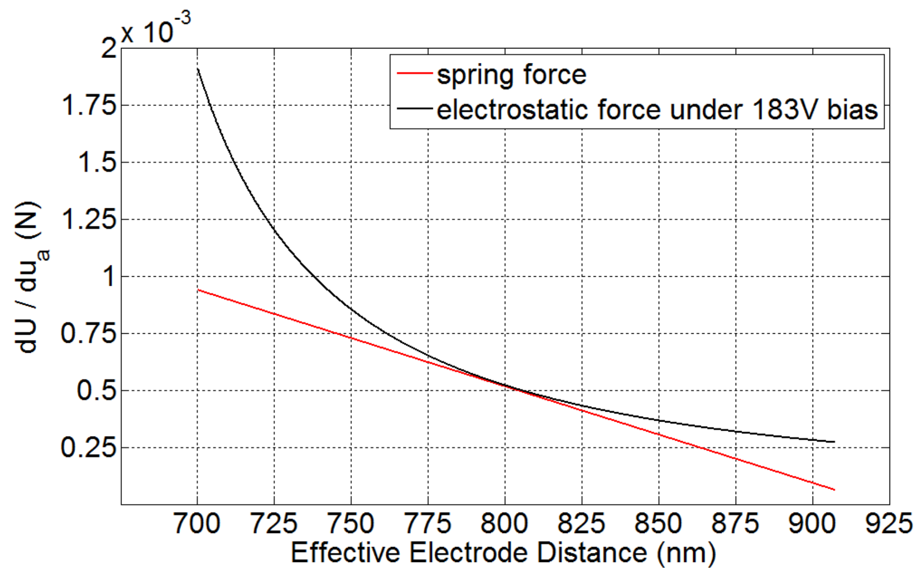

Figure 50: Pull-in voltage calculation based on structure dimensions.

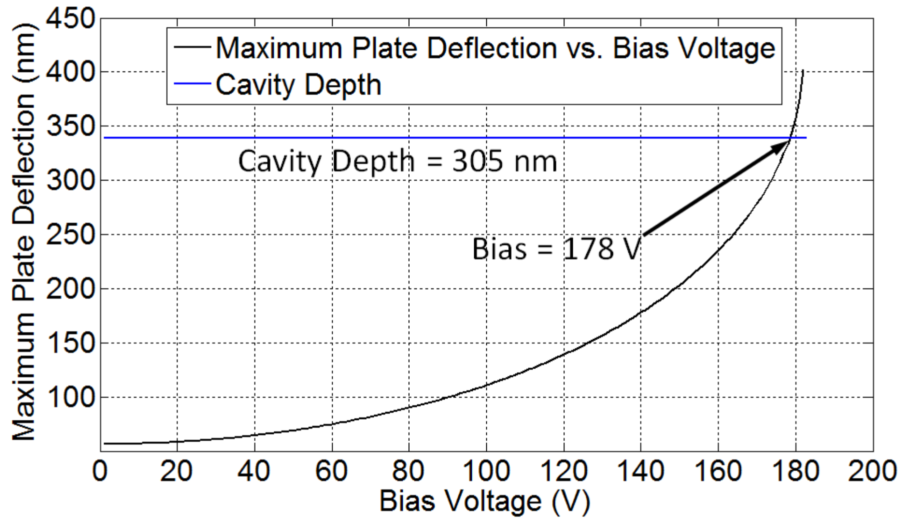

Figure 51: Theoretical calculation results: Maximum plate deflection under bias voltage from 1 V to the calculated pull-in voltage.

6.4 Summary

In this chapter, second generation CMUT fabrication method was described. The fabricated device has the receive-sensitivity greatly enhanced and doesn't require wafer alignment in the bonding step if the process needs to be extended for 2D array fabrication. However, the non-uniform coating of the BCB layer on the top wafer results in non-uniform membrane thickness, which in turn introduced larger resonance frequency variance to CMUTs on different wafer locations during fabrication. For future works using BCB as a part of the membrane layers, one should either take the coating uniformity into account, or BCB coating process must be improved in order to have better transducer quality control.

Chapter 7 Conclusion and Future Works

7.1 Summary of Works

The focus of the reported work in this thesis is the development of a CMUT fabrication process based on adhesive wafer bonding technique. Photo BCB was used as the polymer adhesive, which can be patterned through a lithography process.

The fabrication process starts with photo BCB coating on two separate wafers. One wafer (bottom wafer) is used as a substrate providing bottom electrodes. The other wafer (top wafer) provides a membrane layer, which is the non-polished LPCVD silicon nitride. Cavities can be patterned in the photo BCB film on either the top or the bottom wafer. The wafers with patterned and non-patterned photo BCB are then soft cured (190°C in vacuum oven for one hour plus ramp-up/-down time). The soft cure process is able to remove the chemical or gas residuals in the photo BCB film in order to circumvent deformation and void creation during bonding. The FTIR spectrum of the soft cured photo BCB sample shows that soft cure does not affect the bonding properties of photo BCB. After soft cure, wafers are then bonded in vacuum by bringing two wafers into contact with compressive force and temperature applied. The maximum process temperature during bonding is 250°C, which is also the maximum temperature of the entire fabrication process. Therefore, the developed process is considered CMOS compatible. The bonded wafer pair is then processed with KOH wet etching to remove the substrate-silicon of the top wafer and release the membrane. Top electrodes and wire bonding pads are then deposited and patterned.

There were three iterations for refining the process and redesigning the CMUT structure. The first generation CMUTs (G1 CMUTs) were developed during the first two iterations that explored the fabrication feasibility and solved the fabrication issues including adhesive deformation, bonding voids and high bias voltage. G1 CMUTs have cavities patterned on the top wafer resulting in single-layer membrane. For given cavity diameter, 50 μm as designed, the uniformity of the resonance frequency among CMUT cells is determined by the membrane thickness uniformity. The membrane material is the LPCVD silicon nitride film with thickness of 605 nm and standard deviation up to 15 nm. Thus, the resulting in-air resonance frequency

differences could be within the range of about ± 0.12 MHz with mean frequency of 4.5 MHz and the immersion resonance frequency differences could be within the range of about ± 0.05 MHz with mean frequency of 1.4 MHz.

Moreover, G1 CMUTs still had limitations in controlling the distance between top and bottom electrodes. Although 1-D CMUT arrays were fabricated, 2-D CMUT arrays were difficult to fabricate using the same process since it required wafer alignment during the bonding step. As a result, there was a need to redesign the CMUT structure and alter the fabrication process accordingly. This resulted in the second generation CMUTs (G2 CMUT) and it was achieved in the third iteration.

G2 CMUTs have cavities patterned on the bottom wafer and the top wafer has non-patterned silicon nitride and BCB together as a membrane layer. Then, there is no need of wafer alignment during wafer bonding as there is no pattern on the top wafer. Furthermore, the Cr layer was deposited on the bottom silicon wafer and patterned into circular shape being concentric with cavities. The distance between top and bottom electrode can then be further decreased by controlling the thickness of the Cr layer on the bottom wafer. Benefitting from the closer electrode distance, the sensitivity of CMUT in receive mode was increased, by more than twice compared to that of G1 CMUTs.

The G2 CMUTs have slightly smaller cell diameter (48.5 μm compared with 50 μm in diameter), but present much increased resonance frequency due to the thicker membrane. However, the two-layer membrane and the thickness uniformity depends on not only the uniformity of the silicon nitride layer, but also the non-patterned photo BCB film. It was found that the non-patterned photo BCB film before bonding has a thickness standard deviation of about 13.8 nm. The uniformity after bonding was not measured yet. We can assume the non-patterned photo BCB film has similar uniformity before and after wafer bonding since the photo BCB layer didn’t show any deformation after wafer bonding. Then, by counting the uniformity of the silicon nitride layer, the in-air resonance frequency could be within the range of about ± 0.11 MHz with mean frequency of 6.7 MHZ. However, this estimation is not able to evaluate the performance of CMUTs at the edge of the wafer due to the poor coating uniformity of photo BCB along the wafer edge.

7.2 Future Works

The coating uniformity of BCB layers still needs to be enhanced. Spray coating might be a way to achieve better uniformity. However, the spray coating would be suitable only for industrial batch fabrication in regards of process development cost. Thermal treatment could also be useful in film planarization; BCB could reflow at certain temperature, but the cross-linking level should be carefully controlled to not negatively affect the bonding.

Secondly, dielectric charging in the layers of silicon nitride and BCB still need to be studied since it directly relates to the transducer's durability. Signal weakening by longer operation time has been observed when testing the CMUTs with high voltage bias (> 100 V), which indicates the existence of trapped charges in the insulating layers. Therefore, structure dimensions should also be carefully designed in order to have the operation voltage minimized.

Lastly, BCB showed great features of low process temperature, optical transparency, and flexibility in selecting bonding materials. All of these features haven't been fully utilized in the three iterations. Therefore, new structures should be designed and fabricated to study the feasibility and explore potential problems.

CMUT 2D array

A prime candidate to be considered in future would be a 2D CMUT array. Based on the third iteration process, the bottom wafer can be made of insulating materials (glass or silicon oxide) with patterned-conductive layer deposited as bottom electrodes, as illustrated in Figure 52. BCB can then be deposited and patterned with cavities on the bottom wafer. After wafer bonding using electrically insulating materials for the membrane, top electrodes can be patterned to form a 2D array.

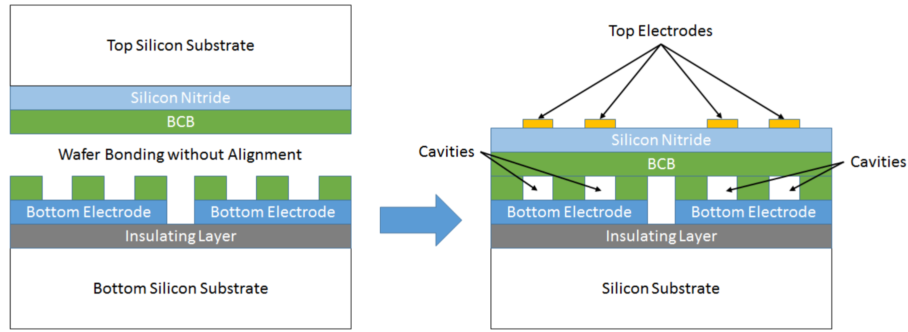

Figure 52: Illustration of 2D CMUT array fabrication process.

CMOS integration

The second item to be considered in future would be the integration of CMUT fabrication with CMOS process. The maximum process temperature of this BCB process is 250°C, which means that BCB CMUTs can be fabricated directly on IC chips. After finishing the CMOS process and before dicing the wafer, the un-diced IC-wafer can be used as a bottom wafer for CMUTs. A feasibility study has been carried out toward integrating CMUTs with ICs. The process to fabricate a second-generation CMUT onto a chip with application specific integrated circuit (ASIC) is shown in Figure 53. The ASIC was designed with pulsers for actuating CMUTs to generate ultrasound and amplifiers for ultrasonic signal receiving, which has been described in [53]. Microscopy image of the chip, which is given in Figure 54, illustrates the electrode setup of an amplifier. CMUTs to be fabricated on the chip should have the bottom electrodes be connected with the chip electrodes for pulsing and signal receiving. The major difficulty of the process is about dealing with the uneven chip surface with variance of ±1.5 μm. Unlike the bottom flat wafer used in the three iterations, uneven chip surface with non-flat top surface is not suitable for wafer bonding. In order to overcome this barrier, a layer of silicon nitride was first bonded with the chip providing a flat bonding surface. The remaining processes can then be carried out on the flat silicon nitride substrate. The steps from 1 to 7 as illustrated in Figure 53 have been achieved. However, the ASIC size is about 3.5 mm by 3.5 mm. There was significant ring effect when spin coating the BCB, which resulted in failed bonding in the step 8. Nevertheless, the ring effect will not appear when working with a non-diced wafer, thus the proposed process can be considered feasible.

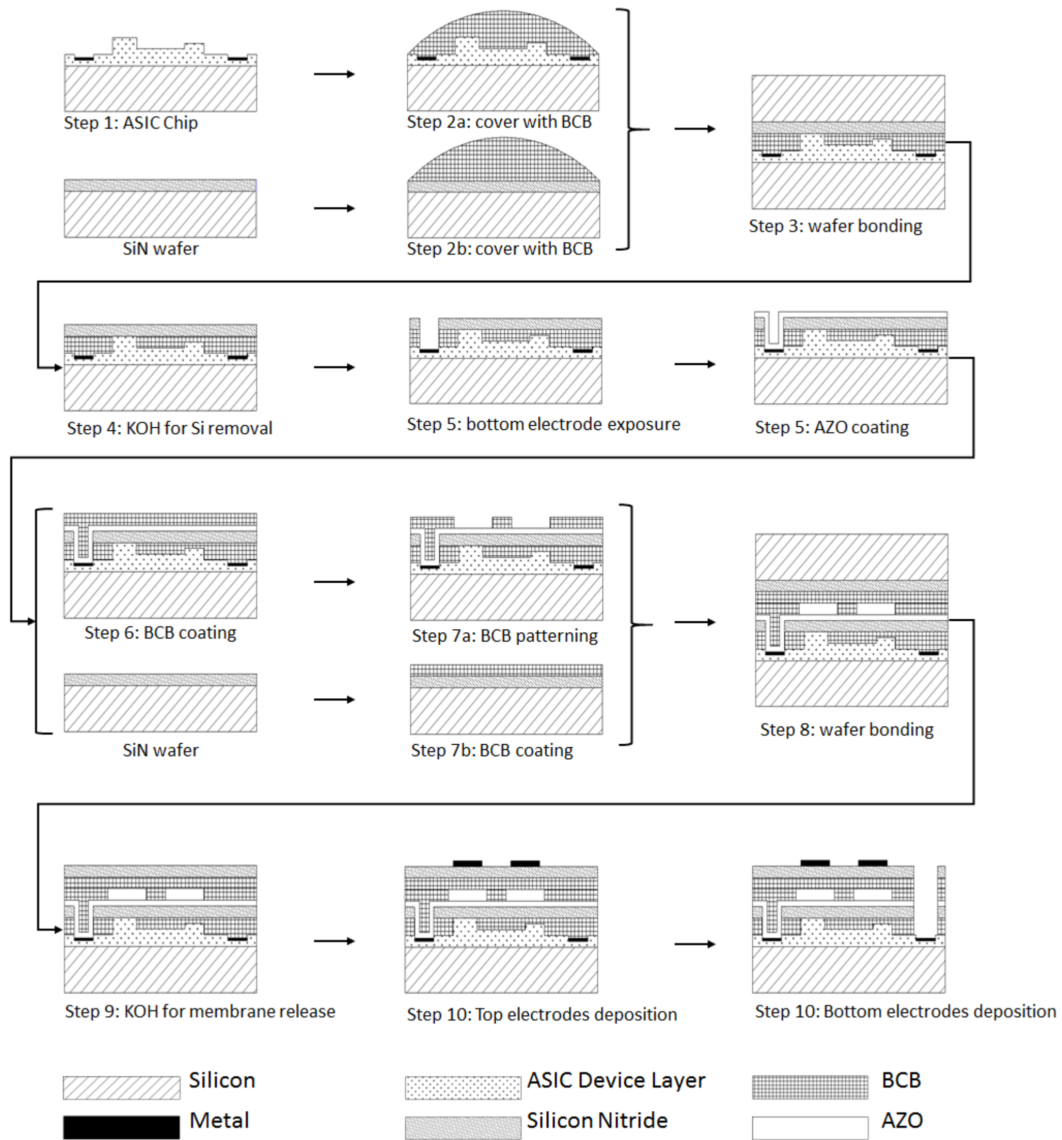

Figure 53: A process designed for integrating CMUT fabrication with a fabricated ASIC chip.

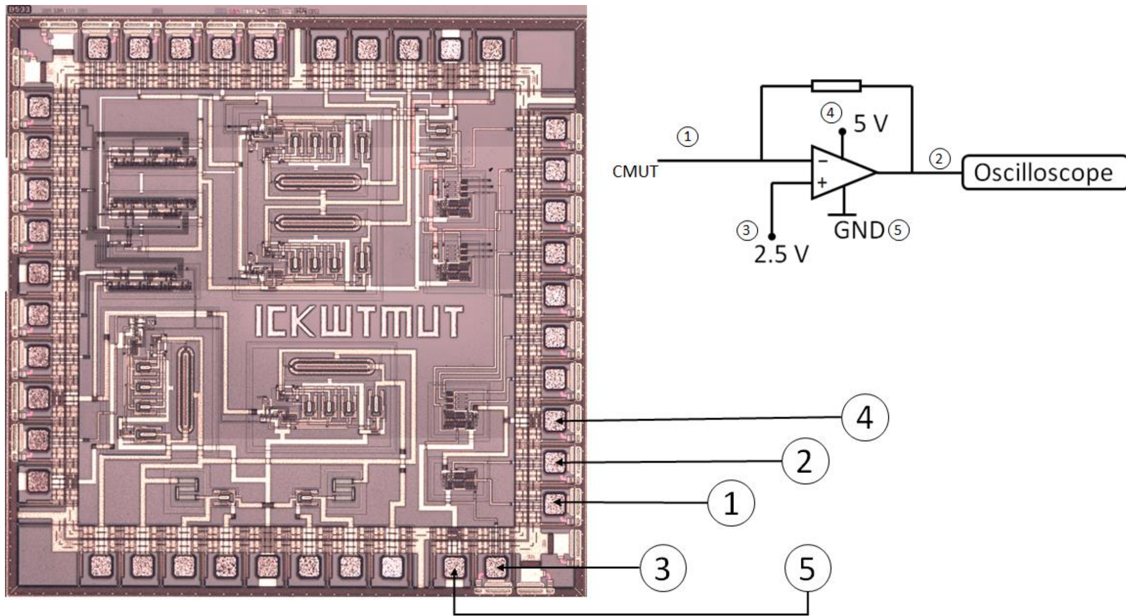

Figure 54: Microscopy image of the ASIC chip. The size of the chip is about 3.5 mm by 3.5 mm. Electrodes for amplifier setup are also illustrated.

Flexible CMUT

A flexible CMUT can be curved to have larger imaging volume and conformably attached with a cylinder-shape probe for small area imaging [38]. The conventional method of making CMUTs flexible is to fabricate the CMUT first followed with substrate thinning. When the silicon substrate is thin enough, 5µm for instance, CMUTs can be curved to certain curvature without being broken. Compared with conventional methods, adhesive wafer bonding using BCB as an adhesive can enable wafer bonding on flexible materials such as polyimide film. An illustration of the fabrication process is given in Figure 55. Instead of thinning the substrate after device fabrication, a flexible substrate is attached to the substrate silicon surface in the very beginning of the process. The CMUT was then achieved by bonding the top wafer with the surface of the flexible layer. By simply removing the substrate silicon, CMUTs become flexible and the curvature depends on the selected flexible material. For future work, not only should the process feasibility be tested, the CMUT performance under bending stress should also be studied.

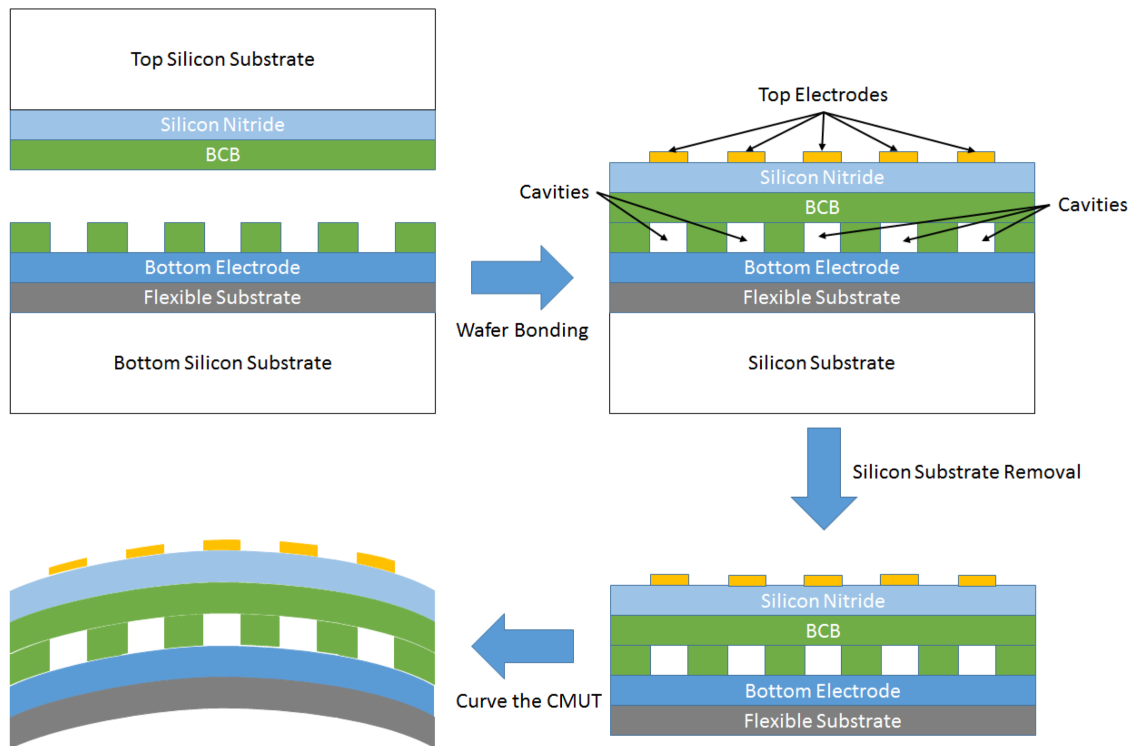

Figure 55: Illustration of flexible CMUT fabrication process.

7.3 Concluding Remarks

The project explored the flexibility of CMUT structure design based on the use of photo BCB. The results are overall satisfactory. Compared with conventional fabrication techniques, the developed processes during the first and second iterations shows the most simplified process with low wafer cost and low process temperature. Tolerance to contaminations at the wafer bonding interface are also demonstrated. The turn-around time of one fabrication process was approximately one week with about 60% yield during process development. Based on the fabrication experience, the yield can be increased to more than 80% for 4"-wafer process if the processes are repeated. The limitations in applying polymer adhesive wafer bonding are mainly related to the uniformity of the adhesive coating. The non-uniform coating could result in performance variance in operation frequency and bias voltage. Further improvements regarding coating uniformity are required as future works.

Secondly, the adhesive wafer bonding using photo BCB is much easier to achieve than direct wafer bonding or anodic wafer bonding. It requires less attention to contaminations and there is no need of high temperature annealing after bonding. The wafer surfaces for bonding also do not need to be as smooth as a silicon wafer, so polishing steps are unnecessary. As a result, it only takes about three hours to achieve a successful bond with minimal care.

Lastly, the applied polymer adhesive is photosensitive, requires low processing temperature and is compatible with varies coating substrates. Silicon wafers, silicon with LPCVD silicon nitride coatings, and glass wafers with aluminum zinc oxide coating have been achieved via wafer bonding using photo BCB as adhesive. Theoretically speaking, the glass wafer itself and silicon wafer with a coating of thermal oxide, aluminum, copper or chromium are also applicable for wafer bonding.

Letter of Copyright Permission[3]

SPRINGER LICENSE TERMS AND CONDITIONS

Dec 08, 2016

This Agreement between Zhenhao Li ("You") and Springer ("Springer") consists of your license details and the terms and conditions provided by Springer and Copyright Clearance Center.

License Number	4004390618091
License date	Dec 08, 2016
Licensed Content Publisher	Springer
Licensed Content Publication	Microsystem Technologies
Licensed Content Title	Fabrication and characterization of sealed cavities realized by adhesive wafer bonding with dry etched Cyclotene™
Licensed Content Author	Aref Bakhtazad
Licensed Content Date	Jan 1, 2015
Licensed Content Volume Number	21
Licensed Content Issue Number	11
Type of Use	Thesis/Dissertation
Portion	Figures/tables/illustrations
Number of figures/tables/illustrations	1
Author of this Springer article	No
Order reference number	
Original figure numbers	Figure 1
Title of your thesis / dissertation	Fabrication of Capacitive Micromachined Ultrasonic Transducers based on Adhesive Wafer Bonding
Expected completion date	Dec 2016
Estimated size(pages)	110
Requestor Location	Zhenhao Li Department of System Design Engineering University of Waterloo 200 University Ave. W. Waterloo, ON N2L3G1 Canada Attn: Zhenhao Li
Billing Type	Invoice
Billing Address	Zhenhao Li Department of System Design Engineering University of Waterloo 200 University Ave. W. Waterloo, ON N2L3G1 Canada Attn: Zhenhao Li
Total	0.00 CAD

[3] This Letter of Copyright Permission is for the Figure 6, which partially reused the content in the reference [62].

Terms and Conditions

Introduction

The publisher for this copyrighted material is Springer. By clicking "accept" in connection with completing this licensing transaction, you agree that the following terms and conditions apply to this transaction (along with the Billing and Payment terms and conditions established by Copyright Clearance Center, Inc. ("CCC"), at the time that you opened your Rightslink account and that are available at any time at http://myaccount.copyright.com).

Limited License

With reference to your request to reuse material on which Springer controls the copyright, permission is granted for the use indicated in your enquiry under the following conditions: - Licenses are for one-time use only with a maximum distribution equal to the number stated in your request.

- Springer material represents original material which does not carry references to other sources. If the material in question appears with a credit to another source, this permission is not valid and authorization has to be obtained from the original copyright holder.

- This permission

- is non-exclusive
- is only valid if no personal rights, trademarks, or competitive products are infringed.
- explicitly excludes the right for derivatives.

- Springer does not supply original artwork or content.

- According to the format which you have selected, the following conditions apply accordingly:

- Print and Electronic: This License include use in electronic form provided it is password protected, on intranet, or CD-Rom/DVD or E-book/E-journal. It may not be republished in electronic open access.
- Print: This License excludes use in electronic form.
- Electronic: This License only pertains to use in electronic form provided it is password protected, on intranet, or CD-Rom/DVD or E-book/E-journal. It may not be republished in electronic open access.

For any electronic use not mentioned, please contact Springer at permissions.springer@spiglobal.com.

- Although Springer controls the copyright to the material and is entitled to negotiate on rights, this license is only valid subject to courtesy information to the author (address is given in the article/chapter).

- If you are an STM Signatory or your work will be published by an STM Signatory and you are requesting to reuse figures/tables/illustrations or single text extracts, permission is granted according to STM Permissions Guidelines: http://www.stm-assoc.org/permissionsguidelines/

For any electronic use not mentioned in the Guidelines, please contact Springer at permissions.springer@spi-global.com. If you request to reuse more content than stipulated in the STM Permissions Guidelines, you will be charged a permission fee for the excess content.

Permission is valid upon payment of the fee as indicated in the licensing process. If permission is granted free of charge on this occasion, that does not prejudice any rights we might have to charge for reproduction of our copyrighted material in the future. -If your request is for reuse in a Thesis, permission is granted free of charge under the following conditions:

This license is valid for one-time use only for the purpose of defending your thesis and with a maximum of 100 extra copies in paper. If the thesis is going to be published, permission needs to be reobtained.

- includes use in an electronic form, provided it is an author-created version of the thesis on his/her own website and his/her university's repository, including UMI (according to the definition on the Sherpa website: http://www.sherpa.ac.uk/romeo/); - is subject to courtesy information to the co-author or corresponding author.

Geographic Rights: Scope

Licenses may be exercised anywhere in the world.

Altering/Modifying Material: Not Permitted

Figures, tables, and illustrations may be altered minimally to serve your work. You may not alter or modify text in any manner. Abbreviations, additions, deletions and/or any other alterations shall be made only with prior written authorization of the author(s).

Reservation of Rights

Springer reserves all rights not specifically granted in the combination of (i) the license details provided by you and accepted in the course of this licensing transaction and (ii) these terms and conditions and (iii) CCC's Billing and Payment terms and conditions.

License Contingent on Payment

While you may exercise the rights licensed immediately upon issuance of the license at the end of the licensing process for the transaction, provided that you have disclosed complete and accurate details of your proposed use, no license is finally effective unless and until full payment is received from you (either by Springer or by CCC) as provided in CCC's Billing and

Payment terms and conditions. If full payment is not received by the date due, then any license preliminarily granted shall be deemed automatically revoked and shall be void as if never granted. Further, in the event that you breach any of these terms and conditions or any of CCC's Billing and Payment terms and conditions, the license is automatically revoked and shall be void as if never granted. Use of materials as described in a revoked license, as well as any use of the materials beyond the scope of an unrevoked license, may constitute copyright infringement and Springer reserves the right to take any and all action to protect its copyright in the materials.

Copyright Notice: Disclaimer

You must include the following copyright and permission notice in connection with any reproduction of the licensed material:

"Springer book/journal title, chapter/article title, volume, year of publication, page, name(s) of author(s), (original copyright notice as given in the publication in which the material was originally published) "With permission of Springer"

In case of use of a graph or illustration, the caption of the graph or illustration must be included, as it is indicated in the original publication.

Warranties: None

Springer makes no representations or warranties with respect to the licensed material and adopts on its own behalf the limitations and disclaimers established by CCC on its behalf in its Billing and Payment terms and conditions for this licensing transaction.

Indemnity

You hereby indemnify and agree to hold harmless Springer and CCC, and their respective officers, directors, employees and agents, from and against any and all claims arising out of your use of the licensed material other than as specifically authorized pursuant to this license.

No Transfer of License

This license is personal to you and may not be sublicensed, assigned, or transferred by you without Springer's written permission.

No Amendment Except in Writing

This license may not be amended except in a writing signed by both parties (or, in the case of Springer, by CCC on Springer's behalf).

Objection to Contrary Terms

Springer hereby objects to any terms contained in any purchase order, acknowledgment, check endorsement or other writing prepared by you, which terms are inconsistent with these terms and conditions or CCC's Billing and Payment terms and conditions. These terms and conditions, together with CCC's Billing and Payment terms and conditions (which are incorporated herein), comprise the entire agreement between you and Springer (and CCC) concerning this licensing transaction. In the event of any conflict between your obligations established by these terms and conditions and those established by CCC's Billing and Payment terms and conditions, these terms and conditions shall control.

Jurisdiction

All disputes that may arise in connection with this present License, or the breach thereof, shall be settled exclusively by arbitration, to be held in the Federal Republic of Germany, in accordance with German law.

Other conditions:

V 12AUG2015

Questions? customercare@copyright.com or +1-855-239-3415 (toll free in the US) or +1-978-646-2777.

Bibliography

[1] M. Haller and B. T. Khuri-Yakub, "A surface micromachined electrostatic ultrasonic air transducer," *Ultrasonics, Ferroelectrics, and Frequency Control, IEEE Transactions on,* vol. 43, pp. 1-6, 1996.

[2] D. M. Mills, "Medical imaging with capacitive micromachined ultrasound transducer (cMUT) arrays," in *Ultrasonics Symposium, 2004 IEEE*, 2004, pp. 384-390.

[3] A. Buhrdorf, O. Ahrens, and J. Binder, "Capacitive micromachined ultrasonic transducers and their application," in *Ultrasonics Symposium, 2001 IEEE*, 2001, pp. 933-940.

[4] D. Schindel and D. Hutchins, "Applications of micromachined capacitance transducers in air-coupled ultrasonics and nondestructive evaluation," *Ultrasonics, Ferroelectrics, and Frequency Control, IEEE Transactions on,* vol. 42, pp. 51-58, 1995.

[5] A. Logan and J. T. Yeow, "Fabricating capacitive micromachined ultrasonic transducers with a novel silicon-nitride-based wafer bonding process," *Ultrasonics, Ferroelectrics, and Frequency Control, IEEE Transactions on,* vol. 56, pp. 1074-1084, 2009.

[6] A. Erguri, Y. Huang, X. Zhuang, Ö. Oralkan, G. G. Yarahoglu, and B. T. Khuri-Yakub, "Capacitive micromachined ultrasonic transducers: fabrication technology," *Ultrasonics, Ferroelectrics, and Frequency Control, IEEE Transactions on,* vol. 52, pp. 2242-2258, 2005.

[7] P. Ramm, J. J.-Q. Lu, and M. M. Taklo, *Handbook of Wafer Bonding*: John Wiley & Sons, 2012.

[8] Y. Tsuji, M. Kupnik, and B. T. Khuri-Yakub, "Low temperature process for CMUT fabrication with wafer bonding technique," in *Ultrasonics Symposium (IUS), 2010 IEEE*, 2010, pp. 551-554.

[9] S. Bengtsson and P. Amirfeiz, "Room temperature wafer bonding of silicon, oxidized silicon, and crystalline quartz," *Journal of Electronic Materials,* vol. 29, pp. 909-915, 2000.

[10] G. Gurun, C. Tekes, J. Zahorian, T. Xu, S. Satir, M. Karaman*, et al.*, "Single-chip CMUT-on-CMOS front-end system for real-time volumetric IVUS and ICE imaging," *IEEE transactions on ultrasonics, ferroelectrics, and frequency control,* vol. 61, pp. 239-250, 2014.

[11] J. Zahorian, M. Hochman, T. Xu, S. Satir, G. Gurun, M. Karaman*, et al.*, "Monolithic CMUT-on-CMOS integration for intravascular ultrasound applications," *IEEE transactions on ultrasonics, ferroelectrics, and frequency control,* vol. 58, pp. 2659-2667, 2011.

[12] G. Gurun, P. Hasler, and F. L. Degertekin, "Front-end receiver electronics for high-frequency monolithic CMUT-on-CMOS imaging arrays," *IEEE transactions on ultrasonics, ferroelectrics, and frequency control,* vol. 58, pp. 1658-1668, 2011.

[13] S. H. Wong, R. D. Watkins, M. Kupnik, K. B. Pauly, and B. T. Khuri-Yakub, "Feasibility of MR-temperature mapping of ultrasonic heating from a CMUT," *IEEE transactions on ultrasonics, ferroelectrics, and frequency control,* vol. 55, pp. 811-818, 2008.

[14] M. Wang and J. Chen, "Volumetric flow measurement using an implantable CMUT array," *IEEE transactions on biomedical circuits and systems,* vol. 5, pp. 214-222, 2011.

[15] R. Przybyla, A. Flynn, V. Jain, S. Shelton, A. Guedes, I. Izyumin*, et al.*, "A micromechanical ultrasonic distance sensor with> 1 meter range," in *2011 16th International Solid-State Sensors, Actuators and Microsystems Conference*, 2011, pp. 2070-2073.

[16] S. H. Wong, M. Kupnik, R. D. Watkins, K. Butts-Pauly, and B. T. Khuri-Yakub, "Capacitive micromachined ultrasonic transducers for therapeutic ultrasound applications," *IEEE transactions on Biomedical Engineering,* vol. 57, pp. 114-123, 2010.

[17] M. Thränhardt, P.-C. Eccardt, H. Mooshofer, P. Hauptmann, and L. Degertekin, "A resonant CMUT sensor for fluid applications," in *Sensors, 2009 IEEE*, 2009, pp. 878-883.

[18] M. Wang, J. Chen, X. Cheng, T. Zhang, and X. Liu, "A bi-directional real-time blood flowmeter using an implantable CMUT array," in *2008 IEEE Ultrasonics Symposium*, 2008, pp. 1-4.

[19] S. Vaithilingam, T.-J. Ma, Y. Furukawa, I. O. Wygant, X. Zhuang, A. De La Zerda*, et al.*, "Three-dimensional photoacoustic imaging using a two-dimensional CMUT array," *IEEE transactions on ultrasonics, ferroelectrics, and frequency control,* vol. 56, pp. 2411-2419, 2009.

[20] R. K. Chee, P. Zhang, M. Maadi, and R. J. Zemp, "Multi-Frequency Interlaced CMUTs for Photoacoustic Imaging," *IEEE Transactions on Ultrasonics, Ferroelectrics, and Frequency Control,* 2016.

[21] J. H. Jang, M. F. Rasmussen, A. Bhuyan, H.-S. Yoon, A. Moini, C. Chang*, et al.*, "Dual-mode integrated circuit for imaging and HIFU with 2-D CMUT arrays," in *Ultrasonics Symposium (IUS), 2015 IEEE International*, 2015, pp. 1-4.

[22] T.-C. Cheng, C.-W. C. Hsu, H.-C. Wang, and T.-H. Tsai, "A low-power oscillator-based readout interface for medical ultrasonic sensors," in *2016 International Symposium on VLSI Design, Automation and Test (VLSI-DAT)*, 2016, pp. 1-4.

[23] N. Lamberti, G. Caliano, A. Iula, and A. S. Savoia, "A high frequency cMUT probe for ultrasound imaging of fingerprints," *Sensors and Actuators A: Physical,* vol. 172, pp. 561-569, 2011.

[24] V. G. Chouvardas, A. N. Miliou, and M. N. Hatalis, "Design of a Tactile Display Based on a High Power CMUT Array," in *Informatics (PCI), 2012 16th Panhellenic Conference on*, 2012, pp. 228-233.

[25] A. Octavio, R. L. O'Leary, S. M. Whiteley, Ó. Martínez-Graullera, C. J. Martín-Arguedas, L. Gómez-Ullate*, et al.*, "Air-coupled linear and sparse cMUT array manufactured using MUMPs process," *Microsystem technologies,* vol. 17, pp. 1635-1644, 2011.

[26] R. Zhang, W. Zhang, C. He, J. Song, L. Mu, J. Cui*, et al.*, "Design of Capacitive Micromachined Ultrasonic Transducer (CMUT) linear array for underwater imaging," *Sensor Review,* vol. 36, pp. 77-85, 2016.

[27] A. Unlugedik, A. S. Tasdelen, A. Atalar, and H. Koymen, "Designing transmitting CMUT cells for airborne applications," *IEEE transactions on ultrasonics, ferroelectrics, and frequency control,* vol. 61, pp. 1899-1910, 2014.

[28] S. Na, A. I. Chen, L. L. Wong, Z. Li, M. Macecek, and J. T. Yeow, "Capacitive micromachined ultrasonic transducers based on annular cell geometry for air-coupled applications," *Ultrasonics,* vol. 71, pp. 152-160, 2016.

[29] S. Fanget, S. Hentz, P. Puget, J. Arcamone, M. Matheron, E. Colinet*, et al.*, "Gas sensors based on gravimetric detection—A review," *Sensors and Actuators B: Chemical,* vol. 160, pp. 804-821, 2011.

[30] D. Barauskas, G. Vanagas, D. Virzonis, A. Ramanaviciene, A. Makaraviciute, and A. Ramanavicius, "Application of CMUT as immunosensor," in *2013 IEEE International Ultrasonics Symposium (IUS)*, 2013, pp. 1708-1711.

[31] H. J. Lee, K. K. Park, M. Kupnik, O. Oralkan, and B. T. Khuri-Yakub, "Chemical vapor detection using a capacitive micromachined ultrasonic transducer," *Analytical chemistry,* vol. 83, pp. 9314-9320, 2011.

[32] H. J. Lee, K. K. Park, O. Oralkan, M. Kupnik, and B. T. Khuri-Yakub, "CMUT as a chemical sensor for DMMP detection," in *2008 IEEE International Frequency Control Symposium*, 2008, pp. 434-439.

[33] K. Park, H. Lee, G. Yaralioglu, A. Ergun, Ö. Oralkan, M. Kupnik*, et al.*, "Capacitive micromachined ultrasonic transducers for chemical detection in nitrogen," *Applied Physics Letters,* vol. 91, p. 094102, 2007.

[34] K. Park, H. Lee, M. Kupnik, O. Oralkan, and B. Khuri-Yahub, "Fabricating capacitive micromachined ultrasonic transducers with direct wafer-bonding and LOCOS technology," in *Micro Electro Mechanical Systems, 2008. MEMS 2008. IEEE 21st International Conference on*, 2008, pp. 339-342.

[35] A. Bozkurt, I. Ladabaum, A. Atalar, and B. T. Khuri-Yakub, "Theory and analysis of electrode size optimization for capacitive microfabricated ultrasonic transducers," *ieee transactions on ultrasonics, ferroelectrics, and frequency control,* vol. 46, pp. 1364-1374, 1999.

[36] G. Caliano, A. Caronti, A. Savoia, C. Longo, M. Pappalardo, E. Cianci*, et al.*, "Capacitive micromachined ultrasonic transducer (cMUT) made by a novel 'reverse fabrication process'," in *IEEE Ultrasonics Symposium*, 2005, pp. 479-82.

[37] A. Caronti, A. Coppa, A. Savoia, C. Longo, P. Gatta, B. Mauti*, et al.*, "Curvilinear capacitive micromachined ultrasonic transducer (CMUT) array fabricated using a reverse process," in *2008 IEEE Ultrasonics Symposium*, 2008, pp. 2092-2095.

[38] I. Albert, H. Chen, L. L. Wong, S. Na, Z. Li, M. Macecek*, et al.*, "Fabrication of a Curved Row-Column Addressed Capacitive Micromachined Ultrasonic Transducer Array," 2016.

[39] J. Gelly and F. Lanteri, "Comparison of piezoelectric (thickness mode) and MEMS transducers," in *Ultrasonics, 2003 IEEE Symposium on*, 2003, pp. 1965-1974.

[40] M. Torndahl, M. Almqvist, L. Wallman, H. W. Persson, and K. Lindstrom, "Characterisation and comparison of a cMUT versus a piezoelectric transducer for air applications," in *Ultrasonics Symposium, 2002. Proceedings. 2002 IEEE*, 2002, pp. 1023-1026.

[41] B. T. Khuri-Yakub, C.-H. Cheng, F.-L. Degertekin, S. Ergun, S. Hansen, X.-C. Jin*, et al.*, "Silicon micromachined ultrasonic transducers," *Japanese Journal of Applied Physics,* vol. 39, p. 2883, 2000.

[42] E. Cianci, L. Visigalli, V. Foglietti, G. Caliano, and M. Pappalardo, "Improvements towards a reliable fabrication process for cMUT," *Microelectronic Engineering,* vol. 67, pp. 602-608, 2003.

[43] O. Ahrens, A. Buhrdorf, D. Hohlfeld, L. Tebje, and J. Binder, "Fabrication of gap-optimized CMUT," *IEEE transactions on ultrasonics, ferroelectrics, and frequency control,* vol. 49, pp. 1321-1329, 2002.

[44] B. Belgacem, D. Alquier, P. Muralt, J. Baborowski, S. Lucas, and R. Jerisian, "Optimization of the fabrication of sealed capacitive transducers using surface micromachining," *Journal of Micromechanics and Microengineering,* vol. 14, p. 299, 2003.

[45] S. Calmes, C. Cheng, F. Degertekin, X. Jin, S. Ergun, and B. Khuri-Yakub, "Highly integrated 2-D capacitive micromachined ultrasonic transducers," in *Ultrasonics Symposium, 1999. Proceedings. 1999 IEEE*, 1999, pp. 1163-1166.

[46] O. Ahrens, D. Hohlfeld, A. Buhrdorf, O. Glitza, and J. Binder, "A new class of capacitive micromachined ultrasonic transducers," in *Ultrasonics Symposium, 2000 IEEE*, 2000, pp. 939-942.

[47] A. Buhrdorf, L. Tebje, O. Ahrens, O. Glitza, and J. Binder, "Capacitive micromachined ultrasonic transducer (cMUT) array for the frequency range below 500 kHz," in *Ultrasonics Symposium, 2000 IEEE*, 2000, pp. 915-918.

[48] G. Caliano, F. Galanello, A. Caronti, R. Carotenuto, M. Pappalardo, V. Foglietti*, et al.*, "Micromachined ultrasonic transducers using silicon nitride membrane fabricated in PECVD technology," in *Ultrasonics Symposium, 2000 IEEE*, 2000, pp. 963-968.

[49] G. Caliano, R. Carotenuto, A. Caronti, and M. Pappalardo, "cMUT echographic probes: Design and fabrication process," in *Ultrasonics Symposium, 2002. Proceedings. 2002 IEEE*, 2002, pp. 1067-1070.

[50] R. Noble, R. Davies, D. King, M. Day, A. Jones, J. McIntosh*, et al.*, "Low-temperature micromachined cMUTs with fully-integrated analogue front-end electronics," in *Ultrasonics Symposium, 2002. Proceedings. 2002 IEEE*, 2002, pp. 1045-1050.

[51] M. Pappalardo, G. Caliano, A. Caronti, F. D'Alessio, C. Cucco, E. Cianci*, et al.*, "Capacitive ultrasonic transducers with a new vibrating structure," in *Ultrasonics, 2003 IEEE Symposium on*, 2003, pp. 1955-1959.

[52] A. Buhrdorf, A. Lohfink, S. Junge, P. Eccardt, and W. Benecke, "Fabrication and characterization of a new capacitive micromachined ultrasonic transducer (cMUT) using

polysilicon as membrane and sacrificial layer material," in *Ultrasonics, 2003 IEEE Symposium on*, 2003, pp. 1951-1954.

[53] L. L. Wong, A. I. Chen, and J. T. Yeow, "CMUT front-end circuits designed in a high-voltage CMOS process and the phase measurement receiver circuit," in *2012 IEEE International Ultrasonics Symposium*, 2012, pp. 1838-1841.

[54] M. I. Haller and B. T. Khuri-Yakub, "A surface micromachined electrostatic ultrasonic air transducer," in *Ultrasonics Symposium, 1994. Proceedings., 1994 IEEE*, 1994, pp. 1241-1244.

[55] Y. Huang, A. Ergun, E. Haeggstrom, and B. Khuri-Yakub, "Fabrication of Capacitive Micromachined Ultrasonic Transducers (CMUTs) using wafer bonding technology for low frequency (10 kHz-150 kHz) sonar applications," in *OCEANS'02 MTS/IEEE*, 2002, pp. 2322-2327.

[56] Y. Huang, E. Hæggström, M. H. Badi, and B. Khuri-Yakub, "Fabricating capacitive micromachined ultrasonic transducers with wafer-bonding technology," *Microelectromechanical Systems, Journal of,* vol. 12, pp. 128-137, 2003.

[57] A. S. Logan, L. L. Wong, A. I. Chen, and J. T. Yeow, "A 32 x 32 element row-column addressed capacitive micromachined ultrasonic transducer," *IEEE transactions on ultrasonics, ferroelectrics, and frequency control,* vol. 58, pp. 1266-1271, 2011.

[58] A. S. Logan and J. T. Yeow, "1-D CMUT arrays fabricated using a novel wafer bonding process," in *Ultrasonics Symposium, 2008. IUS 2008. IEEE*, 2008, pp. 1226-1229.

[59] F. Y. Yamaner, X. Zhang, and Ö. Oralkan, "A three-mask process for fabricating vacuum-sealed capacitive micromachined ultrasonic transducers using anodic bonding," *Ultrasonics, Ferroelectrics, and Frequency Control, IEEE Transactions on,* vol. 62, pp. 972-982, 2015.

[60] J. Yu, Y. Wang, J.-Q. Lu, and R. J. Gutmann, "Low-temperature silicon wafer bonding based on Ti/Si solid-state amorphization," *Applied physics letters,* vol. 89, p. 2104, 2006.

[61] F. Niklaus, G. Stemme, J.-Q. Lu, and R. Gutmann, "Adhesive wafer bonding," *Journal of applied physics,* vol. 99, p. 031101, 2006.

[62] A. Bakhtazad, R. Manwar, and S. Chowdhury, "Fabrication and characterization of sealed cavities realized by adhesive wafer bonding with dry etched Cyclotene™," *Microsystem Technologies,* pp. 1-8, 2015.

[63] X. Zhuang, D.-S. Lin, Ö. Oralkan, and B. T. Khuri-Yakub, "Fabrication of flexible transducer arrays with through-wafer electrical interconnects based on trench refilling with PDMS," *Journal of Microelectromechanical Systems,* vol. 17, pp. 446-452, 2008.

[64] "Processing Procedures for CYCLOTENE 3000 Series Dry Etch Resins," Dow Chemical2012.

[65] A. Almajid, L. Sorochynska, K. Friedrich, and B. Wetzel, "Effects of graphene and CNT on mechanical, thermal, electrical and corrosion properties of vinylester based nanocomposites," *Plastics, Rubber and Composites,* vol. 44, pp. 50-62, 2015.

[66] P. Gupta, M. Rajput, N. Singla, V. Kumar, and D. Lahiri, "Electric field and current assisted alignment of CNT inside polymer matrix and its effects on electrical and mechanical properties," *Polymer,* vol. 89, pp. 119-127, 2016.

[67] E. M. Jackson, P. E. Laibinis, W. E. Collins, A. Ueda, C. D. Wingard, and B. Penn, "Development and thermal properties of carbon nanotube-polymer composites," *Composites Part B: Engineering,* 2016.

[68] K. S. Khare, F. Khabaz, and R. Khare, "Effect of carbon nanotube functionalization on mechanical and thermal properties of cross-linked epoxy–carbon nanotube nanocomposites: role of strengthening the interfacial interactions," *ACS applied materials & interfaces,* vol. 6, pp. 6098-6110, 2014.

[69] C. Pan, H. Yang, S. Shen, M. Chou, and H. Chou, "A low-temperature wafer bonding technique using patternable materials," *Journal of Micromechanics and Microengineering,* vol. 12, p. 611, 2002.

[70] F. Niklaus, J. Lu, J. McMahon, J. Yu, S. Lee, T. Cale*, et al.*, "Wafer-level 3D integration technology platforms for ICs and MEMs," *Proc. 22nd Int. VMIC,* pp. 486-493, 2005.

[71] F. Niklaus, R. Kumar, J. McMahon, J. Yu, J.-Q. Lu, T. Cale*, et al.*, "Adhesive wafer bonding using partially cured benzocyclobutene for three-dimensional integration," *Journal of The Electrochemical Society,* vol. 153, pp. G291-G295, 2006.

[72] M. Makihata, S. Tanaka, M. Muroyama, S. Matsuzaki, H. Yamada, T. Nakayama*, et al.*, "Adhesive wafer bonding using a molded thick benzocyclobutene layer for wafer-level integration of MEMS and LSI," *Journal of Micromechanics and Microengineering,* vol. 21, p. 085002, 2011.

[73] B. Bayram, G. G. Yaralioglu, A. S. Ergun, and B. Khuri-Yakub, "Influence of the electrode size and location on the performance of a CMUT [US transducer]," in *Ultrasonics Symposium, 2001 IEEE*, 2001, pp. 949-952.

[74] J. Oberhammer, F. Niklaus, and G. Stemme, "Selective wafer-level adhesive bonding with benzocyclobutene for fabrication of cavities," *Sensors and Actuators A: Physical,* vol. 105, pp. 297-304, 2003.

[75] "Material Safety Data Sheet for AP3000," Dow Chemical Company2006.

[76] "Product Safety Assessment: DOWANOL™ PM Glycol Ether [Propylene Glycol Methyl Ether]," The Dow Chemical Company2015.

[77] A. Strandjord, W. Rogers, Y. Ida, R. DeVeillis, S. Shiau, E. Moyer*, et al.*, "Photosensitive benzocyclobutene for stress-buffer and passivation applications (one mask manufacturing process)," in *Electronic Components and Technology Conference, 1997. Proceedings., 47th*, 1997, pp. 1260-1268.

[78] Y.-H. So, P. Garrou, J.-H. Im, and D. M. Scheck, "Benzocyclobutene-based polymers for microelectronics," *Chemical innovation,* vol. 31, pp. 40-47, 2001.

[79] M. J. Madou, *Fundamentals of microfabrication: the science of miniaturization*: CRC press, 2002.

[80] (2016). *CYCLOTENE Advanced Electronics Resins - Infrared Spectra*. Available: http://www.dow.com/cyclotene/solution/infrared.htm

[81] S. Poulin, D. Yang, E. Sacher, C. Hyett, and T. Ellis, "The surface structure of Dow Cyclotene 3022, as determined by photoacoustic FTIR, confocal Raman and photoelectron spectroscopies," *Applied surface science,* vol. 165, pp. 15-22, 2000.

[82] S. Sivoththaman, R. Jeyakumar, L. Ren, and A. Nathan, "Characterization of low permittivity (low-k) polymeric dielectric films for low temperature device integration," *Journal of Vacuum Science & Technology A,* vol. 20, pp. 1149-1153, 2002.

[83] P. Linstrom and W. Mallard, "NIST Chemistry WebBook, NIST Standard Reference Database Number 69, National Institute of Standards and Technology, Gaithersburg MD, 20899," ed, 2010.

[84] G. Socrates, *Infrared and Raman characteristic group frequencies: tables and charts*: John Wiley & Sons, 2004.

[85] Z. Li, L. L. Wong, A. I. Chen, S. Na, J. Sun, and J. T. Yeow, "Fabrication of CMUT based on adhesive wafer bonding technique," *Journal of Micromechanics and Microengineering,* vol. 26, 2016.

[86] Z. Li, A. I. Chen, L. L. Wong, S. Na, and J. T. Yeow, "Fabrication of polymer-based wafer-bonded capacitive micromachined ultrasonic transducers," in *Ultrasonics Symposium (IUS), 2015 IEEE International*, 2015, pp. 1-4.

[87] "Processing Procedures for CYCLOTENE 4000 Series Photo BCB Resins," Dow Chemical 2005.

[88] J.-h. Im, E. O. Shaffer, T. Stokich, A. Strandjord, J. Hetzner, J. Curphy*, et al.*, "On the mechanical reliability of photo-BCB-based thin film dielectric polymer for electronic packaging applications," *Journal of Electronic Packaging,* vol. 122, pp. 28-33, 2000.

[89] "Processing procedures for BCB adhesion," Dow Chemical June 2007.

[90] S. Mack, H. Baumann, U. Gösele, H. Werner, and R. Schlögl, "Analysis of Bonding ‐ Related Gas Enclosure in Micromachined Cavities Sealed by Silicon Wafer Bonding," *Journal of the Electrochemical Society,* vol. 144, pp. 1106-1111, 1997.

[91] I. Ladabaum, X. Jin, H. T. Soh, A. Atalar, and B. t Khuri-Yakub, "Surface micromachined capacitive ultrasonic transducers," *IEEE transactions on ultrasonics, ferroelectrics, and frequency control,* vol. 45, pp. 678-690, 1998.

[92] J. N. Coupland and D. J. McClements, "Physical properties of liquid edible oils," *Journal of the American Oil Chemists' Society,* vol. 74, pp. 1559-1564, 1997.

[93] R. Chanamai and D. J. McClements, "Ultrasonic attenuation of edible oils," *Journal of the American Oil Chemists' Society,* vol. 75, pp. 1447-1448, 1998.

[94] H. S. Ju, E. J. Gottlieb, D. R. Augenstein, G. J. Brown, and B. R. Tittmann, "An empirical method to estimate the viscosity of mineral oil by means of ultrasonic attenuation," *IEEE transactions on ultrasonics, ferroelectrics, and frequency control,* vol. 57, pp. 1612-1620, 2010.

[95] A. S. Logan, L. L. Wong, and J. T. Yeow, "A 1-D capacitive micromachined ultrasonic transducer imaging array fabricated with a silicon-nitride-based fusion process," *IEEE/ASME Transactions on Mechatronics,* vol. 16, pp. 861-865, 2011.

[96] W. H. Peake and E. G. Thurston, "The Lowest Resonant Frequency of a Water‐Loaded Circular Plate," *The Journal of the Acoustical Society of America,* vol. 26, pp. 166-168, 1954.

[97] E. Ventsel and T. Krauthammer, *Thin plates and shells: theory: analysis, and applications*: CRC press, 2001.

[98] S. Reyntjens and R. Puers, "A review of focused ion beam applications in microsystem technology," *Journal of Micromechanics and Microengineering,* vol. 11, p. 287, 2001.

[99] A. Ektessabi and T. Sano, "Sputtering and thermal effect during ion microbeam patterning of polymeric films," *Review of Scientific Instruments,* vol. 71, pp. 1012-1015, 2000.

[100] L. E. Kinsler, A. R. Frey, A. B. Coppens, and J. V. Sanders, "Fundamentals of acoustics," *Fundamentals of Acoustics, 4th Edition, by Lawrence E. Kinsler, Austin R. Frey, Alan B. Coppens, James V. Sanders, pp. 560. ISBN 0-471-84789-5. Wiley-VCH, December 1999.,* p. 560, 1999.

[101] S. Chakraverty, *Vibration of plates*: CRC press, 2008.

[102] A. W. Leissa, "Vibration of plates," DTIC Document1969.

[103] Y. Nemirovsky and O. Bochobza-Degani, "A methodology and model for the pull-in parameters of electrostatic actuators," *Journal of microelectromechanical systems,* vol. 10, pp. 601-615, 2001.

Appendix A CMUT Modelling

A.1 Lumped Model

The typical structure of a CMUT cell is illustrated in Figure 56-a. By applying a potential difference between top and bottom electrodes, the plate is pulled downward. Assuming that the thin plate has a small deflection, the mechanical force induced by the plate deformation can be modelled as a spring force. The cavity under the plate is vacuum sealed. There is medium, such as air or liquid on the top of the plate, executes loading force to the plate. The loading force is negatively proportional to the velocity of the and can be treated as a damper. As a result, CMUT can be simplified as a spring-mass damper system as illustrated in Figure 56-b.

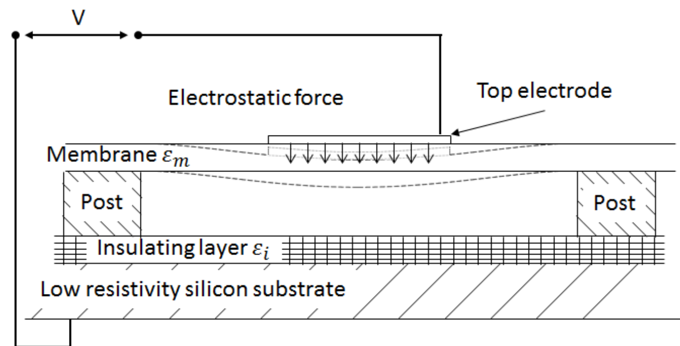

a) Typical structure of a CMUT cell

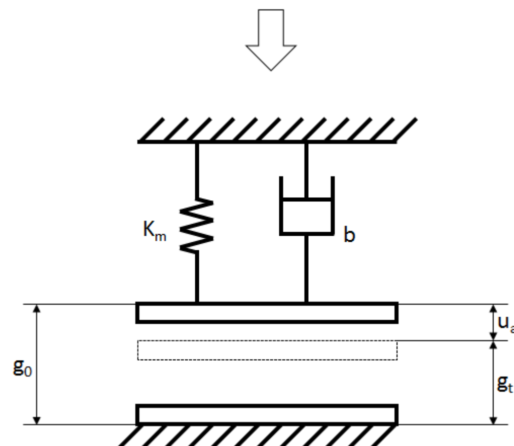

b) Spring-mass-damper system

Figure 56: Spring-mass damping system

A typical CMUT structure contains three layers between top and bottom electrodes:

- Insulating layer with thickness t_i and relative permittivity ε_i;
- Membrane layer with thickness t_m and relative permittivity ε_m;
- Vacuum cavity with depth t_c and relative permittivity $\varepsilon_c = 1$.

Then the effective gap height of the illustrated CMUT at equilibrium position (g_0) with cavity depth (t_c^0) and at certain moment (g_t) with cavity depth (t_c^t) can be calculated by Equation 4.

$$g_0 = t_c^0 + \frac{t_i}{\varepsilon_i} + \frac{t_m}{\varepsilon_m}$$
$$g_t = t_c^t + \frac{t_i}{\varepsilon_i} + \frac{t_m}{\varepsilon_m} \qquad \text{Equation 4}$$

The dynamics of the plate can then be analyzed using Equation 5. The involved force contains: 1) loading force from the medium F_l; 2) mechanical force from the plate deflection F_m; 3) electrostatic force F_e; and 4) force of inertia from membrane mass F_g. Each force will be discussed separately.

$$F_l + F_m + F_e + F_g = 0 \qquad \text{Equation 5}$$

A.1.1 Loading Force

Loading force can be calculated by:

$$F_l = |Z_m|\pi a^2 \frac{du_a}{dt} \qquad \text{Equation 6}$$

The radiation impedance Z_m of membrane in medium can be calculated by [100]:

$$Z_r = R_r + jX_r = \rho_{medium} c\pi a_{eff}^2 \left[1 - \frac{J_1(2\omega a_{eff}/c)}{2\omega a_{eff}/c} + j\frac{H_1(2\omega a_{eff}/c)}{2\omega a_{eff}/c}\right] \qquad \text{Equation 7}$$

Function J_1 is the first-order Bessel function of the first kind, and the function H_1 is the first-order Struve function. Parameters of ρ_{medium}, c and ω are the medium density, sound speed in the medium and the vibration frequency, respectively. Parameter a_{eff} is the effective

radius when equal the plate to a piston that displace the same volume at the moment of pull-in. The pull-in effect will be described later in the section A.2.

The Equation 5 becomes:

$$|Z_m|\pi a^2 \frac{du_a}{dt} + F_m + F_e + F_g = 0$$ Equation 8

A.1.2 Mechanical Force

Mechanical force is induced by the membrane deflection and boundary conditions. When the CMUT membrane, which is a thin plate, is simplified as a mass, the mechanical force can be modelled in the form of spring force:

$$F_m = \mathrm{k}_m u_a$$ Equation 9

Where k_m is the spring constant and u_a is the average displacement of the plate.

According to the plate theory, the displacement u of a point on the thin plate at location (x, y) with load per unit area of $p(x, y)$ can be obtained through:

$$\nabla^4(u) = \frac{\partial^4 u}{\partial x^4} + 2\frac{\partial^4 u}{\partial x^2 \partial y^2} + \frac{\partial^4 u}{\partial y^4} = \frac{p(x, y)}{D}$$ Equation 10

Where D is the flexural rigidity of circular plate:

$$D = \frac{E t_m^3}{12(1 - \nu^2)}$$ Equation 11

It is easier for circular shape thin plate analysis in the polar coordinates:

$$\nabla^4(u) = \frac{\partial^4 u}{\partial r^4} + \frac{2}{r}\frac{\partial^3 u}{\partial r^3} - \frac{1}{r^2}\frac{\partial^2 u}{\partial r^2} + \frac{1}{r^3}\frac{\partial u}{\partial r} + \frac{2}{r^2}\frac{\partial^4 u}{\partial r^2 \partial \varphi^2} - \frac{2}{r^3}\frac{\partial^3 u}{\partial r \partial \varphi^2} + \frac{4}{r^4}\frac{\partial^2 u}{\partial \varphi^2} + \frac{1}{r^4}\frac{\partial^4 u}{\partial \varphi^4} = \frac{p(r, \varphi)}{D}$$

Equation 12

When operating CMUT in air, the plate deforms due to both atmosphere pressure (p_{atm}) and electrostatic force (F_e) as shown in Figure 57. The atmosphere pressure distributed over

the entire plate area. However, electrostatic force is applied only in the area of top electrode, which is distributed over the central area of the plate with the electrode radius b for $b = \eta a$.

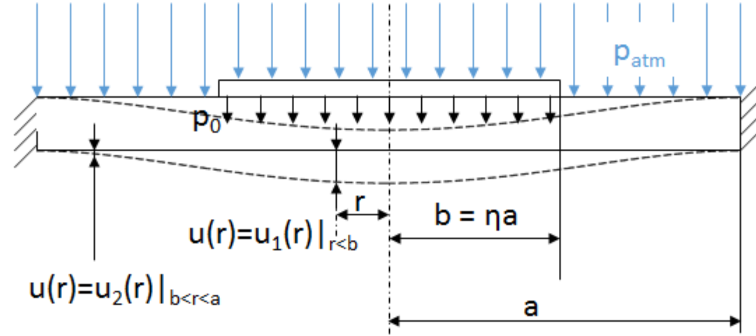

Figure 57: Both atmosphere pressure (p_{atm}) and electrostatic force (p_0) will induce membrane deflection.

When no bias voltage is applied, atmosphere pressure acts on the entire circular plate with edges clamped. The deflection function in terms of r under uniform pressure p_0 is given by Equation 13 [97].

$$u(r) = \frac{p_{atm}a^4}{64D}[1 - \left(\frac{r}{a}\right)^2]^2 \quad \text{Equation 13}$$

When applying a DC bias voltage, a uniform pressure p_0 is applied in the central plate region with radius of b together with the atmosphere pressure. The deflection function should be modified. The solution of Equation 12 for a circular thin plate with clamped edge under asymmetric distributed force can be expressed by Equation 14 [97]. In the equation, $p(r)$ is the pressure distribution over the thin plate, and constants C_1 to C_4 can be calculated based on the boundary conditions and continuity conditions.

$$\mathrm{u}(r) = C_1 lnr + C_2 r^2 lnr + C_3 r^2 + C_4 + \int \frac{1}{r}\left\{\int r \left[\int \frac{1}{r}\left(\int \frac{r}{D} p(r)\, dr\right) dr\right] dr\right\} dr$$

Equation 14

In order to calculate the deflection equation under atmosphere pressure over the entire plate and electrostatic force over the centre area of the plate, the plate needs to be divided into two parts:

$$\begin{cases} \mathrm{u}(r) = u_1(r) \cdots r \in [0, b) \\ \mathrm{u}(r) = u_2(r) \cdots r \in [b, a] \end{cases}$$ Equation 15

1) For the inner region: $r \in [0, b)$, $p(r) = p = p_0 + p_{atm}$

$$u_1(r) = C_{31}r^2 + C_{41} + \int \frac{1}{r}\left\{\int r\left[\int \frac{1}{r}\left(\int \frac{r}{D}p(r)\,dr\right)dr\right]dr\right\}dr$$

$$\Rightarrow u_1(r) = C_{31}r^2 + C_{41} + \frac{pr^4}{64D}$$ Equation 16

2) For outer region: $r \in [b, a]$, $p(r) = p_{atm}$

$$u_2(r) = C_{12}lnr + C_{22}r^2lnr + C_{32}r^2 + C_{42} + \int \frac{1}{r}\left\{\int r\left[\int \frac{1}{r}\left(\int \frac{r}{D}p(r)\,dr\right)dr\right]dr\right\}dr$$

$$\Rightarrow u_2(r) = C_{12}lnr + C_{22}r^2lnr + C_{32}r^2 + C_{42} + \frac{p_{atm}r^4}{64D}$$ Equation 17

Conditions for solving C_{31}, C_{41}, C_{12}, C_{22}, C_{32} and C_{42} are:

At $r = a$, two boundary conditions are applied: $u_2|_{r=a} = 0$ and $\left.\frac{du_2}{dr}\right|_{r=a} = 0$

$$C_{12}lna + C_{22}a^2lna + C_{32}a^2 + C_{42} + \frac{p_{atm}a^4}{64D} = 0$$ Equation 18

$$\frac{du_2}{dr} = C_{12}\frac{1}{a} + C_{22}a(2lna + 1) + 2C_{32}a + \frac{p_{atm}a^3}{16D} = 0$$ Equation 19

At $r = b$, four continuity conditions are applied: $u_1|_{r=b} = u_2|_{r=b}$, $\left.\frac{du_1}{dr}\right|_{r=b} = \left.\frac{du_2}{dr}\right|_{r=b}$, $M_{r1}|_{r=b} = M_{r2}|_{r=b}$ and $Q_{r1}|_{r=b} = Q_{r2}|_{r=b}$

$$C_{31}b^2 + C_{41} + \frac{pb^4}{64D} = C_{12}lnb + C_{22}b^2lnb + C_{32}b^2 + C_{42} + \frac{p_{atm}b^4}{64D}$$ Equation 20

$$2C_{31}b + \frac{pb^3}{16D} = C_{12}\frac{1}{b} + C_{22}b(2lnb + 1) + 2C_{32}b + \frac{p_{atm}b^3}{16D} \quad \text{Equation 21}$$

$$-D\left[2C_{31}(\nu + 1) + \frac{pb^2}{16D}(\nu + 3)\right]$$

$$= -D\left[C_{12}\frac{1}{b^2}(\nu - 1) + C_{22}[2lnb(\nu + 1) + \nu + 3] \right. \quad \text{Equation 22}$$

$$\left. + 2C_{32}(\nu + 1) + \frac{p_{atm}r^2}{16D}(\nu + 3)\right]$$

$$-\frac{1}{2}pr = -4C_{22}D\frac{1}{r} - \frac{1}{2}p_{atm}r \quad \text{Equation 23}$$

Finally, by solving equations Equation 18 to Equation 23, deflection at the position with distance to plate center of r under both atmosphere pressure and electrostatic force can be calculated by Equation 24.

$$\mathrm{u}(r)|_{r\in[0,b)} = u_1(r) = C_{31}r^2 + C_{41} + \frac{pr^4}{64D} = C_{31}r^2 + C_{41} + \frac{(p_0 + p_{atm})r^4}{64D}$$

$$C_{31} = \frac{p_0a^2}{64D}[8\eta^2 ln\eta - 2\eta^4] - \frac{p_{atm}a^2}{32D}$$

$$C_{41} = \frac{p_0a^4}{64D}[4\eta^2 - 3\eta^4 + 4\eta^4 ln\eta] + \frac{p_{atm}a^4}{64D}$$

$$\mathrm{u}(r)|_{r\in[b,a]} = u_2(r) = C_{12}lnr + C_{22}r^2 lnr + C_{32}r^2 + C_{42} + \frac{p_{atm}r^4}{64D} \quad \text{Equation 24}$$

$$C_{12} = \frac{p_0a^4\eta^4}{16D} \qquad C_{22} = \frac{p_0a^2\eta^2}{8D}$$

$$C_{32} = -\frac{p_0a^2}{64D}[2\eta^4 + 4\eta^2(2lna + 1)] - \frac{p_{atm}a^2}{32D}$$

$$C_{42} = \frac{p_0a^4}{64D}[4\eta^2 + 2\eta^4(1 - 2lna)] + \frac{p_{atm}a^4}{64D}$$

Based on Equation 24, the average displacement $\boldsymbol{u_a}$ and spring constant k_m can then be calculated.

$$u_a = \frac{\int_0^a 2\pi r u(r) dr}{\pi a^2} = \frac{\int_0^b 2\pi r u_1(r) dr}{\pi a^2} + \frac{\int_{\mathrm{b}}^a 2\pi r u_2(r) dr}{\pi a^2}$$

$$\Rightarrow u_a = \frac{p_0 a^4}{192D}[\eta^6 - 3\eta^4 + 3\eta^2] + \frac{p_{atm} a^4}{64D}\left[8\eta^6 ln\eta - \eta^8 - 3\eta^6 + 5\eta^4 - \eta^2 + \frac{1}{3}\right] \quad \text{Equation 25}$$

$$\mathrm{k}_m = \frac{p_0 \pi b^2}{u_a|_{p=p_0+p_{atm}} - u_a|_{p_0=0}} = \frac{p_0 \pi b^2}{\frac{p_0 a^4}{192D}[\eta^6 - 3\eta^4 + 3\eta^2]} = \frac{p_0 \pi a^2 \eta^2}{\frac{p_0 a^4}{192D}[\eta^6 - 3\eta^4 + 3\eta^2]}$$

$$\Rightarrow \mathrm{k}_m = \frac{192\pi D}{a^2}\frac{\eta^2}{\eta^6 - 3\eta^4 + 3\eta^2} \quad \text{Equation 26}$$

A.1.3 Electrostatic Force

The electrostatic force was generated when there is a potential difference between the top and bottom electrode. From the energy point of view,

$$F_e = -\frac{dE}{du_a} = -\frac{d\left(\frac{1}{2}QV\right)}{du_a} = -\frac{d\left(\frac{1}{2}CV^2\right)}{du_a} = -\frac{1}{2}V^2\frac{dC}{du_a} \quad \text{Equation 27}$$

Based on Equation 24, the capacitance of the cell under loading can be calculated by:

$$C = \int_0^b \frac{2\pi\varepsilon r}{g_0 - u_1(r)} dr = \int_0^b \frac{2\pi\varepsilon r}{g_0 - \left(C_{31}r^2 + C_{41} + \frac{pr^4}{64D}\right)} dr$$

$$\Rightarrow C = \frac{-2\pi\varepsilon}{\sqrt{\Delta}} artanh\left[\frac{\frac{p}{32D}b^2\sqrt{\Delta}}{\Delta - \frac{p}{32D}b^2 C_{31} - C_{31}^2}\right] \quad \text{Equation 28}$$

$$\Delta = C_{31}^2 - 4\frac{p}{64D}(C_{41} - g_0) > 0$$

One can then calculate $\frac{dC}{du_a}$ to determine the electrostatic force under bias voltage of V.

Equation 5 then becomes:

$$|Z_m|\pi a^2 \frac{du_a}{dt} + \mathrm{k}_m u_a - \frac{1}{2}V^2 \frac{dC}{du_a} + F_g = 0$$ Equation 29

Spring Softening Effect

Tylor expanding Equation 27 at the first order,

$$-\frac{1}{2}V^2 \frac{dC}{du_a} = -A - B(u_a - u_{aDC}) + O^1(u_a)$$ Equation 30

Where u_a^{DC} is the average displacement under DC bias of V.

Constants A and B can be expressed in:

$$A = \frac{1}{2}V^2 \frac{dC}{du_a}\bigg|_{u_a = u_a^{DC}}$$

$$B = \frac{1}{2}V^2 \frac{d^2C}{du_a^2}\bigg|_{u_a = u_a^{DC}}$$

At this point, Equation 5 can be expressed as:

$$F_g + |Z_m|\pi a^2 \frac{du_a}{dt} + [\mathrm{k}_m - B]u_a + B\, u_a^{DC} - A = 0$$ Equation 31

For $B > 0$, the effective spring constant decreases by the increase of bias voltage due to the existence of term $-\frac{1}{2}V^2 \frac{d^2C}{du_a^2}\Big|_{u_a = u_a^{DC}}$. This phenomenon is called "spring softening effect".

A.1.4 Force of Inertia

Force of inertia can be expressed by:

$$F_g = -m_{eq}\frac{d^2u_a}{dt^2} \qquad \text{Equation 32}$$

A circular thin plate with edge clamped has in-air natural resonance frequency [101, 102]:

$$f_r = \frac{1}{2\pi}\frac{10.22}{\mathrm{a}^2}\sqrt{\frac{D}{\rho t_m}} \qquad \text{Equation 33}$$

The resonance frequency of a spring-mass system can also be calculated as:

$$f_r = \frac{1}{2\pi}\sqrt{\frac{\mathrm{k}_m}{m_{eq}}} \qquad \text{Equation 34}$$

Then, by taking Equation 26 in to Equation 34, the equivalent membrane mass can be calculated by solving Equation 33 and Equation 34.

$$m_{eq} = 1.84\rho\pi a^2 t_m\frac{\eta^2}{\eta^6 - 3\eta^4 + 3\eta^2} = 1.84m\frac{\eta^2}{\eta^6 - 3\eta^4 + 3\eta^2} \qquad \text{Equation 35}$$

A.2 Pull-in Effect

CMUT is a voltage controlled capacitive actuator and the pull-in effect is usually analyzed in static condition [103]. As shown in Figure 58, there are two equilibrium states when applying bias voltage: stable state corresponding to low total energy and non-stable state corresponding to high total energy. The electric energy stored in the CMUT contributed by the accumulated charges is $U_e = \frac{1}{2}CV^2$; and the mechanical energy contributed by the plate deflection is U_m. When the bias voltage increases, two equilibrium states get closer. At a certain bias voltage, the two equilibrium states become one. This bias voltage is the pull-in voltage.

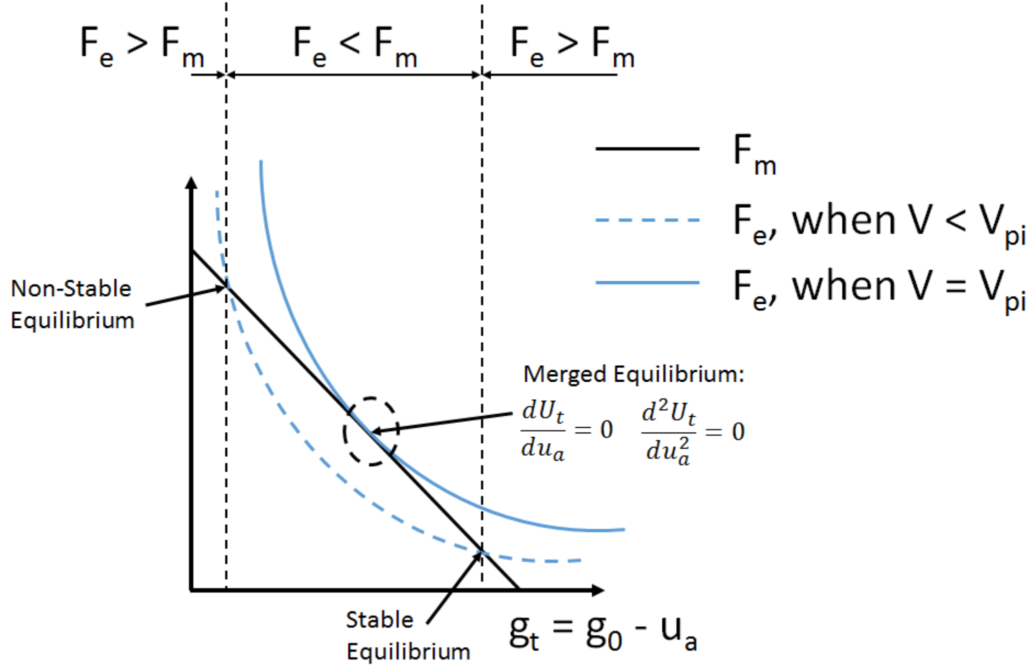

Figure 58: The intersection between the curve of electrostatic force and the spring force are the equilibrium states. The upper-left one is the non-stable one corresponding to higher energy and the lower-right one is the stable one corresponding to lower energy. When bias voltage is equal to the pull-in voltage, two equilibriums are merged.

At pull-in bias voltage, the first spatial derivative of the potential energy (force) and its second derivation (slope) of electric energy and the mechanical energy are equal, thus we have:

$$\frac{dU_t}{du_a} = \frac{1}{2}V^2\frac{dC}{du_a} + \frac{dU_m}{du_a} = 0 \Longrightarrow -\frac{1}{2}V^2 = \frac{dU_m}{du_a}\Big/\frac{dC}{du_a}$$

$$\frac{d^2U_t}{du_a^2} = \frac{1}{2}V^2\frac{d^2C}{du_a^2} + \frac{d^2U_m}{du_a^2} = 0 \Longrightarrow -\frac{1}{2}V^2 = \frac{d^2U_m}{du_a^2}\Big/\frac{d^2C}{du_a^2}$$

$$\Longrightarrow \frac{dU_m}{du_a}\Big/\frac{dC}{du_a} = \frac{d^2U_m}{du_a^2}\Big/\frac{d^2C}{du_a^2} \Longrightarrow \frac{dU_m}{du_a}\frac{d^2C}{du_a^2} = \frac{d^2U_m}{du_a^2}\frac{dC}{du_a}$$

$$or\ \frac{dU_m}{du_a}\frac{d^2C}{du_a^2} - \frac{d^2U_m}{du_a^2}\frac{dC}{du_a} = 0 \qquad \text{Equation 36}$$

By solving Equation 36, average displacement of membrane $u_a = u_{a_pi}$,when $V = V_{pi}$, can calculated. Furthermore, the electrostatic force $F_e = \frac{1}{2}C_{pi}V_{pi}^2 = F_m = k_m u_{a_pi}$. The pull-in voltage can then be calculated.